Thin film growth and structural investigation of $DyBa_2Cu_3O_{7-\delta}$

Von der Fakultät Chemie der Universität Stuttgart
zur Erlangung der Würde eines Doktors der
Naturwissenschaften (Dr. rer. nat.) genehmigte Abhandlung

Vorgelegt von

Daniel Putzky

aus Dresden, Deutschland

Hauptberichter:	Prof. Dr. Bernhard Keimer
Mitberichter:	Prof. Dr. Guido Schmitz
Prüfungsvorsitzender:	Prof. Dr. Rainer Niewa
Tag der mündlichen Prüfung:	18.12.2020

Max-Planck-Institut für Festkörperforschung
Universität Stuttgart

Stuttgart 2020

Contents

Abbreviations

123 cuprates	cuprates with the stoichiometry $RE\mathrm{Ba_2Cu_3O_{7-\delta}}$
AFM	Atomic force microscopy
ALL-BME	Atomic layer-by-layer molecular-beam epitaxy
ARPES	Angle-resolved photoemission spectroscopy
a.u.	arbitrary units
CDW	Charge density wave
DyBCO	Dysprosium barium copper oxide, $\mathrm{DyBa_2Cu_3O_{7-\delta}}$
ϵ	Lattice mismatch of substrate and film
HTSC	High temperature superconductor
LSAT	Lanthanum strontium aluminum tantalate, $(\mathrm{LaAlO_3})_{0.3}(\mathrm{Sr_2AlTaO_6})_{0.7}$
MBE	Molecular-beam epitaxy
MI	Mutual inductance
MIT	Metal-insulator transition
NdBCO	Neodymium barium copper oxide, $\mathrm{NdBa_2Cu_3O_{7-\delta}}$
NGO	Neodymium gallate, $\mathrm{NdGaO_3}$
pc	pseudo-cubic
PLD	Pulsed laser deposition
$p(O_3)$	Ozone partial pressure
PrBCO	Praseodymium barium copper oxide, $\mathrm{PrBa_2Cu_3O_{7-\delta}}$
PVD	Physical vapor deposition
QCM	Quartz crystal microbalance

RE	Rare earth element
*RE*BCO	Rare earth barium copper oxide, $RE\mathrm{Ba_2Cu_3O_{7-\delta}}$
RGA	Residual-gas analyzer
RXS	Resonant x-ray scattering
RHEED	Reflection high-energy electron diffraction
r.l.u.	reciprocal lattice units
RRR	Residual resistance ration
RSM	Reciprocal space map
SC	Superconductivity, superconductor
STE	Shutter transient effect
STEM	Scanning transmission electron microscopy
STO	Strontium titanate, $\mathrm{SrTiO_3}$
T_c	Superconducting transition temperature
TM	Transition metal
TMO	Transition metal oxide
TP	Twinning plane
u.c.	unit cell
XAS	X-ray absortion spectroscopy
XMCD	X-ray magnetic circular dichroism
XRD	X-ray diffraction
YBCO	Yttrium barium copper oxide, $\mathrm{YBa_2Cu_3O_{7-\delta}}$

Zusammenfassung in deutscher Sprache

Auch Jahrzehnte nach ihrer Entdeckung stehen hochtemperatursupraleitende Kupferoxide nach wie vor an der Spitze der Forschung zu kondensierter Materie. Die so genannte 123-Cuprat-Familie mit der Zusammensetzung $RE\mathrm{Ba_2Cu_3O_{7-\delta}}$ (RE = Y oder Seltenerdmetall) ist die erste Materialklasse, die einen supraleitenden Übergang oberhalb der Temperatur von flüssigem Stickstoff besitzt. Solche hohen Übergangstemperaturen sind nicht nur von großem technologischen Interesse, sondern sie stellen auch unser grundlegendes Verständnis des supraleitenden Mechanismus in Frage. Es wurden viele Anstrengungen unternommen, um den mikroskopischen Mechanismus hinter der Hochtemperatur-Supraleitung zu verstehen, mit dem Ziel, die Übergangstemperatur weiter zu erhöhen und sie sogar der Raumtemperatur anzunähern. In über drei Jahrzehnten Forschung wurde eine Vielzahl von Phänomenen entdeckt, die direkt oder indirekt mit der Supraleitung in Cupraten zusammenhängen, einschließlich Antiferromagnetismus, Spindichtewellenordnung, Ladungsdichtewellen und das Pseudogap-Regime [1]. All diese Ergebnisse lassen sich in einem umfangreichen Phasendiagramm zusammenfassen, in dem durch eine relativ kleine Änderung von Parametern, wie z.B. Dotierung und Tem-

peratur, auf die einzelnen Phasen zugegriffen werden kann.

Diese Arbeit befasst sich mit epitaktischen Dünnfilmen aus $DyBa_2Cu_3O_{7-\delta}$ (DyBCO), einem Mitglied der 123-Cuprat-Familie mit einem maximalen supraleitenden Übergang bei 93 K. In den letzten Jahren ermöglichten Fortschritte in den Dünnschichtabscheidungstechnologien die Synthese von künstlichen Strukturen mit atomarer Genauigkeit. Die DyBCO-Dünnfilme wurden mit modernster Oxid-Molekularstrahlepitaxie (MBE) gewachsen. Anders als bei früherem MBE-Wachstum mit Parallelabscheidung wurde eine atomare layer-by-layer Sequenz mit *in-situ* Elektronenstrahlbeugung ("reflection high-energy electron diffraction") entwickelt. Diese Wachstumsmethode ermöglicht eine *in-situ* Rückmeldung zu den einzeln abgeschiedenen Elemente und zur Identifizierung der gebildeten Phase. Weiterhin kann die Stöchiometrie während des Wachstums angepasst werden. Die Qualität der dünnen Schichten wurde durch eine umfangreiche *ex-situ* Charakterisierung untersucht, wie z.B. Röntgenbeugung zur Phasenanalyse, Transport- und Gegeninduktionsmessungen zur Bestimmung der supraleitenden Übergangstemperatur, und Rastertransmissionselektronenmikroskopie zur Untersuchung von Stapelfehlern. All diese Informationen mündeten in einem optimierten Wachstum und einer hohen Qualität der dünnen Filme.

Darüber hinaus machen wir uns die Gitterfehlanpassung mit dem Substrat und die Heteroepitaxie zunutze, um die Auswirkungen der biaxialen Verspannung auf die Filmstruktur zu untersuchen. Die Kristallstruktur und Morphologie der DyBCO-Dünnfilme wurde durch systematische Änderung der Filmdicke und der Gitterfehlanpassung mit verschiedenen Substraten untersucht. 123-Cuprat-Einkristalle vollziehen bei einem Sauerstoffgehalt von $\delta < 0{,}65$ einen tetragonalen-zu-orthorhombischen Phasenübergang und bilden Zwillingsdomänen aus. Zur systematischen Untersuchung der Zwillingsbildung der DyBCO-Filme wurden Synchrotron-Röntgenbeugungsmessungen durchgeführt.

In jüngster Zeit hat die Beobachtung von Ladungsdichtewellen, die mit der Supraleitung konkurrieren, einen neuen Aspekt aufgeworfen, der für das Verständnis der Supraleitung in Cupraten wichtig sein könnte. Eine wirkungsvolle Methode zur Untersuchung der Ladungsordnung ist die resonante Röntgenstreuung, mit der sich kurzreichweitige Korrelationen nachweisen lassen. Darüber hinaus macht sich diese Technik die resonante Verstärkung des Streusignals zunutze, wodurch sie besonders geeignet ist dünne Filme zu untersuchen, die ein kleines Probenvolumen haben. Bisherige Untersuchungen der resonanten Streuung an der Cu L_3-Absorptionskante haben gezeigt, dass die Ladungsordnung in den CuO_2-Ebenen angeordnet ist. Ohne Magnetfeld und ohne äußeren Druck hat die Ladungsordnung nur beträchtliche Korrelationen in der Ebene, was ihr einen 2D-Charakter verleiht. Durch Anlegen eines großen Magnetfeldes oder einer einachsigen Dehnung entlang der a-Achse ergibt sich jedoch auch eine Korrelation außerhalb der Ebene [2, 3]. In verwandten $YBa_2Cu_3O_{7-\delta}$-Dünnfilmen wurde eine solche 3D-Korrelation sogar ohne Magnetfeld beobachtet [4], was auf die Fähigkeit der epitaktischen Verspannung hinweist, die elektronische Eigenschaften entscheidend zu verändern.
In dieser Arbeit untersuchten wir in hochwertigen Dünnfilmen die detaillierten Beziehungen zwischen der biaxialen Belastung, der Bildung von Zwillingsdomänen, der Filmdicke und schließlich deren Einfluss auf die elektronischen Eigenschaften. Unsere Ergebnisse geben neue Einblicke in das komplexe Zusammenspiel dieser Parameter.

Diese Arbeit ist wie folgt aufgebaut:
Kapitel 1 bietet eine Einführung in die 123-Cuprate mit besonderem Augenmerk auf die Struktur und die verschiedenen elektronischen Phasen, die durch Lochdotierung entstehen.
Kapitel 2 beschreibt das Dünnschichtwachstum mit Sauerstoff-MBE. Wir beleuchten theoretische Modelle des Dünnschichtwachstums und

die Vorteile der MBE. Ferner werden der MBE-Aufbau und die *in-situ* Messungen zur Kontrolle der Stöchiometrie und Phasenbildung vorgestellt und diskutiert.

In **Kapitel 3** wird eine kurze Zusammenfassung zur Wechselwirkung von Röntgenstrahlung mit kristallinen Materialien gegeben. Dieses Kapitel beschreibt ebenfalls die experimentellen Aufbauten und Techniken, die in dieser Arbeit verwendet wurden, um Informationen über Struktur, Gitterfehlanpassung und geordneten Zustände in den DyBCO-Dünnfilmen zu erhalten.

In **Kapitel 4** werden das DyBCO-Filmwachstum und die Charakterisierung diskutiert. Das Kapitel zeigt, wie *in-situ* Messmethoden zur Optimierung des Filmwachstums genutzt und wie Defekte unterdrückt wurden. Weiterhin stellen wir die Charakterisierung durch Röntgenbeugung, Rasterkraftmikroskopie und Rastertransmissionselektronenmikroskopie vor, die die hohe Qualität und minimale Defektbildung in unseren Filmen bestätigt hat. Abschließend wird ein Vergleich der supraleitenden Eigenschaften in Abhängigkeit von der Schichtdicke und der Gitterfehlanpassung vorgenommen.

In **Kapitel 5** wird die Auswirkung der epitaktischen Verspannung auf die Kristallstruktur der DyBCO-Filme im Detail diskutiert. Ein besonderer Schwerpunkt liegt auf der Untersuchung des tetragonalen-zu-orthorhombischen Phasenübergangs und der Bildung von Zwillingsdomänen. Abhängig von der Schichtdicke, der Substratauswahl und dem Sauerstoffgehalt der Filme werden verschiedene Stufen der Zwillingsbildung identifiziert. Während sehr dünne oder stark sauerstoffarme Filme eine (pseudo-) tetragonale Struktur aufweisen, bilden dicke und vollständig oxidierte Filme orthorhombische Zwillingsdomänen.

Kapitel 6 befasst sich mit der Untersuchung der Ladungsdichtewelle in den DyBCO-Filmen durch resonante Streuung an den Cu L_3 und Dy M_5-Absorpti-onskanten. Während die Ladungsordnung in den CuO_2-Ebenen bereits zuvor in Dünnfilmen beobachtet wurde, wiesen

DyBCO-Filme auch eine einkristallähnliche Sauerstoffordnung in den CuO-Kettenschichten auf. Beide, die Ladungsordnung und die Sauerstoffordnung, wurden ebenfalls an der Dy M_5-Kante detektiert und zeigen eine auffällige, nicht-monotone Feldabhängigkeit.
In **Kapitel 7** fassen wir unsere wichtigsten Ergebnisse und Schlussfolgerungen zusammen. Weiterhin zeigen wir auf, wie die entwickelte Wachstumsmethode und die Kontrolle der Mikrostruktur von DyBCO-Filmen neue Möglichkeiten für zukünftige Studien bietet.

Abstract

Decades after their discovery, high-temperature superconducting copper oxides continue to be at the forefront of condensed matter research. The so-called 123 cuprate family with the composition $RE\mathrm{Ba_2Cu_3O_{7-\delta}}$ (RE = Y or rare-earth element) have been the first class of materials to realize a superconducting transition above liquid nitrogen temperature. Such high transition temperatures are not only of great technological interest, but also call into question our fundamental understanding of the superconducting mechanism. Many efforts were devoted to understanding the microscopic mechanism behind high-temperature superconductivity with the aim to further increase the transition temperature and eventually bringing it even close to room temperature. Over more than three decades of research revealed a variety of phenomena, directly or indirectly related to superconductivity in cuprates including antiferromagnetism, spin density wave order, charge density waves and the pseudogap regime [1]. All these results can be summarized in a rich phase diagram, where distinct phases can be accessed by a relatively small change of parameters, such as doping and temperature.

This thesis focuses on epitaxial thin films of $\mathrm{DyBa_2Cu_3O_{7-\delta}}$ (DyBCO), a member of the 123 cuprate family with maximum superconducting transition at 93 K. In recent years, advances in thin film deposition

technologies made the synthesis of artificial structures with atomic-layer precision possible. The DyBCO thin films were grown with state-of-the-art oxide molecular-beam epitaxy (MBE). In contrast to previous growths by MBE using a co-deposition technique, an atomic layer-by-layer shutter sequence with *in-situ* reflection high-energy electron diffraction feedback was developed. This growth method allows for *in-situ* feedback for individually deposited elements and identifying the formed phase. Moreover, the stoichiometry can be adjusted during the growth. The quality of the thin films was evaluated by extensive *ex-situ* characterization, such as x-ray diffraction for phase analysis, transport and mutual inductance measurements for the determination of the superconducting transition temperature, and scanning transmission electron microscopy for the investigation of stacking faults. All this information converged in an optimized growth sequence and a high quality of the thin films.

Furthermore, we made use of the heteroepitaxy with a lattice mismatching substrate to study the effects of biaxial strain on the film structure. The crystal structure and morphology of the DyBCO thin films was investigated by systematic variation of film thickness and lattice mismatch with different substrates. 123 cuprate single crystals undergo a tetragonal-to-orthorhombic phase transition for an oxygen content $\delta < 0.65$ and form structural twin domains. Synchrotron x-ray diffraction measurements were carried out to systematically study the twinning of the DyBCO films.

Recently, the observation of charge density waves competing with superconductivity has brought up a new aspect that could be important for understanding superconductivity in cuprates. A powerful method to study the charge order is resonant x-ray scattering, which allows detection of short range correlations. Furthermore, this technique harnesses the resonant enhancement of the scattering signal, making it particularly suitable to investigate thin films, which have a small

sample volume. Previous resonant scattering studies performed at the Cu L_3 edge have revealed that the charge order is located in the CuO_2 planes. At zero magnetic field and without external pressure the charge order has only considerable in-plane correlations, giving it a 2D character. However, by applying a large magnetic field or uniaxial strain along the a-axis, a sizable out-of-plane correlation emerges [2, 3]. In related $YBa_2Cu_3O_{7-\delta}$ thin films such a 3D correlation has been observed even in zero magnetic field [4], indicating the ability of epitaxial strain to crucially modify the electronic properties.
In this thesis, we investigated in high quality thin films the detailed relationships between biaxial strain, the formation of twin domains, the film thickness and finally their influence on the electronic properties. Our results give new insights into the complex interplay of these parameters.

This thesis is structured as follows:
Chapter 1 provides an introduction to 123 cuprates, with a special focus on the structure and different electronic phases obtained upon hole doping.
Chapter 2 describes the thin film growth using oxide MBE. We highlight theoretical models of thin film growth and the advantages of MBE. Furthermore, the MBE setup and the *in-situ* feedback to control the stoichiometry and phase formation are presented and discussed.
In **chapter 3** a brief summary of the interaction of x-rays with crystalline materials is provided. This chapter also describes the experimental setups and x-ray techniques used in this thesis to obtain information about structure, epitaxial strain and the formation of ordered states in the DyBCO films.
In **chapter 4**, DyBCO thin film growth and film characterization are discussed. The chapter describes how *in-situ* feedback was used to optimize the film growth and how the defect formation was suppressed.

Moreover, we outline the characterization by x-ray diffraction, atomic force microscopy and scanning transmission electron microscopy that confirmed the high quality and minimal defect formation in our films. Finally, a comparison of the superconducting properties as a function of the film thickness and the lattice mismatch is presented.

In **chapter 5** the effect of epitaxial strain on the crystal structure of the DyBCO films is discussed in detail. A particular focus lies on the investigation of the tetragonal-to-orthorhombic phase transition and the formation of twin domains. Different stages of twinning are identified depending on film thickness, substrate choice and oxygen content of the films. While very thin or highly oxygen-deficient films show a (pseudo-) tetragonal structure, thick and fully oxidized films form orthorhombic twin domains.

Chapter 6 focuses on the investigation of the charge density wave in the DyBCO films by resonant scattering at the Cu L_3 and Dy M_5 edges. While charge order in the CuO_2 planes was previously observed in thin films, DyBCO films also revealed an oxygen order in the CuO chain layers akin to single crystals. Both, the charge order and oxygen order modulation, are also detected at the Dy M_5 edge and display a peculiar, non-monotonic field dependence.

In **chapter 7** we summarize our key findings and conclusions. Furthermore, we outline how the developed growth method and the control of the microstructure in DyBCO films provide new prospects for future studies.

Chapter 1

Introduction

Transition-metal oxides (TMOs) are a widely studied class of materials owing to their large variety of functional properties. These properties range from metallic to semiconducting to insulating states, and can show intriguing phenomena like metal-insulator transitions, spin order, charge order, colossal magnetoresistance, frustrated magnetism, and superconductivity. Their origin lies in the complex interplay of spin, charge, orbital and lattice degrees of freedom. The resulting different phases often compete with each other and strongly depend on external parameters, such as temperature, electric and magnetic field.

A intriguing method to manipulate the properties and the structure are thin films. Recent progress in thin film deposition technologies has drawn a lot of attention on different combinations of TMOs in artificial structures [5–8]. Heterostructures can be used to utilize the bulk properties of the individual materials and to generate new phenomena through interface reconstructions.

A relatively new method for growth of high quality complex oxide thins films is ozone-assisted atomic layer-by-layer molecular-beam epitaxy (ALL-MBE), where individual layers are deposited from effusion cells.

The operation of individual sources provides not only the opportunity to control atomic layers, but also to adjust the stoichiometry during growth and thereby generates an additional degree of freedom. This, in turn requires *in-situ* feedback to ensure the correct stoichiometry of the deposited material.

For TMOs with a comparatively simple perovskite structure (ABO_3), only the ratio of the A and B elements has to be controlled, while oxygen is provided from the ozone background atmosphere. Nevertheless, in more complex TMOs, the control of the stoichiometry is more complicated.

This thesis focuses on the high-temperature superconducting $DyBa_2Cu_3O_{7-\delta}$ (DyBCO), whose structure and composition requires a precise control of the stoichiometry of three cations in the layer-by-layer MBE growth. DyBCO belongs to the family of so-called 123 cuprates, referring to their cation stoichiometry. To get familiar with DyBCO, the next section provides an introduction to the properties and structure.

1.1 123 cuprates

One of the most intriguing properties of condensed matter is superconductivity (SC), which was first discovered in elemental mercury at 4.2 K by Heike Kamerlingh Onnes in 1911. The SC state is characterized by two fundamental properties: a vanishing *dc* resistance and the expulsion of an external magnetic field inside the material. The latter is known as the Meissner-Ochsenfeld effect. Induced currents in the surface of the superconductor screen the external magnetic field, leaving the interior field-free. If the magnetic field is sufficiently strong, the superconductor will return to its normal metallic state. Based on the behavior in an external magnetic field, two types of superconductors can be distinguished. In type I superconductors, the external field is

fully screened below the critical field H_c, while in type II superconductors above the lower critical field H_{c1}, the magnetic flux can partially penetrate through the sample in so-called flux vortices and a mixed state arises. If the magnetic field is further increased above the upper critical field H_{c2}, the mixed state breaks down into the normal state. The SC state can also be destroyed by a critical current density j_c. Both, the critical field and the critical current depend on the temperature and increase with decreasing temperatures below T_c.

In 1986 the discovery of SC with an onset $\approx$ 30 K in the system La-Ba-Cu-O started the era of high-temperature superconductors (HTSC) [9]. Only one year later, the discovery of another Cu compound, $YBa_2Cu_3O_{7-\delta}$ (YBCO) with T_c of 93 K, marked a groundbreaking advance towards technological usability. Such high transition temperatures provide access to the SC state by liquid nitrogen cooling [10]. Ever since, materials containing superconducting CuO_2 layers were at the forefront of fundamental and applied research. Based on the number of CuO_2 layers in their crystallographic unit cell, cuprates can be categorized into monolayer (e.g. $La_{2-x}Ba_xCuO_4$), bilayer (e.g. YBCO), and trilayer compounds (e.g. $HgBa_2Ca_2Cu_3O_{8+x}$). The latter compound holds the T_c record of the cuprate family with 134 K at ambient pressure and even up to 150 K at 150 kbar [11, 12].

Not only the uniqueness of the SC conducting state of cuprates, but also the diverse and unusual normal state properties have attracted considerable attention. The results of over 30 year of research can be summarized in a generic phase diagram for high-T_c cuprates (Fig. 1.6). The rich phase diagram results from the ability to obtain different properties by changing temperature, pressure and doping. The ongoing investigation of the interplay of different collective ordering phenomena is driven not least by the search for the superconducting pairing mechanism in cuprates. The advances in the synthesis of high-quality single crystals and thin films, as well as the development of new, sensitive

experimental instrumentation allowed scientists to expand the current understanding of cuprates.

In this thesis, the focus lies on the bilayer cuprate DyBCO, which is a member of the 123 family, whose parent compound is YBCO. The Y cation side can be substituted with many rare-earth elements, effecting T_c only slightly [13–15]. The reason for choosing Dy instead of Y is twofold. First, the ionic radii of Y^{3+} (1.159Å) and Dy^{3+} (1.167Å) are very similar and both 123 cuprates have a T_c of ≈ 93 K [13, 14, 16], but their magnetic properties differ. While Y^{3+} has a closed-shell electron configuration and no unpaired spins moments, Dy^{3+} has a partially filled $4f$ electron configuration ($4f^9$) and provides a strong, localized moment. Second, related to the low vapor pressure of Y, the thermal evaporation required in MBE growth is limited.

1.2 Crystal structure of 123 cuprates

In the following, the crystal structure of 123 cuprates is introduced in more detail [17–19]. Since the present work investigates DyBCO, the discussion uses the example of DyBCO.

The structure of DyBCO can be considered an oxygen deficient triple perovskite unit stacked along the c direction. The A sites are occupied by Ba and Dy in the sequence Ba-Dy-Ba, while the B sites are occupied by Cu. The unit cell can also be seen as a layered structure in which two CuO_2 plane layers are separated by a Dy layer and where two BaO layers separate the two CuO_2 planes from the CuO chain layer (Fig. 1.1).

The structure includes two inequivalent Cu sites. In the CuO_2 planes the Cu(2) ion is surrounded by 5 oxygen ions forming a square pyramid. The surrounding two O(2) and two O(3) ions form the square base and are slightly shifted towards the Dy ion, while the O(4) ion forms

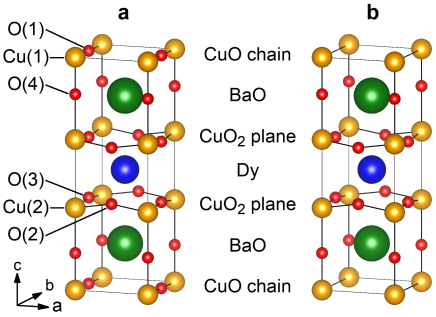

Figure 1.1: Crystal structure of $DyBa_2Cu_3O_{7-\delta}$ with (a) $\delta = 0$ and (b) $\delta = 1$. The different ions are marked in (a). Based on [20] created with [21].

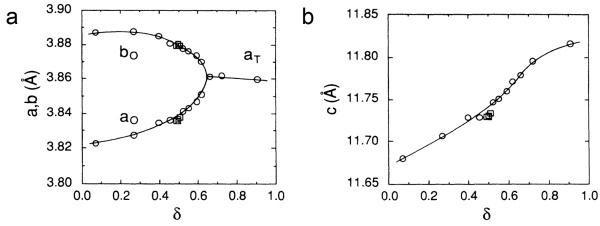

Figure 1.2: Lattice parameters in the orthorhombic phase (a_O,b_O) and in the tetragonal phase (a_T) of $YBa_2Cu_3O_{7-\delta}$, as well as the c-lattice parameter as a function of the oxygen content δ. From [17].

the tip of the pyramid, acting as a bridge to the CuO chain layer. The Cu(2)-O(2) and Cu(2)-O(3) distance (≈ 1.95Å) is shorter than the Cu(2)-O(4) distance ($\approx 2.3 - 2.45$Å) [18]. Therefore, the properties of the so-called CuO_2 plane is often of two-dimensional nature, such as the superconductivity or the charge ordering, which will be discussed in section 1.4.

The other Cu position, Cu(1), is in the chain layers and its coordination depends on the oxygen content of the compound. In the oxygen

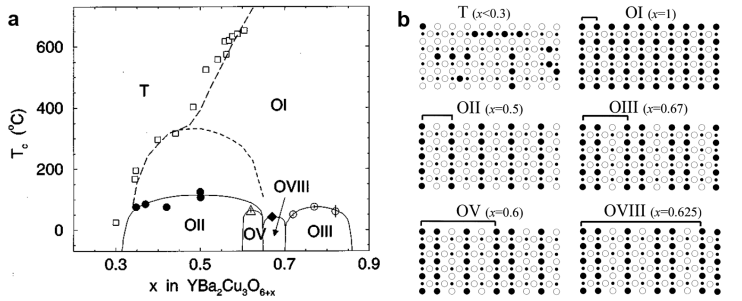

Figure 1.3: a) Phase diagram of the oxygen order in dependence of the oxygen content. From [19]. b) Sketch of oxygen order. From [25].

deficient compound ($\delta = 1$) the Cu(I) ion is surrounded by two O(4) ions along c, while the O(1) position is empty (Fig. 1.1b). The unit cell symmetry of the oxygen deficient DyBCO is therefore tetragonal ($a = b = 3.868$ Å, $c = 11.811$ Å for $\delta = 0.75$ [22]). By adding oxygen, the vacancies between the Cu(1) ions are filled with oxygen. Remarkably, oxygen only occupies the position between the Cu(1) ions along the b direction resulting in completely filled Cu(1)-O(1)-Cu(1) chains along b for $\delta = 0$. The uniaxial arrangement of the oxygen ions results in an orthorhombic symmetry ($a = 3.842$ Å, $b = 3.887$ Å, $c = 11.678$ Å for $\delta = 0.1$ [23]). The addition of oxygen also results in a decrease of the c-axis length (Fig. 1.2b). Hence the c-lattice parameter is frequently used to determine the oxygen content [17, 24].

A transition of the tetragonal structure to the orthorhombic structure is observed at an oxygen content of ≈ 6.35 (Fig. 1.2a) [17]. In the orthorhombic structure a periodic arrangement of full (f) and empty (e) CuO chains is formed and is named after its periodicity along a [19, 25]. The ortho-II order refers to a f-e, the ortho-III order to a f-f-e, the ortho-V to a f-f-e-f-e, and the ortho-VIII to a f-f-e-f-e-f-f-e sequence, respectively (Fig. 1.3).

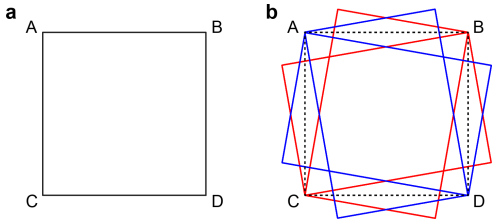

Figure 1.4: Sketch of in-plane lattice of (a) tetragonal structure (ABCD) and (b) orthorhombic twinned structure. The red domains arise from twinning along [110] and the blue domains from [1$\bar{1}$0]. Based on [26].

Regardless of the oxygen order, all orthorhombic structures undergo a phase transition towards the tetragonal structure at high temperatures. This is particularly important for single crystal and thin film synthesis, since the growth takes place at high temperatures and results in the formation of the tetragonal phase. Upon cooling in oxygen atmosphere, the transition to the orthorhombic structure takes place. During this transition, the symmetry is reduced: the mirror planes along (110) and (1$\bar{1}$0) as well as the C4 symmetry are lost. The orthorhombic structure evolves by forming twin domains where the [110] or [1$\bar{1}$0] axes of the tetragonal high-T and orthorhombic low-T phase align. Thereby four twin domains are formed [26] (Fig. 1.4). In crystals, detwinned domains can be obtained by applying uniaxial pressure at 350-400 °C [27, 28]. Since epitaxial thin films are often under biaxial pressure from the substrate, all four twin domains are present, unless substrates with a rectangular surface structure or with a large miscut angle are used [29, 30].

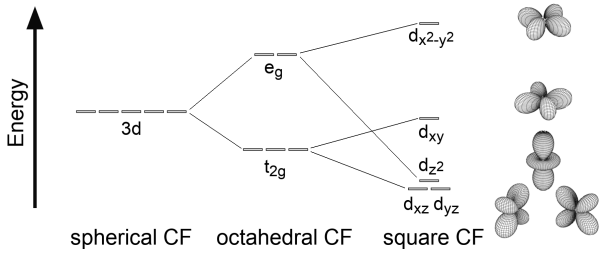

Figure 1.5: Sketch of crystal field (CF) splitting of the d orbitals, based on [16]. The shape of the d orbitals is also sketched.

1.3 Electronic structure of 123 cuprates

To understand the properties of 123 cuprates, it is often sufficient to consider only the CuO_2 planes and CuO chain layers. In the parent compound ($\delta = 1$), Cu has an overall, formal charge of +1.67, which can be redistributed to two Cu^{2+} ions in the CuO_2 planes and one Cu^{+} ion in the chain layer. In the fully oxygen-doped compound ($\delta = 0$), the overall Cu charge is +2.33. However, x-ray absorption spectroscopy revealed that the valence of Cu is not +III, but instead an O^{-} ion is formed [31].

Let us consider the electronic structure of the CuO_2 planes in more detail to understand this behavior. The Cu^{2+} ions have an electron configuration of [Ar] $3d^9$. In the ideal perovskite structure the Cu ions are surrounded by 6 oxygen ions forming an octahedron. This imposes an octahedral crystal field on the Cu ions which results in a splitting of the d orbitals into the t_{2g} and e_g levels. However, the Cu ions in the CuO_2 plane have a quadratic planar crystal field, generated by the four surrounding oxygen ions, which further splits the e_g and t_{2g} levels, as shown in Fig. 1.5.

The electrons in the d orbitals are not localized and can hop between different ions. Hence, the electronic correlations of electrons occupying

the same orbital need to be considered. This is accounted for in the Hubbard model, which describes the electronic state as the competition of on-site Coulomb repulsion U between electrons in the same d orbital at the same site, and a hopping integral t, which allows electrons to transfer from one site to another. If $t >> U$ the compound will be metallic, but if $U << t$ the electrons are localized and, depending on the band width, give rise to an insulating ground state. This simple model describes many transition metal (TM) oxides, but reaches its limits when the hybridization of the TM's $3d$ and oxygen $2p$ orbital is strong. Especially for the late $3d$ TMs, the energy of the partially filled e_g level(s) is close to the oxygen p level, resulting in a strong hybridization and an extension of the above mentioned Hubbard model [32]. Energetically, the oxygen p levels lie between the filled and empty TM's d levels, resulting in a charge-transfer insulator (for the undoped case), which is characterized by a corresponding charge transfer energy Δ [33].

This leads to a significant difference when considering the hole doping of cuprates, since doped holes reside in oxygen $2p$ orbitals, which will be discussed next.

The doping originates in the CuO chain layer, where additional oxygen is incorporated into the structure. Therefore, the CuO chain layer is also referred to as the "charge reservoir". By adding oxygen to the empty CuO chains, the Cu(1) valence increases from +I to +II. At an oxygen content larger than 6.25, chains with two O(1) ions around a Cu(1) ion are formed. Since Cu(1) already has a +II valence state, holes are doped into the O(1) ion, resulting formally in an O^- ion [34]. Above 6.25 oxygen content, the number of carriers increases with oxygen doping. The holes are then transferred from the CuO chain layers through the BaO buffer layer into the CuO_2 plane.

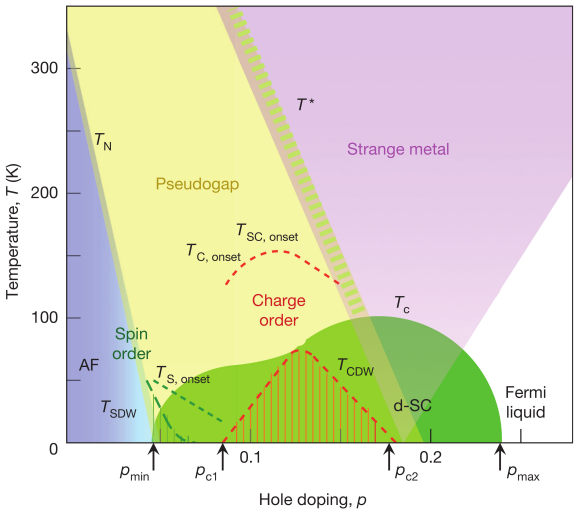

Figure 1.6: Generic phase diagram of hole doped cuprates in dependence of the doping p and the temperature. From [1].

1.4 Hole doping in 123 cuprates

123 cuprates have a rich phase diagram with many phenomena, which can be accessed by hole doping p. Starting from $\delta = p = 0$, the parent compound is an antiferromagnet and charge-transfer insulator at low temperature. Upon doping, the antiferromagnetic order is suppressed and the SC phase with T_c up to 93 K is observed.

123 cuprates are type II superconductors, characterized by a low coherence length, a high penetration depth of the magnetic field and a formation of flux vortices between H_{c1} and H_{c2}. The SC state appears in a range of hole doping of $\approx$ 0.04 to 0.27 forming the "superconducting dome" in the phase diagram. The doping with the maximal T_c of 93 K is called the optimal doping p_{opt} and divides between the so-called underdoped regime with $p < p_{opt}$ and the overdoped region

with $p > p_{opt}$. In the underdoped region around $p \approx 0.12$ a plateau is observed, where T_c decreases more slowly as a function of doping.
In the overdoped regime at high temperatures, the so-called strange-metal phase is formed, which, so far, remains insufficiently understood. In contrast to normal metals, 123 cuprates show a linear temperature dependence of the resistivity in this phase.
In the high-temperature regime of the underdoped cuprates a so-called pseudogap phase is observed. It is characterized by a partial gapping of the Fermi surface that can be directly observed by angle-resolved photoemission spectroscopy (ARPES). Investigations of $Bi_2Sr_2CaCu_2O_{8+\delta}$ (Bi2212), revealed similarities between the pseudogap and the superconducting gap: a gap in the anti-node region of the Fermi surface ((0,0) $\rightarrow$ (π,0)) and d-wave symmetry [35, 36]. This results in a picture, where, in the pseudogap region, preformed superconducting pairs (Cooper pairs) are formed, obtaining phase coherence only below T_c. Nevertheless, in a second picture, the pseudogap is an independent phase and competes with SC. Evidence for this interpretation was also found in ARPES on Bi2212: the antinodal gap depends on the doping, while the gap near the nodes is independent of the doping [37]. Furthermore, the gap at the anti-nodal and near-nodal region shows different temperature dependencies, indicating different origins and consequently different phenomena.
In the underdoped regime at low temperatures the formation of a charge density wave (CDW) was first observed by resonant inelastic x-ray scattering at the Cu L_3 edge for doping between 0.09 and 0.13, and was interpreted by charge ordering in the CuO_2 planes [38]. The CDW phase forms a dome with an onset between 100 and 150 K depending on the doping (Fig. 1.7a). The temperature dependence further shows a maximum intensity at T_c, which points to a competition with the SC state. The competition is also seen by applying a magnetic field, and thereby suppressing SC and recovering the CDW scattering peak

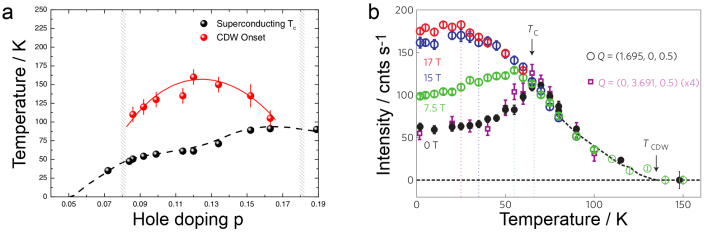

Figure 1.7: (a) Doping dependence of the 2D CDW onset temperature and the superconducting T_c in YBCO. From [42]. (b) Temperature dependence of the 2D CDW peak intensity at different applied magnetic fields. From [39].

intensity (Fig. 1.7b) [39]. While the CDW peak intensity above T_c is independent of the field, the intensity increases below T_c when a field is applied [40, 41]. The CDW has a moderate in-plane and very small out-of-plane correlation length, indicative of a two-dimensional character (2D CDW).

It has recently been shown that the in-plane correlation can be enhanced and a correlation along the c direction is obtained (3D CDW) by applying a large magnetic field (< 17 T) [2, 43]. This 3D CDW appears in addition to the 2D CDW. Both charge ordered states have a similar in-plane wave vector of ≈ 0.31 r.l.u. and can be distinguished by RXS, where the 2D CDW intensity is spread along l with a maximum at half-integer values, while the 3D CDW has sharp peaks at integer l values.

The required high magnetic fields limit the experimental methods and facilities to access this 3D order state. The need for high magnetic fields has become obsolete with the observation of 3D CDW stabilization by application of uniaxial strain along the a-axis [3]. In addition, it has been shown that the 3D CDW is present in YBCO thin films without the application of magnetic fields or external strain [4]. However, the

origin of the 3D CDW remains unclear. In single crystals the 3D CDW involves only the Cu(2) ions from the CuO_2 planes with an onset temperature similar to the 2D CDW, while the 3D CDW in YBCO films also has contributions from the Cu(1) ions of the CuO chain layers and is stable until room temperature. In thin films, the involvement of the Cu ions from the CuO chain layers in the CDW formation points to the importance of the structure, which can be systematically varied in epitaxial thin films. More generally, the stabilization of the 3D CDW in thin films demonstrates the advantages of heteroepitaxy to create meta-stable phases and provide easy access to ordered states.

Chapter 2

Growth of thin films

In this chapter, we discuss theoretical and technical aspects of thin film growth. After a general introduction to concepts of thin film growth, the used MBE setup is described in section 2.3.

Thin films are a layer of material with a thickness in the nanometer range. Usually, thin films are deposited onto a much thicker supporting matrix, the substrate. The obtained film can be amorphous, poly- or single-crystalline and composed of both organic or inorganic compounds. For the purpose of this work, only single-crystalline films of metal oxide deposited on single crystalline substrates are addressed. The film can grow epitaxially, meaning that it will follow the structure of the substrate, if the lattice structure and lattice constants of both the substrate and the film material are similar.
In practice, however, the lattice structure of the substrate and film material usually differ. The mismatch of the two materials is characterized by the lattice misfit ϵ:

$$\epsilon = \frac{a_s - a_f}{a_s} \ , \tag{2.1}$$

where a_s and a_f refer to the in-plane lattice parameters of the substrate and the film respectively. For the substrate and the film the surface orientation needs to be taken into account. For example, a (110) cut crystal has the in-plane axes along $[1\bar{1}0]$ and [001]. In complex systems, the lattice is usually transformed into the pseudocubic (pc) symmetry and the corresponding pseudocubic substrate and film lattice parameters are used to calculate the misfit.

Depending on the degree of the lattice mismatch, the film can adapt to the substrate structure, which will result in epitaxial strain. This strain can be either tensile ($\epsilon > 0$) or compressive ($\epsilon < 0$) and has a similar effect as pressure applied along the in-plane lattice parameters. With increasing film thickness, the epitaxial strain is slowly released via the formation of misfit dislocations until the film resumes the bulk-like lattice above a critical thickness. By selecting different substrates and substrate cuts, the epitaxial strain can be systematically tuned. In case of a large mismatch, the film can not adopt the lattice structure of the substrate and will either form defects or resume the bulk lattice or decompose into different compounds.

Thin films allow investigations of the effect of confinement and interfaces. In many cases, the properties of thin films and heterostructures, where layers of different materials are deposited onto each other, differ from the corresponding bulk properties. A famous example is the combination of the insulating $SrTiO_3$ with the insulating $LaAlO_3$ to form a two-dimensional electron gas that is superconducting at very low temperatures [44, 45]. The effect of epitaxial strain can be seen in $PrNiO_3$, which, in bulk, exhibits a metal-insulator-transition (MIT) at 135 K [46]. While films under tensile strain still show almost no change in the MIT, films under compressive strain remain metallic even to lowest temperatures [47, 48]. Another example is $La_{1.9}Sr_{0.1}CuO_4$, which, in bulk, becomes superconducting at 25 K, while thin films under compressive strain have a T_c of 49 K [49].

2.1 Deposition methods

Thin films are synthesized by using various techniques. The underlying concept can be divided into chemical and physical deposition. Chemical deposition involves the chemical reaction of a precursor to form the film, while physical deposition involves the change of state. Techniques where the film is created from vapor of the material in a vacuum setup are referred to as physical vapor deposition (PVD).
The most common PVD techniques used for the thin film growth are sputtering, pulsed laser deposition (PLD) and molecular beam epitaxy (MBE). In PLD, the material is ablated with a high energy laser, creating a plasma. In sputtering, the material is bombarded with an ion or atom beam to create vapor. For both techniques, a target with the stoichiometric composition of the desired material is used. In MBE, elements are usually evaporated from individual Knudsen effusion cells, creating an additional degree of freedom for the deposited material composition. In contrast to PLD and sputtering, a high vacuum is needed to ensure the ballistic transport between the effusion cells and the substrate.
Each deposition method has its advantages and disadvantages. In PLD and sputtering, the usage of a target enables reproducible film growth. Nevertheless, the film quality depends on the target stoichiometry, requiring a precise composition. In MBE growth, the stoichiometric freedom can be a blessing and a curse. It allows for the modification of the stoichiometry during deposition, the introduction of off-stoichiometry as well as systematic doping with other elements. On the other hand, it limits the reproducibility and introduces deviations from the desired stoichiometry.
Depending on the used technique, the vaporized atoms arriving at the

substrate have a characteristic kinetic energy. The plasma plume in PLD results in high kinetic energy, while the evaporation of the different elements in MBE is connected to low kinetic energy. The energy of atoms vaporized by sputtering is in between PLD and MBE. High energies of the atoms threaten to damage the film interface, which is particularly crucial in heterostructures. The comparison of PLD and MBE growth of $LaNiO_3$-$LaAlO_3$ heterostructures revealed, that the interfaces of MBE grown structures are sharper, while the cation stoichiometry is more difficult to control, which introduces defects [50]. For this thesis, MBE growth was chosen due to the ability to obtain high quality interfaces. For the purpose of overcoming the disadvantages of the stoichiometric freedom and in order to use it to suppress defects, *in-situ* feedback systems have been installed, which will be discussed in section 2.3.

2.2 Growth dynamics

Thin film growth is governed by kinetics and thermodynamics. The latter address the interface energies, particularly the strength of the bonds between the deposited atoms and the substrate. Depending on the bond strength, three different growth modes can be distinguished [51]. If the bonds between the deposited atoms are weaker than the bonds with the substrate, the deposited atoms prefer to complete a full layer before the next layer is started. As a result, the growth is two-dimensional and is then referred to as the layer-by-layer or Frank-van-der-Merve growth mode. In contrast, if the bonds between the deposited atoms are stronger than the bonds to the substrate, the deposited atoms prefer to nucleate and form islands. This growth mode is called the Island or Vollmer-Weber mode. The intermediate situation between the two extreme cases is called the Layer-plus-Island

or Stranski-Krastanov mode. After an initial two dimensional growth, three-dimensional islands start forming.
In addition to the thermodynamic considerations, kinetic limitations arise from the surface diffusion of the deposited atoms. Single-crystalline substrate surfaces are not perfectly flat and actually posses a slight miscut angle which gives rise to step edges between flat terraces. Atoms reaching the step edge and crossing to the next lower terrace need to overcome an additional energy barrier, the so called Ehrlich-Schwoebel barrier. Depending on the intralayer diffusion (on the terrace) and interlayer diffusion (across a step edge), three kinetic growth modes can be distinguished [51].
The step-flow mode is obtained, when the intralayer diffusion is high. Then the deposited atoms can diffuse to the step edge, which is thermodynamically favored due to the additional bonds with the step. When the diffusion length of the deposited atoms is shorter than the terrace width, islands will form on top of the terraces. If the interlayer diffusion is high enough for a deposited atom to reach the edge of an island, drop to the lower terrace and complete one layer before the next layer is started, it is called layer-by-layer growth. If the interlayer diffusion is lower, the deposited atoms can not complete the previous layer and form new layers. As a result, the islands grow and the multilayer growth is obtained.
In MBE growth of complex oxides, the different growth modes can be controlled by changing the substrate temperature, the deposition rate of the constituent element and the oxidant background pressure. Compared to PLD growth, the deposition rate is lower, favoring the layer-by-layer growth mode. Moreover, an increase of the temperature enhances the surface mobility and consequently supports the layer-by-layer mode. Nevertheless, the temperature range is limited by the MBE heating system as well as thermodynamics of the phase stability. For thin film growth, the phase diagram usually has to be investigated

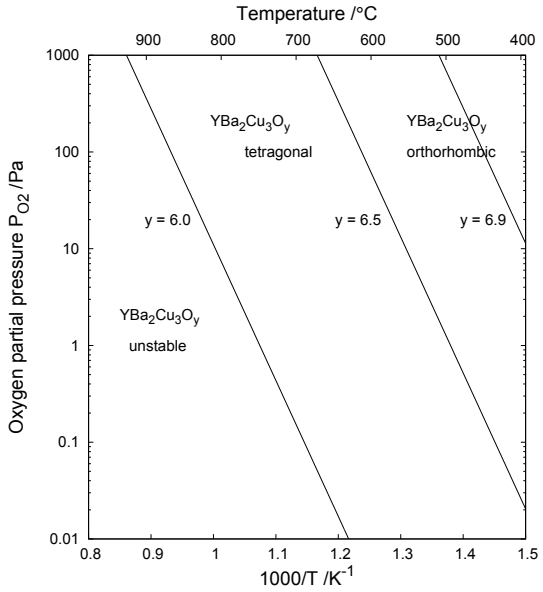

Figure 2.1: Pressure-temperature phase diagram for $YBa_2Cu_3O_y$ indicating the critical stability line at y = 6.0, the tetragonal-orthorhombic transition at y = 6.5 and stability for y = 6.9. Based on [52].

by systematic variations of the growth parameters pressure, temperature and stoichiometry. As a decent starting point, existing work on related materials, e.g. YBCO as the parent compound of DyBCO, can be used (Fig. 2.1). In MBE growth, the ballistic transport needs to be ensured, which limits the background pressure to 10^{-4} torr and consequently restricts the accessible range of the phase diagram. The pressure limitation and the need to oxidize the pure elements to form the corresponding metal oxides require a strong oxidation agent. Common oxidation agents are plasma activated oxygen or ozone [53–55].

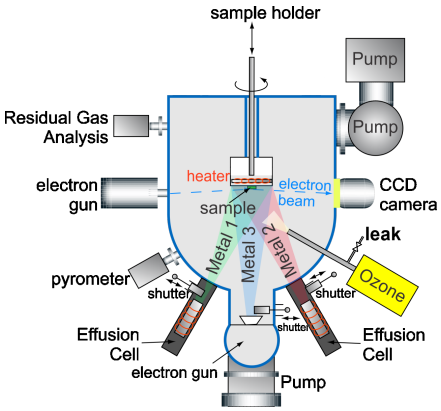

Figure 2.2: Sketch of the used MBE chamber based on [56].

Until a desired film quality is achieved, numerous optimization steps of the growth parameters as well as extensive *ex-situ* characterization are required.

2.3 Oxide MBE

After the discussion of theoretical models and basic principles of thin film growth, this section focuses on technical and practical aspects of complex oxide thin film growth using MBE.

The setup used for this thesis is an ozone assisted MBE built by DCA Instruments [56]. It consists of a central distribution unit, operated in high vacuum, which is connected to two identical growth chambers, a load lock to load substrates and an eight slot storage unit. The general layout of the deposition chamber is sketched in Fig. 2.2.

In MBE growth, the ballistic transport regime limits the background pressure. Hence, ozone is used as the oxidization agent. Prior to the film growth, ozone is collected with an ozone generator and stored

in a liquid N_2 cooled still filled with silica gel. During film growth, the ozone is evaporated by controlled heating and delivered into the growth chamber. The ozone nozzle is directed onto the substrate and locally creates a high almost pure ozone atmosphere on the substrate surface. The corresponding atmosphere in the chamber is continuously monitored with a residual gas analyzer (RGA). Since it is located on the backside of the substrate holder, the detected composition does not reflect the actual atmosphere at the substrate. An additional leak valve attached to the ozone delivery line allows the increase of the ozone partial pressure ($p(O_3)$) measured by the RGA (Fig. 2.3). Strikingly, all gases increased $p(O_3)$ dramatically up to one order of magnitude. Pure N_2 and air cause the highest increase of the ozone partial pressure. Although the valve position for the highest leak was similar for all gases, the total pressure in the chamber differs, indicating an inaccuracy of the valve. Therefore, the small difference between the gases can also be associated with the total pressure. The origin of the $p(O_3)$ enhancement was not investigated further due to the unknown atmosphere composition at the nozzle outlet, which could only be determined by changing the RGA position.

The substrates are mounted upside down in the chamber and heated with a resistive heater. Prior to loading, the backside of the substrate is painted with $SrRuO_3$ powder dispersed in iso-propanol, to increase the radiation absorption and thereby making the heating more efficient. The temperature of the substrate is monitored with a thermocouple, placed between the heater and the substrate, as well as with the pyrometer focused on the surface of the substrate. The corresponding emissivity factor for each substrate is determined by calibration measurements in a special oven setup, where a thermocouple is attached to the backside of the substrate.

The elements are evaporated from effusion cells, which are equipped with computer operated shutters for a precise control. For each element,

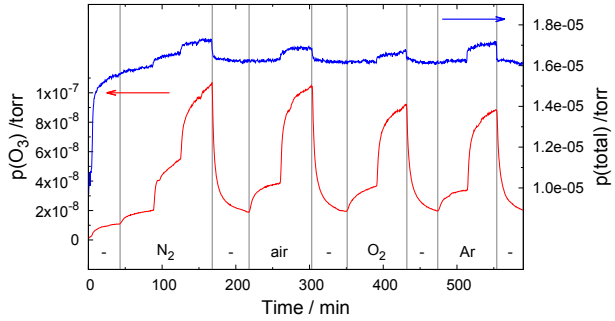

Figure 2.3: Effect of the leak valve of the ozone supply line on the partial pressure of ozone (red) and the total pressure (blue). For N_2, three valve positions were investigated, while for air, O_2 and Ar only two positions were used. Between the different gases, the leak was closed.

a different temperature is needed to obtain a usable vapor pressure and consequently a stable flux. Therefore, different cell layouts and crucibles are used. While Ba is sublimated at 400-500 °C, Dy is sublimated above 1200 °C and requires a high temperature cell. Cu is evaporated at ≈ 1150 °C in a dual filament cell to prevent the condensation of Cu on the opening of the crucible and thereby blocking the beam.

The effusion cells are used in a constant temperature mode, where the heating power is adjusted accordingly. When the shutter is closed, radiation is reflected back into the crucible and the material temperature is raised. Upon opening the shutter, the initial flux is higher until a constant value is obtained [57–59]. In addition, increasing flux over time was reported, assigned to compensation of the temperature decrease upon opening of the shutter [60]. The shutter transient depends on the element and the closed shutter time before opening. Values above 25 %

flux increase were reported for Ga [58]. However, the transient can be reduced, if the distance between shutter and the crucible is increased. The shutter transient is different for every setup and therefore is a characteristic property for each cell and every MBE setup.
Finally, during the growth, the shutters of the effusion cells are computer controlled and can be manually corrected by either extending or shortening the opening time. Based on the shutter operation, two basic MBE modes can be distinguished. When all required shutters are opened simultaneously, it is called co-deposition. If one cell is opened after another and consequently one atomic layer is deposited after another, it is referred to as atomic-layer-by-layer MBE (ALL-MBE). The obtained *in-situ* feedback can be related to one specific cell and corresponding adjustments to the stoichiometry are possible. This method is well suited for complex oxides which have layered crystal structures. Hence, the ALL-MBE growth mode was used in this thesis. It should also be mentioned that the operation in the intermediate stage is possible as well, where some cells remain open continuously while other cells are alternated in a pattern.
Regardless of the growth mode, prior to the deposition, the flux of each effusion cell has to be calibrated and a feedback system is required during growth. For the used MBE setup, the initial calibration is obtained with a quartz crystal micro balance (QCM) and the deposition is monitored using *in-situ* RHEED. Both methods are further explained in the next two sections.

2.3.1 Quartz crystal microbalance

The used element flux in MBE growth is very small and therefore a sensitive method to determine the deposited material mass must be used. A quartz crystal microbalance (QCM) uses a quartz resonator.

Upon deposition of material onto the surface of the quartz, the oscillation frequency shifts. The Sauerbrey equation relates the shift of the oscillation frequency and the change of mass per area: [61]

$$\Delta f = -C_f \cdot \Delta m \ . \tag{2.2}$$

The crystal sensitivity factor C_f is a characteristic property for the used quartz crystal. A tooling factor accounts for the angle between element beam and surface of quartz, and a sticking coefficient for the amount of molecules sticking to the quartz surface. Finally, the molar mass of the deposited molecule must be considered to obtain an atom flux. Working in ozone background, several oxidation states can be obtained. Therefore, the determination of the molar mass is connected with an uncertainty. In order to avoid the unknown oxidation state, the initial calibration can be done in vacuum and the molar mass can be assumed to be equal to the element mass. The disadvantage is the neglect of oxygen. Upon ozone exposure, metal oxides form on the material surface in the crucible. This reduces the surface area for evaporation or sublimation and therefore reduces the flux. As a consequence, there is no perfect calibration and the disadvantage of the selected method should always be considered.
The oscillator's frequency is temperature-dependent and a change of temperature also induces a shift of the frequency. By using different cuts of quartz crystals, the temperature effect can be minimized for the desired temperature range. Usually, QCMs are water cooled to obtain a nearly constant quartz temperature. However, due to the displacement of the heat reservoir from the quartz, small temperature offsets can occur. Therefore, the standard QCM was replaced with a temperature controlled version, where the temperature of the heat reservoir is measured and where the coolant flow - in this case air - can be adjusted. There is still a temperature difference between the measured temperature and the actual quartz temperature, but a

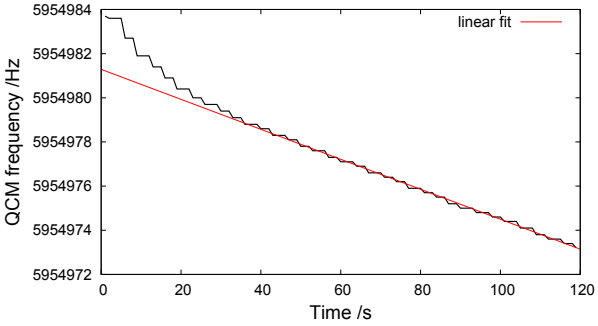

Figure 2.4: Calibration curve for an effusion cell. The initial shift is higher due to the shutter transient effect. The flux can be assumed to be constant after 40 s and a good fit with a linear relation is observed (red line).

quantitative analysis is possible, allowing a better understanding of the calibration.

For the calibration of an effusion cell, the quartz frequency is measured during the deposition of the selected element. The shift of frequency is fitted with a linear equation and the slope equals Δf in the Sauerbrey equation. Fig. 2.4 shows a typical frequency curve, where deviations from the expected linear approximation are visible. The large deviation in the first seconds are related to transient effects after opening the shutter, where the flux is higher. After an equilibrium formed in the crucible, the flux is almost constant and a linear decrease of the quartz frequency is observed. A second common deviation is observed due to irregular cooling or heating of the quartz. These obstructions can be avoided through a precise heat control and a low flux, which decreases the shutter transient effect.

The calibration is repeated until the slope remains within a 10 % range. With the tooling factor T, sticking coefficient S, the molar mass M

and Eq. 2.2, the flux can be calculated:

$$flux = \frac{(\frac{-\Delta f}{\Delta t}) \cdot T \cdot S \cdot C_f}{M} \ . \tag{2.3}$$

After the calibration, the corresponding flux is assumed to be constant. Nevertheless, calibration after the growth frequently revealed a decrease of the flux arising from the consumption and the oxidation of the source material. Therefore, stoichiometry corrections during growth must be expected and *in-situ* monitoring is required.

2.3.2 In-situ RHEED

The growth of the thin film is monitored *in-situ* using reflection high-energy electron diffraction (RHEED). An electron beam with energies of 20-40 keV, in the used setup 25 keV, is focused on the substrate surface in a grazing incident angle (1-5 °), resulting in a low penetration depth and a high surface sensitivity. The electrons are reflected and diffracted by the surface and are detected on a fluorescent screen.
Due to the low penetration depth, only the in-plane lattice is probed. Therefore, the 3D reciprocal lattice points become 2D reciprocal lattice rods. For well ordered surfaces, the rods are sharp, while imperfections result in broadening. The high electron energy results in a large Ewald sphere, which will cut the reciprocal rods at a grazing angle. As a result, for a real two dimensional surface, the observed RHEED pattern at the fluorescent screen consists of streaks instead of spots. Despite the surface sensitivity, the electrons can also transmit through small islands, which will give rise to spots in the RHEED pattern. As a consequence, RHEED can be used to distinguish between flat surfaces (streaks) and islands (spots). One exception is observed for perfect surfaces, where the rods are very sharp and the Ewald sphere cuts them in sharp spots. In contrast to the island growth, these spots are arranged in a circle.

During growth, surface reconstruction can take place giving rise to additional streaks or a completely different pattern. The distance between streaks and/or spots can be used to determine the in-plane lattice parameters. By determining the relation between the streak spacing and the crystal lattice of a reference, for example the substrate, the lattice parameters of a new pattern can be extracted (for the specific substrate-fluorescent-screen distance and electron energy).

In addition to the interpretation of single RHEED patterns, the intensity of the diffracted electrons can be monitored over time. In a simple picture, the intensity of the reflected electron is high, if the surface is flat. When atoms are deposited onto the surface, the roughness increases and the monitored electron intensity decreases due to diffuse scattering. When the surface is half covered, the intensity will be lowest. Further deposition of atoms fills the gaps in the surface and thereby increases the electron intensity until the surface is flat again. Thus, the period of the observed intensity oscillation represents the growth of a single monolayer.

Depending on the growth mode, deviations from this simple picture are expected. The described behavior is only valid in the layer-by-layer growth mode, where the new layer grows between several one-layer high islands and the next layer only forms once the previous layer is completed. In the step-flow mode, where only one step is present on the surface, the deposited atoms will bond to the step and thereby move the step across the surface until the layer is completed and the next layer with a new step nucleates. The reflection will not be affected by the moving step and hence, no intensity oscillation is observed. In the island growth mode, diffuse scattering on the islands will decrease the reflected beam intensity. While the period of the oscillation still matches the formation of a monolayer, the amplitude will be dampened. In the layer-plus-island growth mode, the initial ideal oscillation will transform to a dampened oscillation when the islands start forming.

The simple assumption that the maximum RHEED intensity corresponds to the completion of a layer might not always be true and the maximum could also occur when the layer is not completed [62].

2.3.3 Growth optimization

Successful synthesis of complex oxides depends on many parameters. For MBE growth, it is necessary to obtain the optimal substrate temperature, the right oxidant background pressure and to provide the exact amount of constituent atoms to form the desired phase. Although the primary information during the growth is obtained by the *in-situ* RHEED monitoring, the formation of the targeted phase is confirmed by *ex-situ* characterization. Common techniques are x-ray diffraction for phase identification, atomic force microscopy for surface morphology imaging and transport measurements for specific properties like resistivity.

The stability of complex oxides depends on the pressure vs temperature phase diagram. A higher substrate temperature increases the mobility of the deposited atoms on the surface and is therefore better suited for the formation of high quality crystal structure. However, higher temperatures also require higher oxidation conditions. Therefore, systematic changes of pressure and temperature are necessary to find the best growth window. In case of a low background pressure and a high temperature for Cu based complex oxides, only Cu^{1+} compounds are formed, while in good conditions also Cu^{2+} is stabilized.

In addition to the optimization of the growth window, the stoichiometry needs to be addressed since non-stoichiometry results in formation of impurity phases. This is accomplished during growth by the RHEED intensity monitoring. For new materials, the assignment of a specific RHEED pattern to a certain phase is unknown and needs to be ex-

plored. By adjusting the shutter times in such a way, that one set of diffraction spots in enhanced, individual phases can be identified using post-growth characterization. The obtained RHEED pattern database is then used to identify defects early in growth and to adjust the stoichiometry to avoid defect formation. For simple perovskites with the composition ABO_3, only the shutter time of one effusion cell is changed, usually the least stable cell, while the other remains constant. For more complex oxides the interplay of the different elements makes the stoichiometry adjustments more complicated, especially since more impurity phases are possible.

Numerous film growths and *ex-situ* quality assessment are required in order to obtain the ideal growth conditions and the best stoichiometry control.

Chapter 3

X-ray techniques

X-ray techniques are powerful tools to study the crystal structure of materials in a non-destructive way. Since the discovery of x-rays by Wilhelm Conrad Röntgen in 1895, the application of x-rays as well as the theoretical understanding of their interaction with matter has improved immensely. Because of their wide usage as a standard characterization tool, their history as well as the fundamental principles are subject to many textbooks. Therefore, the basic principles of x-ray scattering are only briefly addressed in the following section, while a more detailed explanation can be found for example in [63]. After some theoretical considerations, the relevant techniques involving x-rays are presented.

3.1 Basic principles

In a crystalline material, the atoms are arranged periodically in space (crystal lattice). The smallest repeating unit which has the full symmetry of the crystal is the unit cell. It is defined by its principal axes

($\mathbf{a}_1$, $\mathbf{a}_2$, $\mathbf{a}_3$), whose lengths are called lattice constants, and the angles between them (α,β,γ). The unit cell is reproduced by translation along its principal axes. The position of an atom $\mathbf{r}_i$ is described by the lattice vector $\mathbf{R}_n$, which indicates the position of the origin of its unit cell and is a linear combination of the principal axes, plus the vector $\mathbf{r}_j$, which indicates the position of the atom within the unit cell:

$$\mathbf{r}_i = \mathbf{R}_n + \mathbf{r}_j = n_1\ \mathbf{a}_1 + n_2\ \mathbf{a}_2 + n_3\ \mathbf{a}_3 + \mathbf{r}_j\ . \tag{3.1}$$

In addition to the real space lattice, the reciprocal lattice plays a fundamental role in the interaction with x-rays. Based on the real space lattice, the reciprocal lattice $\mathbf{G}$ can be constructed as

$$\mathbf{G} = m_1\ \mathbf{a}_1^* + m_2\ \mathbf{a}_2^* + m_3\ \mathbf{a}_3^* \tag{3.2}$$

$$\begin{aligned} \mathbf{a}_1^* &= 2\pi \frac{\mathbf{a}_2 \times \mathbf{a}_3}{\mathbf{a}_1 \cdot (\mathbf{a}_2 \times \mathbf{a}_3)} \\ \mathbf{a}_2^* &= 2\pi \frac{\mathbf{a}_3 \times \mathbf{a}_1}{\mathbf{a}_1 \cdot (\mathbf{a}_2 \times \mathbf{a}_3)} \\ \mathbf{a}_3^* &= 2\pi \frac{\mathbf{a}_1 \times \mathbf{a}_2}{\mathbf{a}_1 \cdot (\mathbf{a}_2 \times \mathbf{a}_3)}\ . \end{aligned} \tag{3.3}$$

For the interaction with x-rays, crystals can be considered parallel planes of atoms, separated by the distance d. In a simplified picture, incident x-rays, with an angle θ relative to the surface, get reflected from those planes. Only if the path difference of the x-rays reflected from successive planes is an integer multiple of the wavelength λ, constructive interference will be observed. These conditions result in the well-known Bragg's law:

$$n \cdot \lambda = 2d \cdot sin(\theta)\ . \tag{3.4}$$

X-rays are electromagnetic waves characterized by a wavelength λ in the range from 0.1 to 100 Å. From the incoming wave $\mathbf{k}_{in}$ and the scattered wave $\mathbf{k}_{scat}$ results a wave vector transfer $\mathbf{Q}$, which is also called scattering vector, and is defined by $\mathbf{Q} = \mathbf{k}_{in} - \mathbf{k}_{scat}$. The value

of the scattering vector $\mathbf{Q}$ can be evaluated knowing the wavelength λ and the angle between $\mathbf{k}_{in}$ and $\mathbf{k}_{scat}$ (2θ):

$$\mathbf{Q} = 2|\mathbf{k}|sin\theta = \frac{4\pi}{\lambda}sin\theta \ . \tag{3.5}$$

In order to observe a constructive interference of the scattered waves, $\mathbf{Q}$ must be a reciprocal space vector $\mathbf{G_{hkl}}$. This is known as the Laue condition $\mathbf{Q} = \mathbf{G}$.

The indices ($h\ k\ l$) are Miller indices that describe the family of lattice planes by which the x-rays are scattered. The corresponding reciprocal lattice vector $\mathbf{G}_{hkl}$ is perpendicular to the ($h\ k\ l$) planes, whose spacing d_{hkl} is given by:

$$d_{hkl} = \frac{2\pi}{|\mathbf{G}_{hkl}|} \ . \tag{3.6}$$

In a more detailed perspective, x-rays interact with atoms by scattering and absorption. In the case of scattering, the electrons start vibrating and emit a spherical wave. For conventional x-ray scattering this process is elastic, meaning that the wavelength of the scattered wave is equal to the incident one ($|\mathbf{k}_{in}| = |\mathbf{k}_{scat}| = |\mathbf{k}|$).

The scattered radiation is the superposition of the contribution of each electron in an atom with density $\rho(\mathbf{r})$. This causes a phase shift $\mathbf{Q} \cdot \mathbf{r}$ and consequently an interference phenomenon. The phase shift is obtained by integrating the factor $e^{i\mathbf{Qr}}$ for every volume element $d\mathbf{r}$:

$$f^0(\mathbf{Q}) = \int \rho(\mathbf{r}) e^{i\mathbf{Qr}} d\mathbf{r} \ . \tag{3.7}$$

$f^0(\mathbf{Q})$ is known as the atomic form factor. In order to obtain the scattering length, which quantifies the ability to scatter x-rays, $f^0(\mathbf{Q})$ has to be multiplied by the Thompson scattering length of an electron r_0 and by -1 to account for the π phase shift between the incident and scattered waves.

The scattering amplitude $F(\mathbf{Q})$ equals the sum of the phase shift of all atoms. Using Eq. 3.1, it can be decomposed into the product of

two terms:

$$\begin{aligned} F(\mathbf{Q}) &= \sum_{\mathbf{R}_n+\mathbf{r}_j}^{\text{all atoms}} f_j(\mathbf{Q}) e^{i\mathbf{Q}(\mathbf{R}_n+\mathbf{r}_j)} \\ &= \sum_j f_j(\mathbf{Q}) e^{i\mathbf{Q}\mathbf{r}_j} \quad \sum_n^N e^{i\mathbf{Q}\mathbf{R}_n} \ . \end{aligned} \tag{3.8}$$

The first term is the unit cell structure factor. The second term (lattice term) accounts for the phase shift between the N unit cells: it will cancel out unless $\mathbf{QR}_n = 2\pi n$, with n being an integer, where constructive interference occurs. This condition is fulfilled if $\mathbf{Q}$ is a reciprocal space vector $\mathbf{G_{hkl}}$ (Laue condition).

In addition to the realization of the Laue condition, the unit cell structure factor (first term in Eq. 3.8) needs to be considered in order to determine whether a reflection can be observed. Depending on the unit cell symmetry, certain (h k l) combinations have a vanishing structure factor, resulting in a forbidden reflection. Only allowed reflections, which follow the selection rules for the unit cell symmetry, can be detected.

In bulk crystals, the number of unit cells is enormous, resulting in a delta function for the lattice term in Eq. 3.8. However, the thickness in thin films is limited, resulting in only N unit cells in the direction perpendicular to the surface. In a one-dimensional approach, the lattice term along the direction z can be written as

$$S_N(Q) = \sum_n^{N-1} e^{iQnz} \ , \tag{3.9}$$

which, after the summation, has the form

$$|S_N(Q)| = \left| \frac{sin(NQz/2)}{sin(Qz/2)} \right| \ . \tag{3.10}$$

For an infinite crystal ($N \to \infty$), this is equivalent to a delta function, while for N unit cells, an oscillation correlated to the thickness is

observed. This results in a broadening of the strong reflections at $\mathbf{Q} = \mathbf{G}_{hkl}$ and generates weaker maxima on the side. These additional peaks around the main reflection are called Laue fringes and only appear in smooth films, thereby making them an indicator of the film quality.

Another deviation from the scattering of a perfect crystal arises from the finite dimensions of the substrate and film. For infinite dimensions, which can be assumed for the in-plane components parallel to the surface (x,y), the corresponding lattice term produces a delta function. However, the direction normal to the surface (z) exhibits a sharp step at the surface, resulting in an amplitude of the diffraction peaks proportional to $\frac{1}{Q_z}$. The resulting streaks are called crystal truncation rods (CTR).

So far, the electrons surrounding the atom have been treated as free electrons resulting in the so called Thomson scattering. However, the electrons around the atom are bound to the core and occupy distinct energy levels. Therefore, the atomic form factor is expanded with dispersion corrections accounting for the changes generated by the bound electrons:

$$f(\mathbf{Q}, E) = f^0(\mathbf{Q}) + f'(E) + if''(E) \ . \tag{3.11}$$

The dispersion terms f' and f'' depend only on the photon energy for a particular ion. If the x-ray energy differs greatly from the binding energy, the free electron approximation is valid. However, if the x-ray energy is close to an absorption edge, the bound nature of the electrons needs to be considered. The electrons respond to the x-rays as dampened oscillators with the resonance frequency ω_s. The term f' corresponds to a change in amplitude, while f'' accounts for a phase shift. Both terms exhibit maximum values when the x-ray energy matches a well-defined electronic transition between an occupied and an empty level.

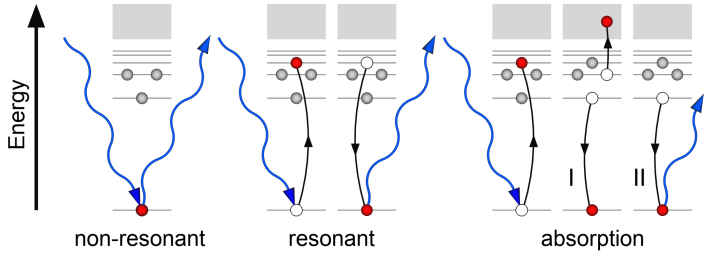

Figure 3.1: Sketch of the interaction of x-rays with atoms. Based on the x-ray energy, they can scatter non-resonantly or resonantly. X-rays can also be absorbed where the formed hole is filled either by Auger electron emission (I) or by fluorescence (II). Based on [63].

When the x-ray energy is tuned to a transition between an occupied and unoccupied electronic level, resonance is obtained. These characteristic energies are called absorption edges and are named based on the energy level that gets excited. The K edge refers to the excitation of a $1s$ level, L_1 edge to $2s$ level, and the L_2 and L_3 edge to $2p$ levels, which split into $2p_{\frac{3}{2}}$ and $2p_{\frac{1}{2}}$ due to spin-orbit coupling.
In x-ray absorption spectroscopy (XAS), the core electrons are excited into an unoccupied level, which allows the detection of the level occupation. The generated core hole is filled very quickly with the same electron (elastic scattering) or with another. This process results in the emission of another x-ray (fluorescence, resonant scattering) and the emission of secondary electrons, called Auger electrons. The absorption can then be detected either by measuring the current that fills the Auger electron holes (total electron yield) or by measuring the emitted photons (fluorescence yield). The scattering with x-ray energy resonant to the absorption edge is called resonant elastic x-ray scattering (REXS) and is characterized by high sensitivity to the electronic configuration of the atoms related to the scattering process.

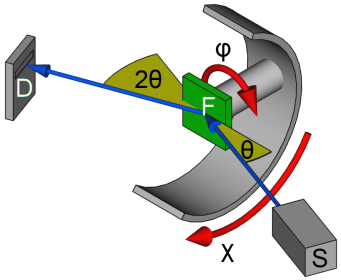

Figure 3.2: Sketch of the scattering geometry in the used four-circle diffractometer with the x-ray source (S), the sample / thin film (F) and the detector (D).

3.2 X-ray scattering methods

In order to investigate the structure of the materials and to exploit x-ray scattering, multiple degrees of freedom are used to rotate the sample and the detector relative to the x-ray source. In a basic setup, two degrees of freedom are present: the angle between the incoming x-rays and the sample θ, and the incoming-outgoing x-rays angle 2θ. This setup is referred to as a two-circle diffractometer. For the characterization of thin films, a four-circle diffractometer with two additional degrees of freedom was used: the rotation around the surface normal of the thin film ϕ, and the rotation around the projection of the beam path onto the sample χ (Fig. 3.2).
Different scan types are used to collect information on the crystal structure. The most used scan to probe the film lattice is the θ-2θ scan, where the angle between source and sample (θ) is half of the angle between source and detector (2θ). The corresponding scattering vector Q of such a symmetric scan probes the direction perpendicular

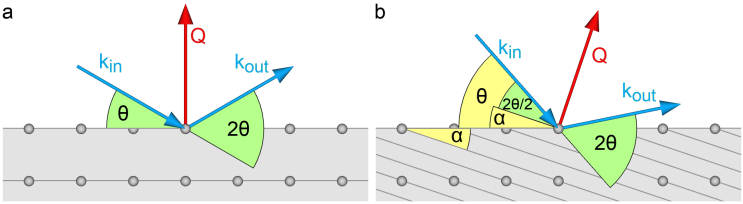

Figure 3.3: Sketch of the scattering angles for a symmetric scan, where the probed planes are parallel to the surface (a), and for an asymmetric scan in grazing exit geometry, where the probed planes are tilted by α in respect to the surface (b).

to the surface (Fig. 3.3a). In the recorded scattering intensity as a function of the scanned angle θ, peaks are observed when the Laue condition is fulfilled. The peak positions can then be used to calculate the corresponding d-spacing of the probed planes using Bragg's law (Eq. 3.4).

In addition, the lattice parameters in the surface plane (in-plane) are of interest, especially since they reveal the lattice mismatch with the substrate. In order to probe such planes, the sample must be tilted by an offset angle α so that the scattering vector Q is perpendicular to the desired set of planes. In a two-circle diffractometer, the offset can only be applied to the θ position resulting in either grazing incident geometry $\frac{2\theta}{2} - \alpha$ or grazing exit geometry $\frac{2\theta}{2} + \alpha$ (Fig. 3.3b). These asymmetric scans are limited by the condition that $0 < \theta < 2\theta$. In a four-circle diffractometer the offset can also be applied along the χ circle, where no restrictions to θ arise.

So far, the thin films were considered as perfect crystals. However, the unit cells are not perfectly ordered with respect to each other. This is called mosaicity. The small misalignment results in spread scattering vectors. The degree of mosaicity is determined by a θ scan, the so

called rocking curve, where all other motors are kept fixed.
Depending on the orientation of the thin film with respect to the diffractometer, the motion can be performed in terms of h, k and l components. By aligning two inequivalent scattering vectors Q_1 and Q_2, an orientation matrix $\mathbf{O}$ can be obtained, linking the reciprocal space to the real space orientation. With this matrix, the individual θ, 2θ, χ and ϕ values are transformed into the corresponding h,k,l values in reciprocal space, following [64]

$$\begin{pmatrix} h \\ k \\ l \end{pmatrix} = \mathbf{O}^{-1}\mathbf{\Phi}^{-1}\mathbf{X}^{-1}\mathbf{\Omega}^{-1}(\mathbf{\Theta} - 1) \begin{pmatrix} 0 \\ 2\pi/\lambda \\ 0 \end{pmatrix} , \tag{3.12}$$

where $\mathbf{\Phi}$, $\mathbf{X}$, $\mathbf{\Omega}$ and $\mathbf{\Theta}$ are the rotation matrices for ϕ, χ, θ and 2θ respectively. The wavelength λ can be calculated from the x-ray energy as

$$\lambda[\text{Å}] = \frac{12.398}{e[keV]} . \tag{3.13}$$

With the orientation matrix, the diffractometer's motors can be controlled to scan specific directions in the reciprocal space, performing so-called hkl-scans. Since the film lattice might be strained due to lattice mismatch, the substrate is frequently used as a reference system with known lattice constants. If the c-axis of the film is perpendicular to the surface, the θ-2θ scan corresponds to a l-scan. If, in addition, the a-axis lies in the scattering plane, the χ scan probes the k direction. Since the variation of k only also implies a change in the value of the Q vector, a true k-scan requires the motion of χ, θ and 2θ.
In this thesis, the c-lattice parameters were determined by performing l-scans using the Nelson-Riley fit [65]. For very thin films, where only two or fewer Bragg peaks were observed, Bragg's law was used instead.

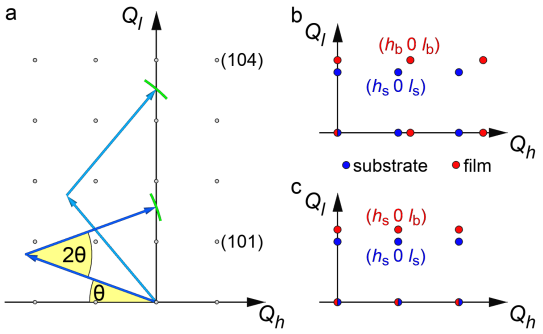

Figure 3.4: (a) Sketch of the reciprocal space mapping with a symmetric l-scan indicating the line detector's cut (green sphere) through the (h,l) plane. (b,c) Sketch of the RSM for the epitaxial relationship of the film (red) and substrate (blue), (b) when the film is relaxed assuming bulk-like properties (h_b 0 l_b) and (c) when the film is strained adapting the substrate in-plane lattice (h_s 0 l_b).

3.2.1 Reciprocal space mapping

The peak positions can not only be used to calculate the lattice parameters of a thin film, but also to investigate the epitaxial relation between the film and the substrate. A perfectly strained film adopts the latter's in-plane lattice parameters, resulting in the same h and k values for the in-plane peaks as for the substrate (h_s,k_s) (Fig. 3.4c). If the film regains the bulk-like structure, the h and k values will correspond to the bulk lattice parameters (h_b, k_b) (Fig. 3.4b). For intermediate conditions, a transition between h_s, k_s and h_b, k_b is observed.
In order to asses the strain relaxation, reciprocal space maps (RSM) are measured in the corresponding h or k region, or both. Using a point detector, only single points in the reciprocal space can be recorded at a time. However, by utilizing a line detector, for every scan position an array of 2θ values is recorded. For the structural characterization

in this thesis, a Mythen 1K line detector with 1280 channels was used. The obtained data points at one scan position resemble a curved 2D cut of the reciprocal space with different (h k l) values for each detector channel (Fig. 3.4a). For symmetric scans (Fig. 3.4a), where the a-axis lies in the scattering plane, the obtained RSM lies in the (h,l) plane. For the same sample orientation, the RSM of asymmetric scans will also be in the (h,l) plane if the offset α is applied to θ. However, if the offset is applied to χ, the RSM investigates variations of all three directions. Therefore, the correct experimental geometry has to be chosen in order to investigate the wanted reciprocal space portion.

3.2.2 X-ray reflectivity

For the determination of the film thickness, x-ray reflectivity (XRR) was used. At low θ angles, an oscillation of the intensity as a function of θ is observed, known as Kiessig fringes. These interference patterns are generated by the reflection of the x-rays from the substrate-film and film-atmosphere interfaces. They are used to determine the thickness t of the film, using the equation [66]

$$sin(\theta_m) = \frac{m \cdot \lambda}{2 \cdot t} \ . \tag{3.14}$$

Since the refractive index of the x-rays in solid matter is smaller than 1, a phase shift by π must be considered and therefore, m assumes half-integer values [63].
Similar to the Kiessig fringes, Laue fringes around the film reflections at higher θ values were also used to determine the thickness. The difference between the Q-vectors of two subsequent fringes is used to determine the thickness t based on Bragg's law and equation (3.5) with $t = 2\pi/\Delta Q$.
Since the DyBCO films are grown in a layer-by-layer mode and a good

agreement between the intended thickness and the measured one was obtained, the film thickness is stated in unit cells.

3.2.3 Resonant x-ray scattering

In RXS the x-ray energy is tuned to an absorption edge, where core electrons are promoted to empty electron levels. In general, an absorption spectrum at a specific edge comprises several peaks, corresponding to different transitions. For example, the Dy M_5 edge is composed of 3 peaks, as will be explained in more detail in section 6.2. By tuning the incoming energy to a specific peak, detailed information about the nature of the observed scattering peak can be obtained.
In scattering experiments the photon energy is usually kept constant and the peak is detected by changing the scattering vector Q. The subtraction of a background is usually necessary in order to better estimate the features of the measured peaks. The energy dependence of a scattering peak can be obtained by fixing the scattering vector and varying the energy. In this case, the background can be approximated by the linear combination of energy scans at higher or lower Q values where the peak is not present. The obtained energy profiles are a powerful tool to investigate the electronic state of the ions involved in the ordering at Q. Therefore, a combination of Q-scans and energy scans is used in RXS experiments (Fig. 3.5).

3.2.4 Instrumentation

The basic characterization of the synthesized films was performed using a four-circle Huber diffractometer with a Cu K_α source and a Mythen line detector (Fig. 3.2).
Investigations of the lattice strain were performed at the MPI beamline of the KARA Synchrotron at the Karlsruhe Institute of Technology. The beamline was operated with a four-circle diffractometer and a

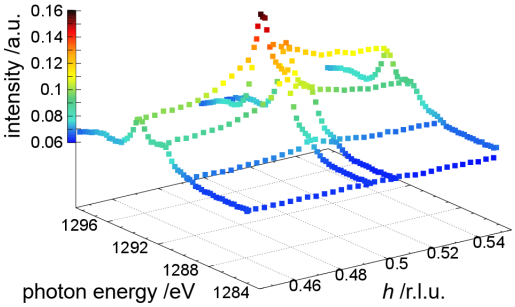

Figure 3.5: Map of the photon energy and in-plane wave vector around the (0.5 0 1.88) peak probed by x-rays tuned to the Dy M_5 edge.

Mythen line detector similar to Fig. 3.2. The $\approx$ 10 keV beam energy gave access to a large area of the reciprocal space and the high beam intensity allowed for measurements of peaks with high Q values. This is particularly advantageous when examining the strain behavior, since small changes in the lattice are only visible with a high instrument resolution and/or at high h, k, l values. Therefore, the substrate strain on the film was investigated at the (4 0 l) and (0 4 l) film reflections (l = 10 - 13) with grazing incident geometry. The twin domains were studied at the (4 0 10) peak, where no interference with substrate peaks was observed. The corresponding reciprocal space maps were obtained with hkl-mesh scans where the l value was kept constant and k and h were scanned.

Resonant x-ray measurements at the Cu L_3 and Dy M_5 edges were conducted at the UE46 PGM-1 beamline at the BESSY-II synchrotron at the Helmholtz-Zentrum Berlin. The beamline comprises two vacuum chambers with a two-circle diffractometer, a liquid Helium flow cryostat, and a photodiode detector. Since the detector is sensitive to all x-rays, the scattering can be of elastic and inelastic nature and it is therefore referred to as resonant x-ray scattering (RXS).

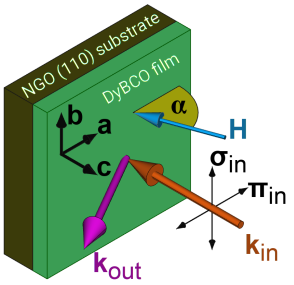

Figure 3.6: Sketch of the scattering geometry for the RXS experiments in the magnetic field chamber.

The incident x-ray beam can be polarized either perpendicular (σ) or parallel (π) to the scattering plane (Fig. 3.6). In addition, one chamber is equipped with a magnet, which allows the application of magnetic fields of up to 6 T. The magnet interferes with the accessible θ and 2θ values, limiting the experimental geometry.
The setup further allows for measuring XAS in total electron yield mode by grounding the sample with silver paint. By using left- and right-handed circular polarized x-rays, x-ray magnetic circular dichroism (XMCD) can be measured. The difference between the absorption spectra measured with left and right circular polarized x-rays is known as XMCD. The magnitude of the dichroism is proportional to the magnetic moment of the ions, thus XMCD facilitates the investigation of the magnetic configuration.

Chapter 4

Growth and characterization of $DyBa_2Cu_3O_{7-\delta}$ thin films

This chapter focuses on the growth of DyBCO thin films. The general aspects of ALL-MBE growth as discussed in chapter 2 are applied to grow DyBCO thin films. In section 4.1, we present the optimization of growth routine and the *in-situ* feedback to avoid defect formation. Furthermore, we discuss the characterization of grown films using XRD, AFM, STEM and transport measurements in section 4.2. Finally, the possibilities to tune thin films by oxygen doping and the transfer of the growth procedure to other rare-earth elements are shown. The synthesis and characterization have been published in [67].

4.1 DyBCO growth

In the following, we present the growth of DyBCO thin films and the optimization towards high quality films. Since DyBCO has three cations, the growth involves a complex interplay between them with

numerous possible side products. Therefore, the precise control of the elements as well as the deposition in the correct stoichiometry are essential.

4.1.1 QCM calibration

In contrast to simple perovskites ABO_3, where the stoichiometry adjustments can be accomplished by changing one element while keeping the second one constant, DyBCO has an interplay of three elements which adds another parameter.
Therefore, the initial calibration with the QCM is crucial and particular attention was paid to further optimize the precision. During the deposition of an element, the shift of the quartz crystal oscillation frequency as a function of time is used to calibrate the flux (Sec. 2.3.1). A good linear approximation of the QCM frequency is obtained if the initial 40 s are ignored, where the shutter transient effect (STE) causes an initial higher flux (Fig. 2.4). However, the additional material arising from the STE must be considered, too. Therefore, the initial 40 s are included in the linear approximation, which results in an increase of the determined flux by up to 10 %. Since the STE depends on the duration of how long the shutter was closed, a growth-based calibration cycle is used where the open and closed shutter times are similar to the growth sequence. As a consequence, the obtained rate represents the most part of the growth, except for the initial layers, which exhibit a slightly higher rate, since the shutter is closed for a long time during the substrate heating.
The second modification is the usage of a heating controlled QCM equipped with a thermocouple. During calibration, the temperature change of the quartz (ΔT_{QCM}) can be reduced by adjusting the coolant flow. Due to the construction limitation that no thermocouple can be

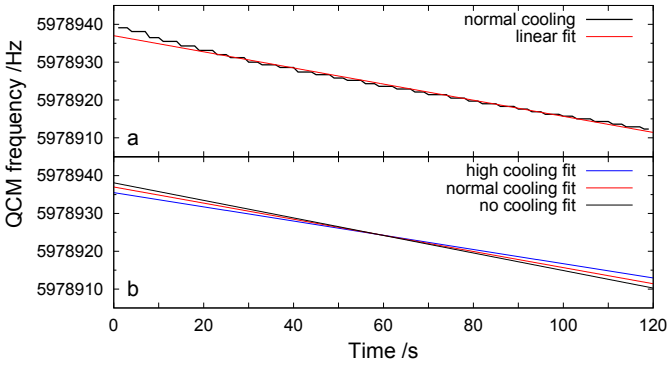

Figure 4.1: QCM calibration curves. (a) Calibration curve for normal cooling with $\Delta T \approx \pm$ 0 K and corresponding linear approximation. (b) Comparison of the linear approximation for the same effusion cell without QCM cooling ($\Delta T \approx$ +0.6 K, black line), with normal QCM cooling (red line) and with high QCM cooling ($\Delta T \approx$ -0.2 K, blue line).

placed on the quartz and the resulting offset in the measured temperature, the coolant flow should remain constant during the calibration to avoid a thermal drift. The influence of the quartz temperature on the calibration is shown in Fig. 4.1. For each coolant flow, the change of frequency over time matches well to a linear approximation, indicating a stable flux. However, the QCM temperature changes during the deposition causing a temperature induced shift of the QCM frequency. Thus, the obtained slope and the determined flux differ by +10 % for $\Delta T_{QCM} \approx$ +0.6 K and by -10 % for $\Delta T_{QCM} \approx$ -0.2 K compared to the calibration at a constant temperature ($\Delta T_{QCM} \approx$ 0 K).
Furthermore, the QCM's coolant flow needs to be adjusted to the cell temperature to obtain a constant QCM temperature. Since the coolant

flow is controlled by a hand valve and the stable QCM temperature is confirmed after two or more calibration cycles, the calibration cycles for one element are completed before the calibration of the next element is started. In conclusion, the error of calibration can be reduced by using a growth based calibration cycle, by keeping the QCM temperature almost constant, and by calibrating one element after another.

The QCM's heat control also allows for monitoring the flux during film growth without overheating the quartz. The QCM remains in the chamber at a position where it does not cast a shadow onto the substrate and where it is still exposed to the element beam. The heat radiation from the substrate holder slowly increases the QCM temperature. In addition, anomalous heating arises from the element beams and heat radiation from the Knudsen cells. Therefore, a constant temperature can not be obtained, which inhibits an *in-situ* calibration. Nevertheless, the determined frequency shifts can be used to calculate the ratio between the different element fluxes. By comparing the ratio of the n-th unit cell with the ratio of the previous layers, required adjustments to the stoichiometry can be identified.

In Fig. 4.2, the determined frequency slope as well as the QCM temperature are shown for the growth of a 40 u.c. thick film. The spikes in the slope and the simultaneous drop in the temperature are related to the refilling of the ozone unit's liquid nitrogen tanks and a consequential cooling of the QCM's coolant supply. These spikes demonstrate the temperature sensitivity of the QCM and the limitation of the heat control. Therefore, *in-situ* RHEED is the primary feedback system and the QCM serves as a second system to support it, especially if a sudden high off-stoichiometry different from the previous layers is observed.

The calibration of the element flux after the growth enabled us to evaluate the assumed constant flux and to confirm *in-situ* stoichiometry adjustments. While the flux of Cu and Dy deviated only slightly, the

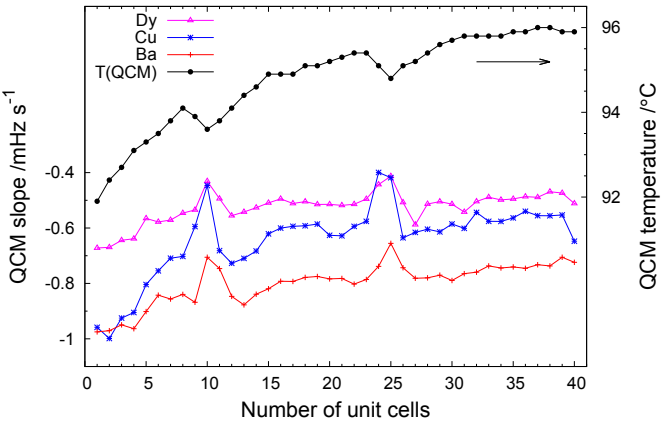

Figure 4.2: *In-situ* QCM monitoring during the growth of 40 u.c. DyBCO. The observed spikes arise from the N_2 refill of the ozone unit.

Ba flux was often reduced, sometimes up to -30 % compared to the initial calibration. This is related to the formation of oxides in the crucible and the consequential reduction of the surface area. Therefore, an increase of the Ba shutter time during the growth can be anticipated, while Cu and Dy should be limited to small adjustments.

4.1.2 *In-situ* RHEED

During film growth, RHEED is the primary feedback system to identify the formation of the desired 123 structure as well as defects. In comparison to co-deposition growth, the layer-by-layer technique facilitates monitoring of changes related to the deposition of a single element. By closing shutters early, or by adding additional opening time, the stoichiometry can be adjusted during growth. By enhancing certain RHEED patterns through off-stoichiometric growth, the corre-

sponding phases can be identified by the required stoichiometry and by *ex-situ* characterization like x-ray diffraction analysis (Sec. 4.2.1). Due to the DyBCO structure, the deposition sequence of Ba-Cu-Dy-Cu-Ba-Cu atomic layers was chosen as the starting point. However, the deposition of Cu after Ba was frequently accompanied by the formation of a characteristic RHEED pattern associated with $BaCu_xO_y$ defects. Therefore, the Ba and Cu deposition were separated by a Dy layer, and a 2Ba-Dy-3Cu sequence similar to Locquet *et al.* [68] was adapted. Thus, a sequential growth mode was obtained, where changes to the RHEED pattern can still be related to only one open shutter.

The interpretation of the RHEED evolution and appearance of characteristic patterns is a complex interplay and sometimes not unambiguous. Therefore, we investigated indicators for the completion of the individual layers, as well as indicators for common defects. By monitoring the intensity of different RHEED patterns in selected areas simultaneously and by detecting changes in the flux with the QCM, the stoichiometry was controlled during growth.

Fig. 4.3 shows an example of a set of monitored areas during growth. During the Ba deposition, the intensity of area 1 and 5 decreased until a minimum was observed, assumingly when BaO started to form and the corresponding pattern's intensity increased. A slight excess of Cu resulted in a pattern with a spot in area 7. The additional Cu formed during the next Ba deposition $BaCu_xO_y$ which was tracked in area 3 and 6. In the beginning of the growth, particularly during the deposition of Dy, an intermediate phase formed that was detected in area 2 and 8, and that could be dissolved by adding more Cu during the next layers. However, an early suppression with more Cu frequently led to excess Cu and consequently $BaCu_xO_y$. Finally, a weak intensity in spot 4 indicated the formation of DyBCO, while a strong intensity indicated the formation of Dy_2O_3. Since (110) oriented Dy_2O_3 matches

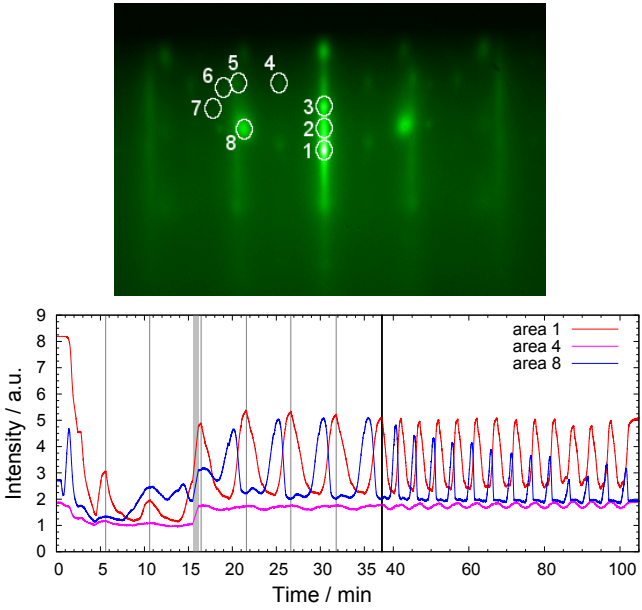

Figure 4.3: (top) Monitored RHEED diffraction spots and (bottom) corresponding intensity oscillation for selected areas during growth. The completion of the first seven unit cells is indicated by vertical lines. After the third unit cell the RHEED current was increased (gray zone).

well to the DyBCO lattice, a distinct RHEED pattern did not show up until a large amount of excess Dy was deposited.

Upon opening the shutter to deposit material, the RHEED intensity initially decreased slightly, arising from the diffuse scattering off the added material. This initial decrease is always present and limits the feedback based on the intensity evolution, particularly when adding just a small amount of material. Therefore, the deposition times for Ba and Cu were extended beyond stoichiometric composition and the

shutters closed manually with RHEED feedback corresponding to the completion of the layer. For Dy the stoichiometry was kept at 1.0 and only changed if Dy_2O_3 defects became dominant or if the QCM indicated a change of the flux.

The first layers are crucial for film growth, because growth seeds for the following layers are formed. If the stoichiometry deviates far from the 123 composition, defects will form and propagate. In the sequential growth mode, the stoichiometric element ratio is only obtained after the completion of a full unit cell, making it more susceptible to defect formation. Since, in the beginning, no coherent growth seeds are present, characteristic RHEED patterns are not observed and stoichiometry adjustments are not possible. Therefore, the initial RHEED intensity decreases quickly (Fig. 4.3) and the formed seeds primarily depend on the initial calibration, emphasizing its crucial role for the film quality.

Despite the initial limitation of RHEED feedback, the deposition in the stoichiometric 1:2:3 ratio leads to the formation of $BaCu_xO_y$ defects, which are visible beyond the decreasing overall intensity. While minor defects can be dissolved, such large defects, which give rise to a strong RHEED pattern, can not be dissolved in the following layers. Since $BaCu_xO_y$ occurs after an excess of Cu, the ratio for the first layer is reduced to 1:2:2. STEM imaging reveals a BaO-CuO_2-Dy-CuO_2-BaO-CuO stacking at the interface (Fig. 4.8), which explains the suppression of the defect for the Cu-deficient initial layer.

After the fourth unit cell the characteristic RHEED patterns emerge and stoichiometry adjustments can be made. The respective pattern after Ba, Dy and Cu deposition repeats itself for every additional layer (Fig. 4.4a-c) and an almost undamped RHEED intensity oscillation is obtained. A slight damping is observed after unit cell 6 -10, indicating the transition to an island growth mode.

The RHEED patterns and the intensity osciallation are observed for all

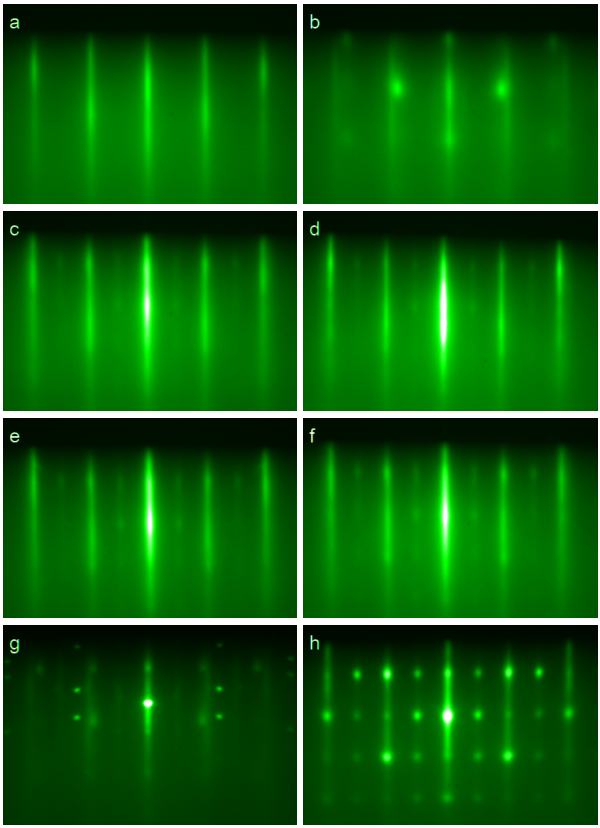

Figure 4.4: Characteristic RHEED patterns are observed during growth after the completion of (a) Ba, (b) Dy and (c) Cu on STO (100), as well as for the formation of (g) $BaCu_xO_y$ and (h) Dy_2O_3 defects. A representative RHEED pattern at the end of the growth is shown for 20 u.c. DyBCO on (d) NGO (110), (e) LSAT (100) and (f) STO (100).

used substrates, confirming the surface sensitivity of RHEED. Through careful stoichiometry adjustments, films without defect patterns are obtained (Fig. 4.4d-f). Between the substrate streaks a second pattern is observed with a spot distribution typical for a 3D growth. It could be related to the presence of Dy_2O_3 defects at the surface, which is beyond the detection of XRD and therefore can not be confirmed. Since the pattern also matches with the DyBCO main streaks, it can be related to a surface reconstruction, for example by arrangement of oxygen atoms in the ortho-II order causing a doubling of the *a*-axis. For DyBCO thin films, a decreased oxygen content at the surface was determined by angle-resolved photoemission spectroscopy [69]. However, in the presence of ozone the formation of an oxygen-deficient surface seems unlikely. In the final RHEED pattern of films thicker than 20 u.c. frequently weak defect spots are observed, which can be related to the accumulation of minor stoichiometry offsets. Since the *in-situ* feedback is limited, the grown films are extensively characterized after growth.

4.1.3 Oxygen-doping of DyBCO thin films

In addition to the growth of fully oxidized thin films with a high superconducting transition (T_c), oxygen-doping was also investigated. By annealing the films in the MBE at ≈ 650 °C in vacuum, a complete suppression of the superconducting transition is obtained. However, by annealing in a low ozone background pressure ($p(O_3) \approx 3-5\times10^{-9}$ torr), a reduced T_c is achieved. The original high T_c can be recovered by subsequent annealing in high ozone pressure, making it a reversible process. Therefore, the reduced T_c can be related to a different oxygen doping and not to a decomposition. Due to the low background pressure and fluctuation of the ozone pressure, which was within the

noise level of the RGA, doping towards a precise T_c was only possible within a $\pm$ 5 K range. The annealing conditions (time and pressure) depend on the substrate and the film thickness.

4.2 Structure characterization

Film characterization involves multiple techniques to investigate the overall structure (XRD), the surface (AFM), the stacking order (STEM) and the superconducting transition. The combined results of these characterizations provided a measure of the film quality and were used to further optimize the growth.

4.2.1 X-ray diffraction analysis

X-ray diffraction (XRD) provides information about the average composition of the film. It was used as the standard technique to identify the formed phases and to determine the film thickness as described in section 3.2.2. Symmetric out-of-plane scans were measured with a four-circle Huber diffractometer and Cu-$K_{\alpha 1}$ radiation. Using the Bragg equation, d-spacing analysis was applied to identify matching phases to the observed reflections. The high crystalline quality of the films was confirmed by the presence of pronounced peaks matching c-axis oriented DyBCO.

The formation of defects was enhanced by off-stoichiometric growth. Thereby, strong peaks corresponding to the defect were observed in the XRD pattern, which made an identification possible. During film growth, several defects can form, displaying multiple orientations with respect to the substrate surface and possibly even exhibiting epitaxial strain. An unambiguous identification therefore requires more scans, especially with in-plane components. However, the precise composition

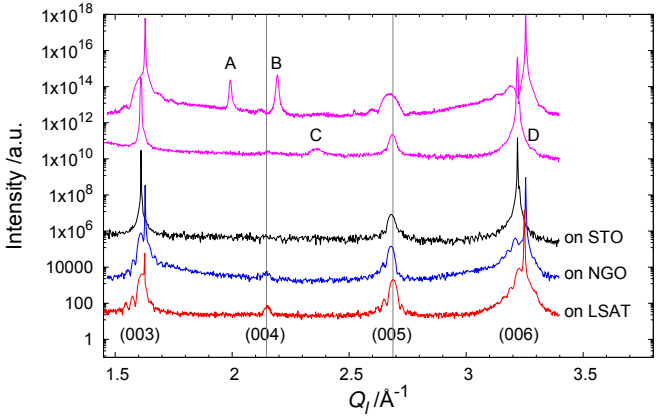

Figure 4.5: XRD of films contain the common defects (A-D, as discussed in the text) and the optimized DyBCO films without defects on LSAT (100), NGO (110) and STO (100). The DyBCO peaks are indexed at the bottom with a guide to the eye for the (004) and (005) position. The (003) and (006) DyBCO peaks overlap with the (pseudo-) cubic (001) and (002) substrate reflection.

of the defect is not significant for the growth optimization, as long as the defect formation can be suppressed by *in-situ* adjustments.
For films with an excess of Dy, the additional peak ($Q_l \approx 2.36$ Å^{-1}, d = 2.66 Å) (Fig. 4.5 defect C) matches with (001) oriented Dy_2O_3 (d = 10.68 Å = 4 · 2.67 Å) [70]. In addition, Dy_2O_3 with an in-plane (110) orientation also provides a good match with the substrate lattice, being visible in RHEED only if large defects formed (Fig. 4.4h).
For Ba-rich films, (110) oriented BaO (d = 7.83 Å = 4 · 1.96 Å) [71] can be assigned to the peak at $Q_l \approx 3.29$ Å^{-1} (d = 1.91 Å) (Fig. 4.5 defect D). This peak overlaps with the trace of the (pseudo-) cubic (002) substrate reflection and Laue fringes from the (006) film peak, making it only visible in a high concentration. In films with a charac-

teristic $BaCu_xO_y$ RHEED pattern (Fig. 4.4g), a peak at $Q_l \approx 1.99$ Å^{-1} (d = 3.16 Å) is present in the diffraction pattern (Fig. 4.5 defect A). It can be matched with strained (111)-oriented $BaCu_2O_2$ (d = 12.87 Å = 4 · 3.22 Å) [72] or strained (110)-oriented $BaCuO_2$ (d = 25.86 Å = 8 · 3.23 Å) [73]. Therefore, the impurity is referred to as $BaCu_xO_y$. The formation of Cu^{1+} compounds is observed in low oxygen pressure [74], which makes a Cu^{2+} in ozone more likely.

Another impurity is observed with a d-spacing of 2.87 Å ($Q_l \approx 2.19$ Å^{-1}) (Fig. 4.5 defect B) and frequently appears together with $BaCu_xO_y$ defects. It can be matched with (100) $BaCu_2O_2$ (d = 5.72 Å = 2 · 2.86 Å) [72] or Dy-containing impurities like (010) oriented Dy_2BaCuO_5 [75] or (100) oriented $DyCu_2O_4$ [76]. *In-situ* RHEED does not show a particular diffraction pattern for this impurity, making a suppression difficult.

With the optimized growth feedback, phase pure DyBCO films with the *c*-axis out-of-plane and without additional impurity peaks were obtained for thicknesses up to 40 u.c. on different substrates (Fig. 4.5). The high crystalline quality was confirmed by the presence of Laue fringes around strong film peaks. In thicker films the longer growth times increased the chance of the accumulation of tiny off-stoichiometry and the formation of small defects.

The position of the DyBCO reflections and the determined *c*-lattice parameters are related to the oxygen content. This is discussed within the scope of the superconducting properties in section 4.3.1. For selected films, the formation of orthorhombic twin domains was investigated using synchrotron radiation, which is discussed in Chapter 5.

In addition to the impurity identification, low angle x-ray reflection was used to determine the film thickness. While for the first films grown, the thickness deviated up to 50 % from the intended thickness, in the optimized growth the desired thickness is achieved. Therefore,

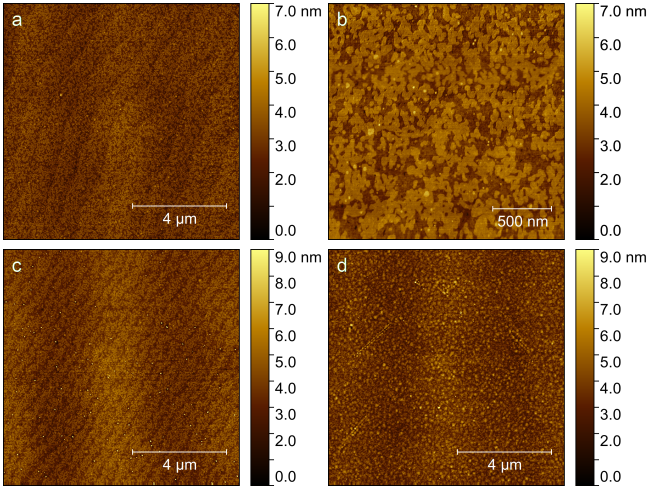

Figure 4.6: AFM surface imaging of 7 u.c. DyBCO films. Films on (a,b) etched STO (001) and (c) not-etched STO show traces of the substrate edges. (d) In films on LSAT islands dominate the surface.

the period of the RHEED oscillation corresponds to one unit cell and a layer-by-layer growth mode is obtained.

4.2.2 Atomic Force Microscopy imaging

The surface of the films was investigated by atomic force microscopy (AFM) using a multinote AFM by Veeco and a Dimension Icon AFM by Bruker. Prior to growth, the substrates were rinsed with acetone and isopropanol and baked at the growth condition for $\approx$ 15 min in the MBE. Therefore, the substrates are expected to have a mixed termination and smeared out terraces.

For very thin films on STO (100), the substrates were treated with buffered HF acid as described by [77] to obtain a TiO_2 termination and atomic terraces. In 7 u.c. DyBCO films on etched STO, traces of the

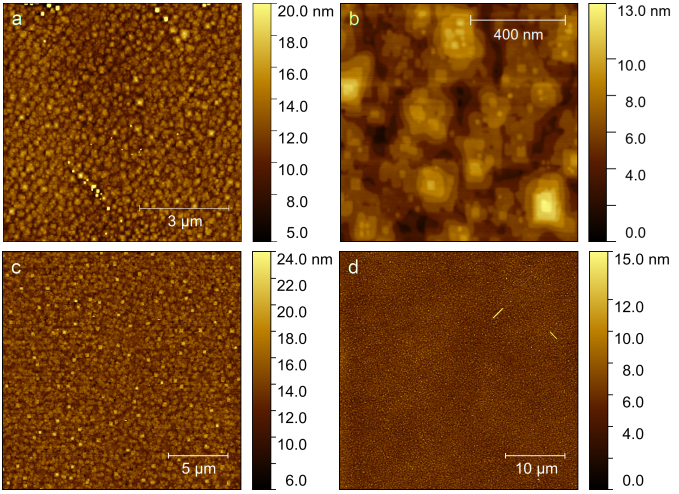

Figure 4.7: AFM surface imaging of 40 u.c. DyBCO on (a,b) LSAT, (c) STO and (d) NGO.

terraces are still visible (Fig. 4.6a). The close-up shows that instead of completing the first layer, a second layer has already formed, indicating an island growth type (Fig. 4.6b). The sharp terrace edges from the substrate vanish between the islands. Strikingly, traces of the substrate are also observed on not-etched substrates as shown in Fig. 4.6c. The alignment of the DyBCO layers indicates either preferred nucleation sites for the new layer or a favored growth direction, matching the substrate terraces or both. The different spacing between the DyBCO layers on the etched and not-etched substrate can be related to the substrate miscut, which was not recorded.

The formation of islands is more striking for films grown on LSAT. In 7 u.c. thick films, the surface is covered by islands with up to four levels (Fig. 4.6d). The height of the island levels is $\approx$ 1.2 nm and corresponds to the *c*-axis of DyBCO. By increasing the film thickness,

the islands also dominate the surface of films on STO. Therefore, the use of etched substrates was limited to a few very thin films.
In thicker films, the islands have a rectangular shape and step height matching to the *c*-axis length of DyBCO. For 40 u.c. on LSAT (Fig. 4.7b) screw islands similar to PLD and sputtering growth are observed [78, 79].
The large scale scans of the thicker films reveal a few surface defects which are identified as white blocks or rods (Fig. 4.7a, c, d) and are associated with the defects identified by XRD. The majority of the film consists of growth islands whose height increases with increasing film thickness.

4.2.3 Scanning Transmission Electron Microscopy imaging

Information of nanoscopic defects were obtained by STEM in collaboration with the Stuttgart Center for Electron Microscopy. Through cross-section imaging, the substrate-film interface and stacking faults were investigated. In z-contrast STEM imaging, heavier atoms appear brighter than lighter ones, allowing for the distinction of different atoms based on their atomic mass. Due to the elaborate preparation of cross sections by milling and the consequent destruction of the sample, only a few films were characterized by STEM.
Although the initial decrease of the RHEED intensity during growth indicated high disorder, the observed substrate-film interfaces on all substrates are sharp (Fig. 4.8c, 4.10). This reveals, that the mobility of the atoms under the growth condition is high enough to rearrange the deposited 2Ba-Dy-3Cu sequence into the DyBCO structure.
The interfaces consist primarily of a BaO-CuO_2-Dy-CuO_2-BaO-CuO stacking, therefore, the first CuO-chain layer is missing. This is consis-

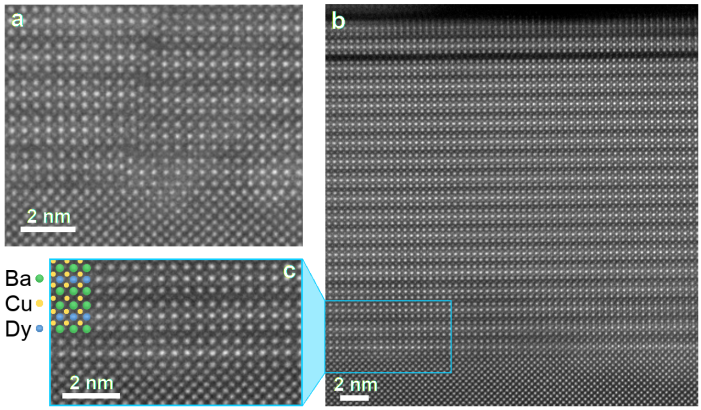

Figure 4.8: STEM image of of 20 u.c. DyBCO grown on LSAT. (a) At the substrate-film interface anti-phase boundary can arise from different stacking orders. A sketch of the DyBCO structure is included in (c).

tent with the growth sequence, where only two layers Cu are deposited for the first unit cell. Nevertheless, due to the limited RHEED feedback during the initial layers, also CuO-BaO-CuO_2-Dy-CuO_2-BaO-CuO stacking and consequently anti-phase boundaries similar to PLD grown films can be observed in some films (Fig. 4.8a) [80]. Similar to PLD grown films with a 122 YBCO target for the first unit cell [81], the flexible stoichiometry of MBE growth allows the reduction of the formation of anti-phase boundaries.

Despite the *in-situ* growth adjustments, defects are observed inside the films. For example, Dy-rich films form Dy_2O_3 defects with a (110) in-plane orientation, which are well matched to the DyBCO lattice. Therefore, inclusions of Dy_2O_3 are easily formed and can also be overgrown by DyBCO (Fig. 4.9b). Depending on the degree of off-stoichiometry, the additional Dy can form double Dy layers inside

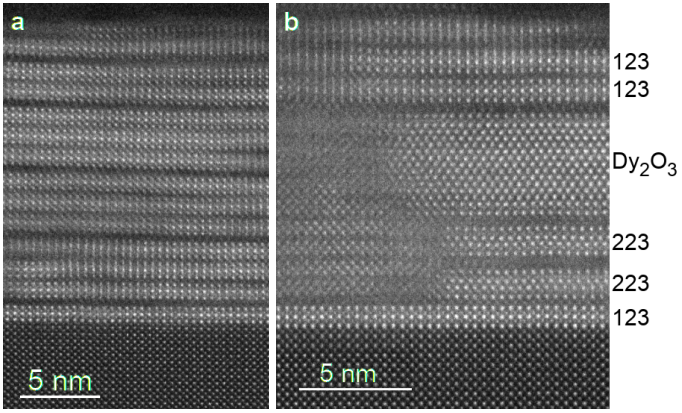

Figure 4.9: STEM images of films before growth optimization containing (a) a high concentration of 124 stacking faults and (b) Dy_2O_3 defects forming a block or an additional layer inside the 123 structure ("223") in Dy-rich films.

the DyBCO structure or large defect areas.

Another common defect is the inclusion of an additional CuO-plane resulting in $DyBa_2Cu_4O_8$ (124). These 124 stacking faults can be identified by an extended dark space between two bright BaO-BaO layers. The additional CuO layer results in a shift of the next blocks by half a unit cell along the *b*-axis [82]. Depending on the defect orientation, the shift of the following 123 blocks can be observed in the cross section. While these defects were distributed throughout the first grown films (4.9a), in optimized films they are only observed in the topmost layers (Fig. 4.8b, 4.10). Even in the optimized growth, tiny amounts of additional material, such as Cu, float on top of the structure and only form defects when a critical density is obtained.

The defect density in the optimized films is very low. They possess a sharp substrate-film interface and only a few 124 stacking faults in the

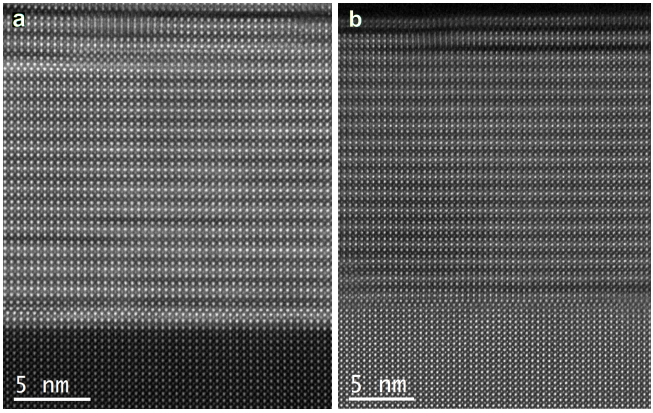

Figure 4.10: STEM image of optimized 20 u.c. films on (a) STO and (b) NGO revealing a low defect density and showing 124 stacking faults only in the topmost layers.

topmost layers. Therefore, the optimized film growth provides access to films with a low defect density.

4.3 Superconducting properties

After confirming the phase formation and the minimization of defects, the superconducting properties were investigated using a mutual inductance setup (MI), which probes the Meissner effect. For selected films, the resistance was measured in van der Pauw geometry (sec. 4.3.2).

4.3.1 Mutual Inductance

In mutual inductance measurements, a film is placed between a drive coil, where an *ac* current generates a magnetic field, and a pickup coil, where the induced voltage is measured [83, 84]. The mutual inductance

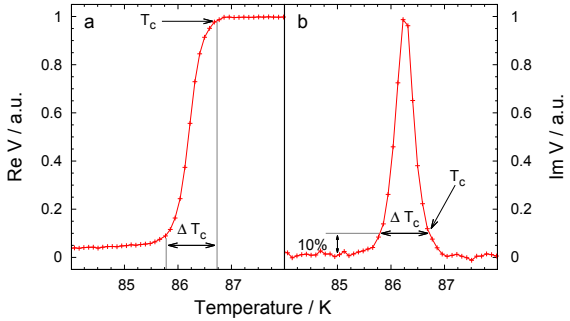

Figure 4.11: Mutual inductance measurement of a 20 u.c. film on LSAT highlighting the superconducting transition T_c and the transition width ΔT_c. The real and imaginary signals were normalized to 1.

can be written as [85]:

$$M = ReV + i \cdot ImV \ . \tag{4.1}$$

When cooled to the superconducting state, the magnetic field is expelled from the sample (Meissner-Ochsenfeld effect). The superconducting transition is characterized by a drop in the real part of the inductance due to induced shielding currents in the film and a peak in the imaginary part, which is proportional to the derivative of the magnetic flux. Since the coils are smaller than the standard film dimensions (10x10 mm^2), only a tiny fraction of the field can leak around the edges of the sample and hence, the picked up signal below T_c is almost zero.

In this work, T_c is defined as the onset of the superconducting transition and the respective transition width based on the imaginary part when the signal crossed 10 % of the maximal peak intensity (Fig. 4.11), which is equivalent to a 5 % - 95 % criterion in the real part. The temperature sensor is located at the base of the MI setup, giving rise to a temperature offset. Therefore, the average of the cooling and the

heating cycle is used to determine T_c.

In MI measurements, a narrow transition width indicates a homogeneous film, while a broad transition indicates a less uniform film. If domains with different T_c are present in the film, which differ more than the transition width, two peaks can be observed in the imaginary signal. However, the shielding of superconducting layers (high T_c) prevents the detection of superconducting transitions at lower temperatures (low T_c), such as from layers close to the interface.

All good MBE-grown films above 20 u.c. thickness have a superconducting transition above 80 K and a narrow transition (ΔT < 4 K). Due to the stoichiometric degree of freedom in MBE, especially the different element flux from one growth to another, only approximately 25-50 % of the grown films have a low defect density and a corresponding high T_c.

The superconducting transition depends on the oxygen content, which is affected by the growth pressure. Films grown by PLD and sputtering in oxygen require an additional annealing step in high oxygen pressure to obtain a high T_c [86–89]. In contrast, films grown by ozone MBE are cooled down at growth pressure and achieve a high T_c. No additional annealing step is required, confirming the high oxidation power of ozone compared to molecular oxygen.

Despite the utilization of ozone, very thin films exhibit a reduced T_c (Fig. 4.12). While 10 u.c. thick films on STO and LSAT exhibit a T_c above 70 K with a narrow transition, thinner films have a decreased T_c and a broader transition. Films below 4 u.c. were not investigated, since the RHEED pattern did not indicate the formation of DyBCO.

The suppressed T_c can be assigned to many reasons. First, it can be attributed to cation intermixing with the substrate and thereby introducing defects into the interface layers. In addition, STEM (Fig. 4.8) shows that at the interface the first CuO chain layer is missing, leaving the superconducting CuO_2 planes underdoped. Recent ARPES

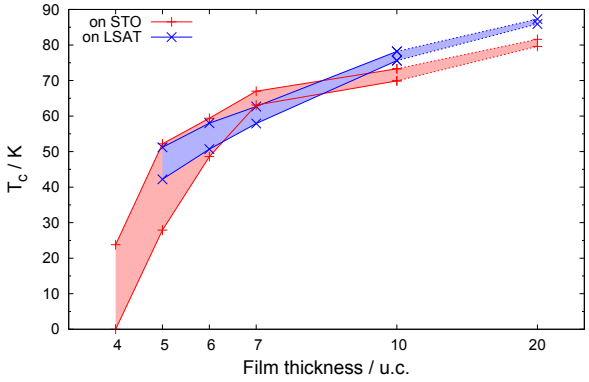

Figure 4.12: T_c versus film thickness of films on LSAT (blue) and STO (red). The shaded area represents the transition width and is a guide to the eye.

investigations of a DyBCO film revealed that despite a high T_c determined by MI, the surface shows a lower doping than the inner layers [69]. This picture of different superconducting layers inside the films is supported by measurements of the superfluid density [90], where four non-superconducting layers were determined. These could be located at the film interface or also in the topmost layers of the film.

The lattice match with the substrate also has to be considered. LSAT and STO have a cubic structure causing a deformation of the DyBCO structure. Two kinds of deformation can be induced: an elastic deformation, where the unit cell volume is preserved and the compression (stretching) of the *a*- and *b*-axes result in a stretching (compression) of the the *c*-axis, respectively, and an inelastic deformation, where atom positions are shifted.

By investigating the *c*-lattice parameter as a function of the film thickness, the origin of the deformation can be investigated. Due to the small film thickness, the DyBCO peaks in the XRD are wide and have

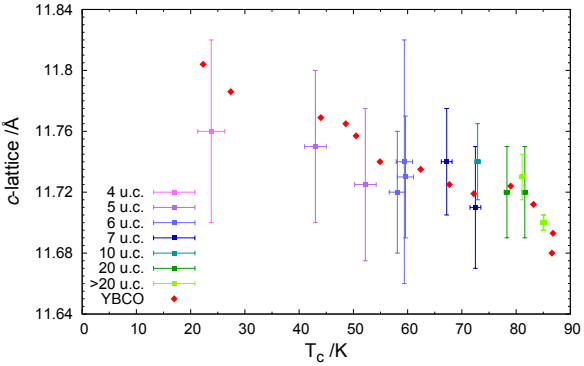

Figure 4.13: T_c vs c-lattice for films grown on STO with various thicknesses and in comparison with 30 nm YBCO on STO with various oxygen-doping levels (from [91]).

a low intensity. Therefore, the c-lattice determination is limited to the intense (005) and (007) reflection, resulting in a high uncertainty. Although the elastic deformation predicts a decrease of the c-lattice for films grown with tensile lattice strain, the contrary is observed for films on STO (Fig. 4.13). Similar observations were made for NdBCO films, where the c-lattice expansion in very thin films was assigned to the different ability to incorporate oxygen [92]. The increase of the c-lattice with decreasing oxygen content is known for YBCO single crystals (Fig. 1.2b) [17]. Comparing the determined c-lattice evolution of the DyBCO films on STO with oxygen deficient YBCO films on STO [91], the tendency of both series match. Therefore, the reduced T_c can be associated with the formation of oxygen defects.

Since STO causes a rather large lattice mismatch, the inelastic deformation is not surprising. Therefore, DyBCO films on LSAT, which causes tensile (compressive) strain along the a- (b-)axis of DyBCO, are investigated. Also for these films, an increase of the c-lattice with de-

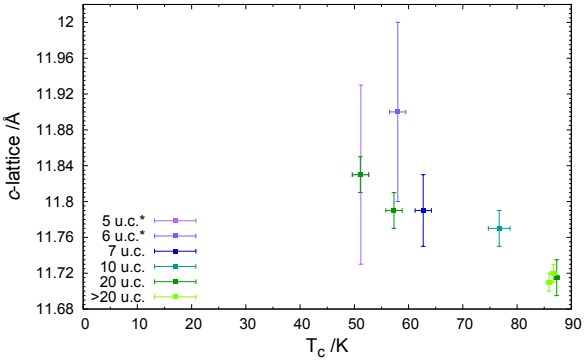

Figure 4.14: T_c vs c-lattice for films grown on LSAT with various thicknesses and in comparison with oxygen-reduced 20 u.c. DyBCO films. For the 5 u.c. and 6 u.c. thick film the c-lattice was determined only by the (005) reflection.

creasing film thickness is observed. The obtained c-lattice parameters match well with the trend observed of 20 u.c. thick oxygen-deficient DyBCO films (Fig. 4.14). Hence, also for films with a small lattice mismatch, the inelastic deformation dominates.

The reduced T_c is also linked to the lattice match with the square surface of the substrate. In very thin films, the corresponding tetragonal DyBCO phase is stabilized and the incorporation of oxygen into the chain layers is energetically disadvantageous [92]. Above the critical thickness, chain layers are stable, orthorhombicity is induced (sec. 5.2) and an increased T_c is obtained.

The investigated ultra thin films (< 7 u.c.) degraded over time, even when stored in Ar atmosphere. The XRD and MI measurements were therefore performed within a week to attribute the c-lattice to the film thickness without the additional degradation. By annealing the films in ozone atmosphere, the original T_c can be recovered. Thus,

the degradation is assigned to the loss of oxygen and not due to decomposition.

The reduction of the oxygen content over time can be induced by the epitaxial strain. The oxidation power from ozone favors a high oxygen content and the superconducting orthorhombic phase. Therefore, during growth conditions a high oxygen content is generated in the film. When the film is stored in inert atmosphere, the lattice mismatch between the film and the substrate can dominate and the surplus oxygen can slowly diffuse out of the film obtaining the energetically favored non-superconducting tetragonal DyBCO phase. Above 10 u.c. thickness the DyBCO film can accommodate the high oxygen content by forming orthorhombic domains (sec. 5.2) and T_c is stable.

In films above 20 u.c. thickness, the transition temperature increases only slightly and values around 86 K are obtained for the best films (Tab. 4.1). The only exception are films on STO, whose T_c is about 2-4 K lower than for films on LSAT and NGO. The origin is ascribed to the twinning mechanism on the different substrates, which is discussed in detail in chapter 5. While films grown on LSAT and NGO form twin domains along the [110]/[1$\bar{1}$0] direction above 10 u.c. thickness, films on STO have an intermediate step with twinning along [100]/[010] between approximately 10 and 40 u.c. thickness. This step causes additional disorder, which can be responsible for the lower T_c. Finally, for very thick films on STO (60 u.c.), a T_c of 85 K similar to films on LSAT and NGO is obtained. The highest T_c is still lower than the 93 K reported for DyBCO single crystals [93] and can be assigned to the distorted structure of the films induced by the epitaxial strain as well as slight offsets in the stoichiometry.

In films with reduced T_c, a mixed state between the orthorhombic high T_c phase and the tetragonal non-superconducting phase is formed (sec. 5.5). While their T_c is stable upon storage, synchrotron based x-ray experiments result in a decrease of T_c. This suggests that x-ray

illumination initiates the transition towards the non-superconducting tetragonal phase. The transition from the fully oxidized orthorhombic phase towards the underdoped tetragonal phase is further discussed in section 5.5.

4.3.2 Transport measurements

For selected films, four-probe resistivity measurements in van der Pauw geometry were conducted. With the assumption of a contact area much smaller than the sample surface, a homogeneous film thickness and no isolated holes in the sample, the sheet resistance of a two dimensional sample with an arbitrary sample shape can be calculated [94]. By measuring the resistance R_1, where the current is applied along one edge of the sample and the voltage is measured along the parallel edge, and by measuring the resistance R_2, where the current and voltage are along the second set of parallel edges (Fig. 4.15a), the sheet resistance can be calculated with the following equation:

$$R = \frac{\pi}{ln2} \cdot \frac{(R_1 + R_2)}{2} \cdot f(R_1/R_2) \ . \tag{4.2}$$

$f(R_1/R_2)$ is a correction factor for the sample geometry and can be obtained from published tables [95] or by solving: [94]

$$\frac{R_1 - R_2}{R_1 + R_2} = f(R_1/R_2) \cdot arccosh\left(\frac{exp(ln2/f(R_1/R_2))}{2}\right) \ . \tag{4.3}$$

Based on the sheet resistance and the sample thickness t, the resistivity ρ can be obtained:

$$\begin{aligned} \rho_s &= R_s \cdot \frac{A}{l} = R_s \cdot t \\ &= \frac{\pi \cdot t}{ln2} \cdot \frac{(R_1 + R_2)}{2} \cdot f(R_1/R_2) \ . \end{aligned} \tag{4.4}$$

To ensure accurate results, four Pt contacts were sputtered onto the corners of the selected films. The measurements were carried out in a

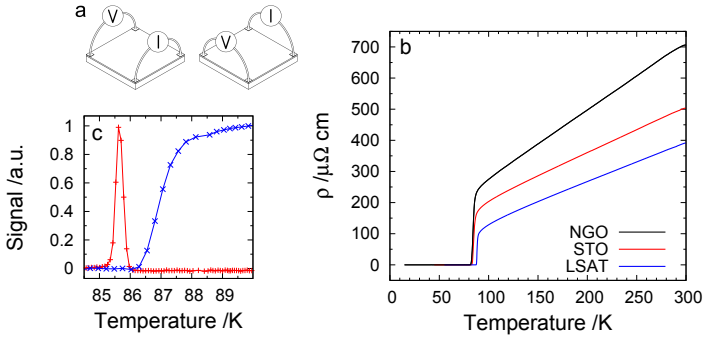

Figure 4.15: (a) Sketch of the contact orientation for the measurements in van der Pauw geometry. (b) Representative resistivity curves for 20 u.c. DyBCO on LSAT, NGO and STO. (c) Comparison of the superconducting transition probed by the imaginary part of MI (red) and the resistance measurements (blue).

Quantum Design physical properties measurement system with temperatures ranging from 4-300 K. The resistance curves from the cooling and heating cycle were averaged to account for the temperature offset between the film and the temperature sensor. T_c^0 defines the temperature, where the resistance reaches zero within the instrumental resolution and indicates that a superconducting path formed through the film. Therefore, the information about sample inhomogeneity is limited to the lowest resistance path.

In comparison, the T_c value, determined by the onset of MI, is equal to the zero resistance T_c^0, determined by resistance measurements (Fig. 4.15c) [84]. To avoid confusion with different criteria for the superconducting transition determined by resistance measurement, such as T_c(onset), T_c(50 %) or T_c^0. In this thesis, T_c refers to the onset of the MI measurements.

The resistivity in regular metals is described with $\rho = \rho_0 + c \cdot T^5$,

where ρ_0 accounts for impurity scattering and the T^5 term accounts for phonon scattering [96]. The film quality is frequently compared by the residual resistivity ratio (RRR), which is obtained by dividing ρ at 300 K by the extrapolated ρ to T→0 K. In superconductors ρ is zero below the superconducting transition. Therefore, ρ just above T_c is frequently used instead of T→0 K for the RRR.

In high T_c cuprates, the strange metal phase above the superconducting transition is associated with a linear temperature dependence of ρ in optimally doped films. Deviations are observed in under- and overdoped films, e.g. when the pseudogap region is accessed or when a T^2 relation occurs at low temperatures [97]. Since the temperature dependence differs from normal metals and is not well understood, several criteria can be applied to compare the film quality. ρ(T→0 K) and ρ(100 K) can be used to compare the impurity scattering similar to normal metals. The RRR (ρ(300 K)/ρ(100 K)) reflects the linear temperature dependence, however, the deviation from the linear dependence in underdoped films limits the interpretation to the high temperature regime.

The comparison of ρ(T→0 K) and ρ(100 K) values of the films with similar thickness on different substrates reveals that films on LSAT exhibit the lowest resistivity (Tab. 4.1). The lattice of LSAT matches well with the lattice of DyBCO, thereby causing almost no epitaxial strain. The orthorhombic structure of NGO induces an in-plane tilt of the orthorhombic domains as well as a small compressive strain on the DyBCO lattice (sec. 5.2), thereby giving rise to more disorder and a higher resistance. STO has the highest lattice mismatch of the investigated substrates and causes more disorder, which provides scattering centers and therefore increases the resistivity. In one exception, a 10 u.c. film on NGO had a similar ρ(100 K) value as films on LSAT, however the ρ(T→0 K) was more than doubled, indicating a high disorder state after all.

	MI		van der Pauw			
	T_c (K)	ΔT_c (K)	T_c (K)	ρ(T→0 K) ($\mu\Omega cm$)	ρ(100 K) ($\mu\Omega cm$)	slope (mK^{-1})
grown on LSAT (100)						
10 u.c.	78.2	2.6	82.0	29.6	186	0.20
	77.1	2.2	80.9	31.6	189	0.21
20 u.c.	86.7	0.8	88.2	11.3	128	0.094
	84.9	2.2	-	-	-	-
50 u.c.	85.9	1.9	88.3	19.3	129	0.17
grown on NGO (110)						
10 u.c.	79.2	3.0	82.8	68.8	188	0.53
	78.5	3.0	81.7	217	537	0.58
20 u.c.	84.2	1.5	84.1	60.8	273	0.29
	83.7	1.8	-	-	-	-
40 u.c.	82.0	3.4	86.2	53.8	195	0.36
grown on STO (100)						
10 u.c.	72.9	2.3	77.2	55.8	221	0.34
	73.3	3.4	-	-	-	-
20 u.c.	81.6	2.0	84.6	61.5	203	0.40
	82.7	0.8	-	-	-	-
40 u.c.	81.1	3.1	86.0	31.9	145	0.28
60 u.c.	85.0	1.7	-	-	-	-

Table 4.1: Transport and mutual-inductance measurements (MI). For selected films, resistance measurements were performed in van der Pauw geometry, where T_c was determined with the 50 % criterion. The residual resistivity (ρ(T→0 K)) was extrapolated to 0 K based on the linear approximation between 240 K and 150 K (slope), where no instrument interference and no deviation from the linear trend were observed.

In addition, the resistivity can be used to compare the MBE grown films to other growth methods. NdBCO films on STO grown by sputtering [92] show a similar $\rho(100\ \mathrm{K})$ value ($\approx 200\ \mu\Omega cm$) as the DyBCO films on STO (100). YBCO films on NGO (110) grown by PLD [98] have a lower resistivity in thick films and a higher resistivity in thin films (10 nm). The best film in our study (20 u.c. on LSAT) has a higher $\rho(100\ \mathrm{K})$ than 123 cuprates grown on MgO, where values of less than 70 $\mu\Omega cm$ have been reported [88, 99, 100]. However, the last comparison considers films on different substrates and rather reveals the potential to further improve the resistivity through the choice of substrate.

In general, the MBE-grown DyBCO films are comparable with films grown by PLD and sputtering. The flexibility of the MBE growth gives easy access to tune the stoichiometry and to substitute the rare-earth elements in the deposition sequences.

4.4 Transfer to other rare-earth elements

In *RE*BCO the rare-earth ion (*RE*) is located between the superconducting CuO_2 planes. Similar to YBCO and DyBCO, the entire family of *RE*BCO is characterized by a T_c above 90 K [13–15], with a few exceptions such as $RE = \mathrm{Pr}$ due to the possible +IV oxidation state. Therefore, we investigated the replacement of Dy with Ho, Nd and Gd, which can all be used in a standard effusion cell. In the periodic table Ho is next to Dy, which also has a high magnetic moment and a similar ionic radius, making the transfer of growth technology easy. In addition, Gd and Nd were selected, since they have the highest and lowest orbital moment of the rare-earth elements.

In contrast to Dy, the corresponding effusion cells were less stable. Especially the Nd flux decreased during the deposition, causing a less controllable and less reproducible growth. For Gd, a high flux is only

	RE	T_c (K)	ΔT_c (K)
LSAT	Ho	77.8	0.8
	Nd	79.9	2.5
NGO	Gd	83.8	3.0
	Ho	74.8	2.3
	Nd	86.0	2.5
STO	Ho	80.4	1.2

Table 4.2: Superconducting properties of 20 u.c. *RE*BCO films characterized by MI.

obtained when the cell temperature was increased until an alloy with the tungsten crucible was thermodynamically stable. Therefore, the crucible has to be changed frequently to prevent destruction of the cell.

During growth, the same RHEED patterns and the same intensity oscillation as for DyBCO were observed. The main difficulty arose from the missing feedback for the termination of the *RE* layer, especially for the elements with less stable flux. Nevertheless, thin films without defects in XRD were obtained after a few test growths.

In comparison with 20 u.c. DyBCO films, the T_c of the *RE*BCO films is about 1-10 K lower (Tab. 4.2). The *RE* ion size causes a slight distortion in the unit cell, which can lead to a slight reduction or increase of T_c, depending on the ion size [13–15]. However, due the limited number of growth experiments for *RE*BCO films with $RE \neq$ Dy, the growth procedure for these films was not optimized. While for DyBCO more than hundred films were grown, the selection for the *RE*BCO films is limited to less than 10 films for each element with the exception of $RE =$ Nd. A total of 14 films was grown for Nd due to the low

stability of the Nd flux. The T_c of 76 K for NdBCO on NGO is comparable to DyBCO (84.1 K) and can be related to the better growth experience with the Nd cell. Considering the limited reproducibility of MBE growth and the small number of grown films, the obtained T_c is remarkable and confirms the application of the developed growth technology for DyBCO films as a general guideline to grow high quality *RE*BCO thin films.

The growth parameters and the RHEED feedback are frequently machine specific, especially due to the different growth kinetics causing a different growth mode. In a collaboration with the thin film group of Brookhaven National Laboratory, the DyBCO growth sequence was applied in the MBE setup of the OASIS project, which also uses ozone as the oxidation agent [101]. Although the element flux was about three times lower than in the setup used for this thesis, a similar RHEED feedback was obtained. Within two weeks, high quality DyBCO thin films with a sharp T_c and a transition around 80 K were obtained, confirming the general applicability of the growth technology.

4.5 Summary

Through extensive *in-situ* and *ex-situ* characterization, we have optimized the layer-by-layer MBE growth of DyBCO thin films. The *in-situ* feedback from the RHEED and the QCM allowed for a reliable control of the stoichiometry and the suppression of impurity phase formation. The *ex-situ* characterization has been done using various methods. Additionally, x-ray diffraction confirmed the formation of the single-phase 123 structure. AFM was used to investigate the surface and confirmed a low surface defect density. Furthermore, cross-section STEM of selected films revealed a sharp substrate-film interface and the reduction of 124 stacking faults. The superconducting transition tem-

perature was extracted from mutual inductance measurements. While very thin films show a reduced T_c, all films above 10 u.c. thickness have a $T_c > 80$ K. Resistivity measurements revealed that the films on LSAT have the lowest resistivity, while films on STO and NGO exhibit a higher resistivity assigned to the large lattice mismatch of STO and the orthorhombic nature of NGO. Furthermore, the microstructure of the films affects T_c and will be discussed in the next chapter.

We also showed how T_c can be reversibly tuned by annealing either in high ozone background pressure (high T_c with narrow transition width), or in a low background pressure (reduced T_c and increased transition width).

Finally, the optimized growth of DyBCO films was extented to other rare-earth 123 cuprates. For RE = Gd, Ho, Nd phase-pure REBCO films with a high T_c were synthesized.

To conclude, the optimized growth sequence for 123 cuprates provides a guideline for high quality thin films with a low defect density and a high T_c. Moreover, it sets the basis for the growth of heterostructures, where all advantages of MBE growth are exploited. For example, the low deposition energy, which creates sharp interfaces, or the degree of freedom in the stoichiometry, which allows the substitution and manipulation of individual layers. The high quality of the films also allows us to implant defects and investigate their effect on characteristic properties.

Chapter 5

Structural twinning in $DyBa_2Cu_3O_{7-\delta}$ thin films

The following chapter focuses on the structural properties and modifications arising from the heteroepitaxy with the underlying substrates. We will discuss the adjustment of the film lattice to the substrate and how the DyBCO structure changes from a pseudo-tetragonal to an orthorhombic structure with increasing film thickness. Furthermore, the investigation of the twin domain distribution and the influence of the oxygen content on the film structure are presented. The results have been published in [67].

The lattice mismatch of the substrate with the deposited film can have a crucial influence on the crystal structure of the film. To investigate such effects of heteroepitaxy, three substrates with different crystal structure and lattice mismatch were used: LSAT (100), NGO (110) and STO (100) (Tab. 5.1). To facilitate the comparison between the different substrates, the following discussion will use the pseudocubic notation for NGO.

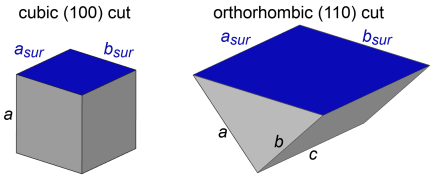

Figure 5.1: Sketch of the substrate cut and the surface (blue).

The lattice parameters of 123 cuprates depend on the oxygen content and can range from a tetragonal to an orthorhombic structure (Fig. 1.2) [17]. In the following discussion, the term bulk-like orthorhombic refers to DyBCO ($\delta = 0.1$) with the lattice parameters $a = 3.842$ Å, $b = 3.887$ Å and $c = 11.678$ Å (diagonal = 5.466 Å) [23]. Since the (pseudo-)cubic substrate favors the tetragonal phase, the mismatch with the bulk tetragonal DyBCO ($a = b = 3.868$ Å, $c = 11.811$ Å and diagonal = 5.470 Å (for $\delta = 0.75$) [22]) is also provided in Tab. 5.1. Depending on the oxygen content and the orthorhombicity of the film, the respective lattice mismatch changes. Therefore, the two presented cases in Tab. 5.1 serve as an estimate for the upper and lower boundary of the lattice mismatch.

After the utilization of specular XRD to confirm the phase formation and the determination of the c-lattice parameter (section. 4.2.1), the lattice mismatch with the substrate is investigated by probing scattering vectors with in-plane components (h or $k \neq 0$). The lattice adjustment along both in-plane directions is disentangled by keeping one in-plane direction zero. The required offset to probe the selected in-plane direction is placed into the θ motion, thereby arranging the cut of the line detector through the (k,l) ((h,l)) plane for $h = 0$ ($k = 0$). The substrate lattice is considered constant and serves as the reference system.

Substrat	surface			o-DyBCO		
	a_{sur} (Å)	b_{sur} (Å)	d_{sur} (Å)	ϵ_a (%)	ϵ_b (%)	ϵ_d (%)
LSAT (100)	3.87	3.87	5.473	0.72	-0.44	0.14
NGO (110)	7.726	7.708	10.913			
NGO (110) $\cdot\frac{1}{2}$	3.863	3.854	5.457			
NGO $(100)_{pc}$	3.858	3.858	5.457	0.42	-0.75	-0.17
STO (100)	3.905	3.905	5.523	1.61	0.46	1.04
Substrat				t-DyBCO		
LSAT (100)	3.87	3.87	5.473	0.05		0.05
NGO $(100)_{pc}$	3.858	3.858	5.457	-0.25		-0.25
STO (100)	3.905	3.905	5.523	0.95		0.95

Table 5.1: Surface lattice parameters (a_{sur}, b_{sur} and diagonal d_{sur}) of the used substrates and the respective in-plane lattice mismatch ϵ with orthorhombic bulk-like DyBCO (o-DyBCO) and tetragonal bulk-like DyBCO (t-DyBCO). The orthorhombic NGO (110) surface lattice parameters equal approximately two times the DyBCO lattice. For NGO also the pseudocubic notation (pc) is presented allowing for the comparison of the substrates. The lattice parameters of NGO and STO are from [102] and [103].

For a given detector resolution, the investigation of small peak splitting can be feasible by probing scattering vectors with high in-plane components, such as $h = 4$ instead of $h = 1$. Therefore, the experiments were carried out at the MPI beamline of the KARA synchrotron providing a high beam intensity and energy, and providing access to a large fraction of reciprocal space.

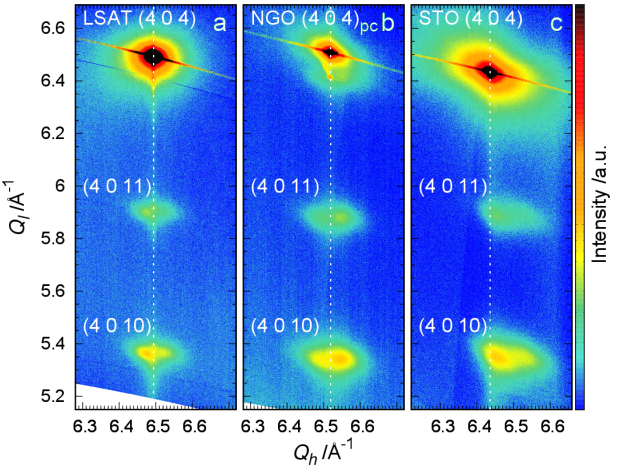

Figure 5.2: RSM of (4 0 l) plane of 20 u.c. thick films on (a) LSAT, (b) NGO and (c) STO in logarithmic intensity scale. The white lines mark the Q_h position of the substrate and are a guide to evaluate the in-plane lattice match.

5.1 Epitaxial strain

First, we draw the attention to the lattice mismatch with the substrate and the resulting epitaxial strain. Reciprocal space maps (RSMs) with large in-plane scattering vectors (h or k) and a wide range of the out-of plane vector (l) allow the comparison of the DyBCO peak position with respect to the substrate peak position. The effect of the substrate mismatch is shown for 20 u.c. thick films for $h = 4$ in Fig. 5.2.

The RSM of the 20 u.c. film on LSAT (Fig. 5.2a) reveals that the position of the (4 0 10) and (4 0 11) DyBCO peak is centered around the Q_h value of the substrate, indicating a matched in-plane lattice to the substrate. Looking closer, two faint peaks at higher and lower Q_h values are observed. Their positions roughly match the bulk-like

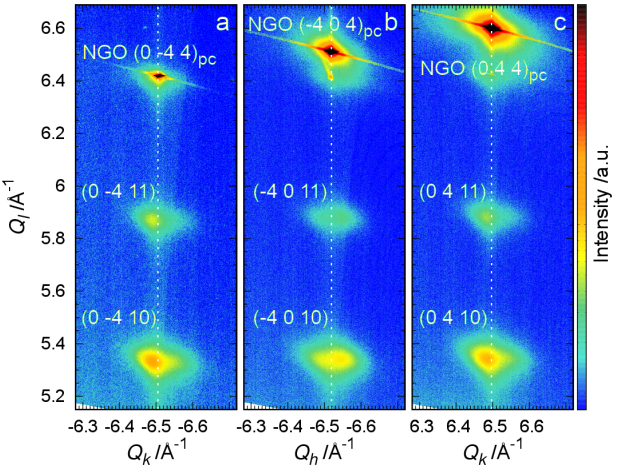

Figure 5.3: RSM of the (0 -4 l), (-4 0 l) and (0 4 l) plane of a 20 u.c. thick film on NGO with logarithmic intensity scale. The white lines mark the Q_k (Q_h) position of the substrate.

DyBCO in-plane lattice, revealing orthorhombic twin domains.

The orthorhombic crystal structure and the (110) cut of the NGO substrate cause a tilt of the crystallographic surface normal in relation to the surface. The tilting is seen in the Q_l position of the $(\pm 4\ 0\ 4)_{pc}$ and $(0\ \pm 4\ 4)_{pc}$ substrate peak, which shifts depending on the substrate orientation (Fig. 5.2b, 5.3). Nevertheless, the DyBCO Q_l values are independent of the substrate orientation, revealing that the film does not pick up the tilted crystal normal and that the DyBCO c-axis is perpendicular to the optical surface.

The RSMs of the 20 u.c. film on NGO (Fig. 5.2b, 5.3) show that the (±4 0 10) ((0 ±4 10)) and (±4 0 11) ((0 ±4 11)) DyBCO peak consist of two faint peaks each and that they are also centered around the Q_h (Q_k) value of the substrate, indicating a lattice adjustment to the rectangular surface of the NGO (110) substrate.

Despite the formation of orthorhombic twin domains, the DyBCO structure is adjusted to the substrate. Since the orthorhombic twinning occurs along the [110] and [1$\bar{1}$0] directions, the mismatch of the diagonals has to be considered. LSAT (NGO) provides a small tensile (compressive) strain (Tab. 5.1), therefore only small adjustments of the film lattice are required and the epitaxial strain can be sustained. The small mismatch of the diagonals can be either accommodated by reducing or stretching the a- and/or b-axes length of the DyBCO lattice or by changing the angle between the a- and b-axes. The larger Q_h (Q_k) value of the (4 0 10) ((0 4 10)) DyBCO peak on NGO compared to the film on LSAT, where Q_h and Q_k are equivalent due to the cubic substrate structure, indicates the adjustment of the in-plane DyBCO axes.

The lattice adjustment of DyBCO films on STO, which causes large tensile strain, is different than in films on LSAT and NGO. The RSM of 20 u.c. film on STO (Fig. 5.2c) reveals that the position of the (4 0 10) and (4 0 11) DyBCO peak is shifted from the Q_h value of the substrate, which indicates a film relaxation. For both DyBCO peaks orthorhombic domains are visible and the respective Q_h value matches with bulk-like orthorhombic DyBCO.

For the substrates with only small strain on the DyBCO structure (LSAT and NGO), the film adjusts to the substrate lattice, while for STO, which causes large strain, the strain relaxation towards the bulk-like DyBCO structure is observed. All films show orthorhombic domains, whose formation is discussed as a function of the thickness and the substrate in the next section.

5.2 Orthorhombic twinning

In single crystalline form, DyBCO undergoes a phase transition from the high temperature tetragonal to the low temperature othorhom-

bic structure analogous to YBCO [17]. Through epitaxial strain, a (pseudo-)cubic substrate can stabilize the tetragonal DyBCO phase. Nevertheless, orthorhombic twin domains are observed in thick films. By aligning the diagonals of the substrate and the diagonals of DyBCO unit cells, twinning along [110] and [1$\bar{1}$0] results in four twin domains akin to single crystals (Fig. 1.4) [30, 104, 105]. Therefore, the mismatch of the diagonals is crucial for the twinning.

RSMs of the (h,k) plane at a film peak can reveal all four domains, for example four equally spaced domains around the commensurate (0 k l) peak (Fig. 5.4a). The set of twin domains arising from one twinning plane (TP) are split, since they have either the a-axis (domain A in Fig. 5.4) or the b-axis (domain C) along the in-plane direction, resulting in a low Q_k (C) and high Q_k (A) value, while the splitting along Q_h arises from the orientation of the TP relative to the in-plane direction [29, 106]. Consequently, the two domain peaks at the commensurate (0 k l) position are actually more accurately labeled as (k 0 l) (A) and (0 k l) (C). At the commensurate (h 0 l) peak, the positions of the domains from the TP are reversed. Now domain A has the b-axis along the in-plane direction, resulting in a low Q_h, while C has a high Q_h. A similar observation is made for the domains of the second TP with a reversed splitting along Q_h due to the opposite orientation of the TP. The domains from both TPs form the characteristic four-fold twinning pattern at the (0 k l) and (h 0 l) peak.

The twinning was investigated at the (4 0 10) and (0 4 10) DyBCO peak, since the large in-plane component (h,k = 4) allows for the detection of small peak splitting, while no interference with the substrate is observed for l = 10.

First, we address the twinning as a function of the film thickness for films on LSAT. It provides an almost ideal lattice match for the tetragonal DyBCO lattice (Tab. 5.1).

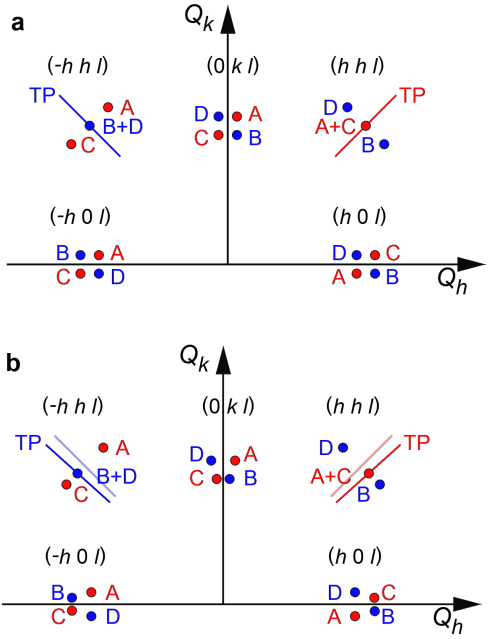

Figure 5.4: Sketch of the twin domain splitting in the (h,k) plane. Domain A and C arise from twinning along [110] (red), and B and D from twinning along $[1\bar{1}0]$ (blue). (a) On a square surface the twinning planes (TP) are perpendicular to each other, while (b) the TPs are tilted on a rectangular surface, resulting in a shift of the twin domain positions. The dark lines in (b) represent the tilted TPs, while the light lines indicate the reference position of perpendicular TPs.

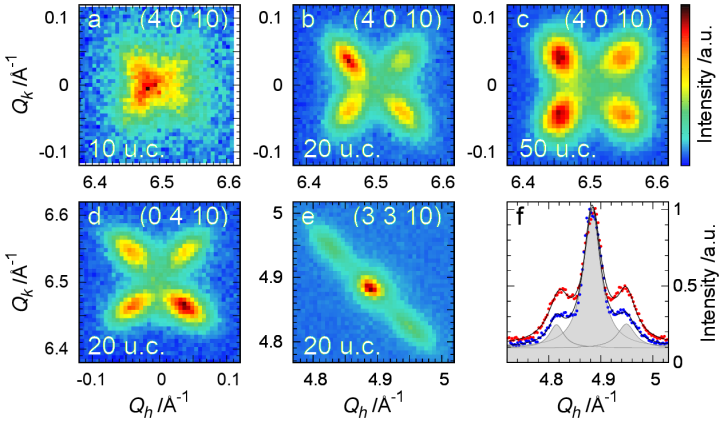

Figure 5.5: Twinning of films on LSAT. RSM of the (4 0 10) peak of (a) 10 u.c., (b) 20 u.c. and (c) 50 u.c. thick films. RSM of the (d) (0 4 10) and (e) (3 3 10) peak of the 20 u.c. thick film. (f) hk-scans perpendicular to the TP across the (3 3 10) (red) and (3 -3 10) (blue) peak normalized to 1 and projected on Q_h are shown for the 20 u.c. film. The Lorentzian fit is shown as a black line and for the scan at (3 -3 10) the individual functions are displayed in gray. All intensities are plotted on a linear scale.

The RSM around the (4 0 10) peak of 50 u.c. DyBCO on LSAT (Fig. 5.5c) contains four well separated, circular-shaped peaks. The individual peak positions match roughly with the lattice of bulk orthorhombic DyBCO, indicating bulk-like twinning.

In films with 20 u.c. thickness on LSAT (Fig. 5.5b), the fourfold twinning is still visible, but the Q_h values are shifted towards the commensurate (4 0 10) position. This suggests that the cubic substrate impedes the twinning and reduces the film's orthorhombicity. In addition, the peaks have an elliptical shape, indicating a distribution of the a- and b-lattice parameters, where the interface layers are expected to

be more strained than the surface layers.

The trend is even more striking when looking at the 10 u.c. thick film (Fig. 5.5a), where the fourfold twinning is very small. The high intensity at the commensurate (4 0 10) position rather implies a tetragonal DyBCO structure. The shape of the RSM can be interpreted as an incipient twinning, where the layers close to the interface are strained to the substrate and adapt a tetragonal lattice while the topmost layers start to form orthorhombic domains. The high T_c ($\approx$ 78 K) and sharp superconducting transition of the 10 u.c. film suggests that the doping level must be close to optimally doped. At first sight, the tetragonal structure and the high T_c appear contradicting, since the onset of superconductivity and the tetragonal-to-orthorhombic phase transition in single crystals coincide at the same oxygen content [17]. However, if alternating short-range CuO chain segments form, the overall structure will appear tetragonal, while the T_c is high [107]. Therefore, the observed structure in the 10 u.c. film is assigned to a pseudo-tetragonal structure.

For ultra-thin films ($\leq$ 7 u.c. thickness) degradation was observed, making these films unsuitable for long time synchrotron radiation exposure. Consequently, they were not investigated.

The study of the LSAT films shows that the film thickness can be used to tune the structure of the thin films. While thick films show almost bulk-like orthorhombic twinning, very thin films reveal a strong reduction of the orthorhombicity. The matching lattice of the film with the substrate can neither be confirmed, nor denied due to the small lattice mismatch (Tab. 5.1), especially when considering a tetragonal DyBCO lattice as stabilized in the 10 u.c. film.

The formation of orthorhombic twin domains on NGO shows a similar thickness dependence as the films on LSAT: thick films (40 u.c.) have well separated orthorhombic domain peaks (Fig. 5.6c), while in the 20 u.c. film an elongation of the peaks and a slight reduction of

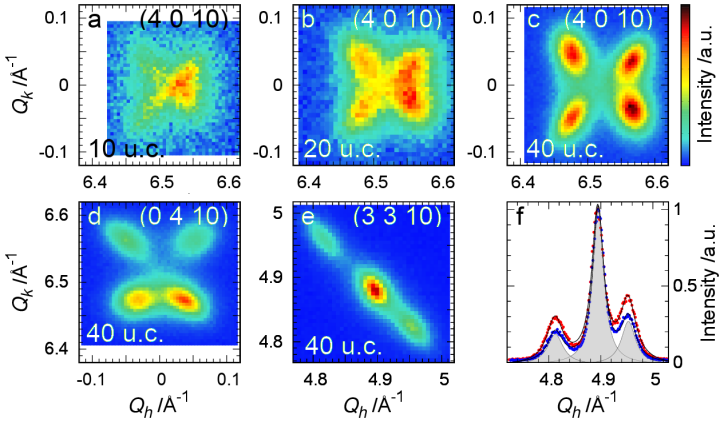

Figure 5.6: Twinning of films on NGO. RSM of the (4 0 10) peak of (a) 10 u.c., (b) 20 u.c. and (c) 40 u.c. thick films. RSM of the (d) (0 4 10) and (e) (3 3 10) peak of the 40 u.c. thick film. (f) hk-scans perpendicular to the TP across the (3 3 10) (red) and (3 -3 10) (blue) peak normalized to 1 and projected on Q_h are shown for the 40 u.c. film. The Lorentzian fit is shown as a black line and for the scan at (3 -3 10) the individual functions are displayed in gray. All intensities are plotted on a linear scale.

the orthorhombicity is observed (Fig. 5.6b), and in the 10 u.c. film a strong reduction of the orthorhombicity towards a pseudo-tetragonal structure is present (Fig. 5.6a).

Despite the similar behavior, the RSMs of the films on NGO look differently. The rectangular surface of NGO (110) generates a tilt of the two TPs, shifting the positions of the twin domains accordingly (Fig. 5.4b). In the 40 u.c. film, the tilting is observed in the RSMs at the (4 0 10) position as a smaller Q_k distance at higher Q_h values and at (0 4 10) as a smaller Q_h distance at lower Q_k, respectively (Fig. 5.6c, d).

In the 40 u.c. film, the center of the (4 0 10) ((0 4 10)) film peak matches with the Q_h (Q_k) value of the substrate along each direction, confirming the adjustment of the DyBCO lattice to the substrate and, consequently, a slight compression of the DyBCO a- and b-lattice parameters. Nevertheless, the splitting ΔQ of the domains arising from a TP is similar to the films on LSAT: almost no splitting in the 10 u.c. film, a mild splitting of $\Delta Q \approx 0.07$ Å^{-1} (≈ 0.08 Å^{-1}) along both directions for the 20 u.c. on NGO (LSAT), and $\Delta Q \approx 0.09$ Å^{-1} (≈ 0.09 Å^{-1}) along both directions for the 40 (50) u.c. film on NGO (LSAT). Therefore, the orthorhombicity can be considered independent of the lattice mismatch, while the length of the DyBCO a- and b-axes are adjusted.

Now we turn the discussion to the twinning of DyBCO on STO (100), which has the largest lattice mismatch among the investigated substrates (Tab. 5.1). In the RSM around the (4 0 10) peak of 60 u.c. on STO (Fig. 5.7h), a similar fourfold twinning pattern with circular-shaped peaks as for the 40 u.c. films on LSAT is observed. The peak position and splitting matches with the lattice of bulk DyBCO, revealing full strain relaxation.

In the (4 0 10) RSM of the 40 u.c. film (Fig. 5.7e) the Q_h positions match with the bulk-like DyBCO lattice, but along Q_k only one broad peak is visible. Nevertheless, the extracted k-scan can be best fitted by two Lorentzian functions indicating that, overall, four domains are still present with an overlap along k (Fig. 5.7f). Similar observations are made for the (0 4 10) peak, where the splitting along Q_h is reduced and Q_k matches with bulk-like DyBCO (Fig. 5.7d).

For the 20 u.c. thick film, the spacing along Q_h is in good agreement with bulk DyBCO, but along Q_k the peak is narrow and the respective k-scan is best described with a single Lorentzian function (Fig. 5.7b, c). Therefore, only two domains split along h are present, suggesting a twinning along [100] and [010]. Again, the same observation is made

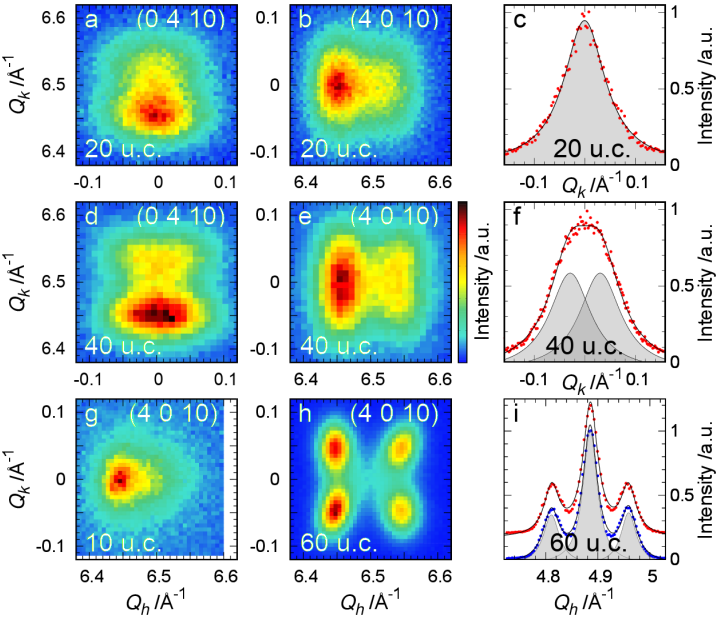

Figure 5.7: Twinning of films on STO. RSM of the (4 0 10) peak of (g) 10 u.c., (b) 20 u.c., (e) 40 u.c. and (h) 60 u.c. thick films. RSM of the (0 4 10) peak of the (a) 20 u.c. and (d) 40 u.c. film. (c, f) The h-scans of the (4 0 10) peak at $Q_k \approx 6.46$ Å^{-1} for the (c) 20 u.c. and (f) 40 u.c. film normalized to 1 and fitted with Lorentzian functions (black line, individual functions are displayed in gray). (i) hk-scans perpendicular to the TP around the (3 3 10) (red) and (3 -3 10) (blue) peak normalized to 1 and projected on Q_h shown for the 60 u.c. film. The Lorentzian fit is shown as a black line and for the scan at (3 -3 10) the individual functions are displayed in gray. All intensities are plotted on a linear scale.

for the (0 4 10) peak (Fig. 5.7a), where the two domains are separated along Q_k. The higher intensity at Q_h (Q_k) $\approx$ 6.45 Å^{-1} can be attributed to the tensile strain from the cubic substrate, which favors a tetragonal DyBCO structure with in-plane lattice parameters close to the substrate ($Q_h(STO) = 6.44$ Å^{-1}).

The RSM at the (4 0 10) peak of the 10 u.c. film (Fig. 5.7g) shows a strong peak at $Q_h \approx 6.45$ Å^{-1}, suggesting a tetragonal structure with lattice parameters close to STO. The additional intensity trace towards higher Q_h indicates a beginning of twin formation. Due to the high T_c of the 10 u.c. film, the observed pattern is also assigned to a pseudo-tetragonal structure.

In contrast to the other substrates compared in this study, the orthorhombic twin formation on STO shows a change in the TP's orientation as a function of the film thickness. While for intermediate thicknesses the DyBCO films form twin domains along [100] and [010] resulting in two domains with nearly bulk lattice parameters, in thicker films the TPs change from [100]/[010] to [110]/[1$\bar{1}$0]. The gradual change can be seen in the 40 u.c. film (Fig. 5.7d, e), while the fourfold pattern is clearly observed in the 60 u.c. film (Fig. 5.7h).

These observations are different to the ones published for NdBCO films on STO, where at 20 u.c. a tetragonal-to-pseudo-tetragonal and at $\approx$ 60 u.c. a pseudo-tetragonal-to-orthorhombic phase transition was reported [92]. The difference can be assigned to the measurement of (h,l) / (k,l) RSMs, which only show a projection of the domains, while the (h,k) RSMs detect all domains.

By analyzing the RSM in the (h,k) plane around the (4 0 10) DyBCO peak, we investigated the formation of orthorhombic twin domains as a function of the film thickness. All 10 u.c. thick films revealed a pseudo-tetragonal structure and consequently a strong suppression of the othorhombicity by the substrate. In the 20 u.c. thick films, a weak suppression of the orthorhombicity and the formation of orthorhom-

bic domains was observed on all substrates. While films grown on substrates with small lattice mismatch (LSAT and NGO) formed orthorhombic domains by twinning along [110]/[1$\bar{1}$0] akin to bulk single crystals, films on STO, which provides a large tensile strain, formed orthorhombic domains by twinning along [100]/[010] and transferred to the twinning along [110]/[1$\bar{1}$0] in thick films.
Furthermore, the films on LSAT and NGO adjusted their lattice to the substrate lattice, despite forming twin domains. In contrast, the films on STO relaxed quickly and already 20 u.c. thick films showed a strong relaxation towards bulk-like lattice parameters. Nevertheless, the STO stabilized the intermediate twinning along [100]/[010] up to 40 u.c. film thickness, revealing effects of the substrate lattice despite a bulk-like orthorhombic DyBCO structure.
The observations also imply that the formation of orthorhombic domains and the substrate strain relaxation are not equivalent. The films on NGO revealed that, despite the formation of orthorhombic domains, the film lattice is adjusted to the substrate, and the films on STO showed that, despite bulk-like orthorhombic domains, in intermediate film thicknesses, the direction of the TPs is different than in bulk.

5.3 Domain distribution

After discussing the formation of the orthorhombic twin domains, we now focus on the population of the formed domains. The RSM around the (4 0 10) ((0 4 10)) peak reveals an asymmetric intensity distribution of the high and low Q_h (Q_k) peaks. The set of twins arising from one TP at the (4 0 10) peak are the corresponding (4 0 10) (A) and (0 4 10) (C) for the domains (Fig. 5.4). Therefore, the set of twin domains should have different intensities due to the different structure factors connected to the orthorhombic lattice structure.

At the commensurate (0 4 10) peak, the positions of the domains from one TP are reversed and the intensity ratio between the high and low Q_k should be similar to the ratio of the high and low Q_h at (4 0 10). However, if the domains are not equally occupied, the intensity ratio can differ between both commensurate peaks.

A convenient way to determine the occupation are RSMs of film peaks along the twinning directions (h h l) and (h $-h$ l). For example the (3 3 10) film peak lies along the [110] direction, resulting in a superposition of the two twin domains from twinning along [110] (A and C), while the two domains from twinning along [1$\bar{1}$0] (B and D) are split (Fig. 5.4 for $h = 3$). At the (3 3 10) peak the respective hk-scan perpendicular to the [110] direction allows for the extraction of the domain occupation of domain B and D relative to the superimposed domains A and C. Since the split peaks correspond to the (-3 3 10) (B) and (3 -3 10) peak (D), the structure factors are equal and the peak intensity can be compared directly. Similar to the hk-scan at (3 3 10), the occupation of A and C can be obtained from the hk-scan at (3 -3 10) or (-3 3 10).

The focus is first drawn to the domain occupation in the 20 u.c. film on LSAT. In the RSM around the (4 0 10) DyBCO peak (Fig. 5.5b), the twin peaks at lower Q_h values exhibit a higher intensity than their respective twins at higher Q_h. Also in the RSM at the (0 4 10) DyBCO peak (Fig. 5.5d) the domains at lower Q_k have a higher intensity. In addition, in both RSMs an intensity difference between the twins from one TP compared to the twins of the other TP is visible. Hence, the attention is drawn to the (3 3 10) and (3 -3 10) DyBCO peak where the domain occupation is more easily accessible.

The RSM and the hk-scan at the (3 3 10) peak (Fig. 5.5e, f) consist of a strong central peak, arising from the superimposed twin domains and two side peaks, arising from twinning along [1$\bar{1}$0]. The intensity of the two side peaks is equal, indicating an equivalent occupation of the

domains. The *hk*-scan at (3 -3 10) has a similar shape indicating an equivalent occupation of the domains from twinning along [110] as well. Nonetheless, when comparing the scans of the (3 3 10) and (3 -3 10) film peak, the intensity ratio of the split domains to the central peak is different. This suggests a preferred twinning along one TP over the other. For the 20 u.c. film on LSAT, the ratio is $\approx$ 2:1 for twinning along [1$\bar{1}$0] compared to twinning along [110].

From previous studies, it is known that the substrate miscut and the orientation of the step edges cause additional strain and allow for manipulation of the twinning [29, 89, 108]. For example, a step orientation along [110] and a miscut above 0.6 ° suppresses one set of twin pairs completely [89]. For the DyBCO films the step orientation was not recorded and the island formation inhibits the determination after growth. Nevertheless, for cubic substrates with a miscut below 0.5 °, the observed preferred twinning agrees with YBCO films on STO with a similar miscut [89].

Next, the domain occupation of films on STO is briefly addressed. The DyBCO films on STO with intermediate thickness have only two domains, which can be accessed at the (4 0 10), as well as the (3 3 10) peak position. Due to the broad peak shape, the domain peaks overlap at the (3 3 10) position. Nevertheless, the twin distribution can be estimated using the (4 0 10) and (0 4 10) domain intensities (Fig. 5.7a, b, d, e). Since the intensity ratios are almost equal, an approximate 1:1 occupation of each domain is estimated. For the 60 u.c. film the almost equal population is seen in the comparison of the two scans across the (3 3 10) and (3 -3 10) peak, where the ratio between the central peak and the two twinned domains is similar for both directions (Fig. 5.7i).

The domain occupation of DyBCO on NGO is different compared to the other substrates. NGO (110) has a rectangular surface (a_{sur} = 2 $\times$ 3.863 Å, b_{sur} = 2 $\times$ 3.854 Å) and thus causes different strain

on the orthorhombic DyBCO *a*- and *b*-axes: the substrate a_{sur}-axis causes 0.54 % (-0.63 %) strain along the DyBCO *a*- (*b*-)axis and the b_{sur}-axis causes 0.3 % (-0.86 %) strain. Therefore, the total strain can be minimized by a preferred alignment of the DyBCO *b*-axis along the NGO a_{sur}-axis, which is the NGO_{ortho} $(1\bar{1}0)$ direction, and the DyBCO *a*-axis along the NGO b_{sur}-axis, which is the NGO_{ortho} (001) direction.

The domain occupation on NGO is discussed for the 40 u.c. DyBCO film, where the domains are well-separated. The *hk*-scan at the (3 3 10) and (3 -3 10) film peak reveals three peaks, which are asymmetrically spaced due to the substrate cut (Fig. 5.6e, f). The superimposed domains of one TP are not centered between the domains of the other TP, but are shifted according to the tilt of the TPs relative to each other.

Similar to the 20 u.c. film on LSAT, a different intensity distribution is observed for the (3 3 10) and (3 -3 10) peak, revealing the preference of one TP over the other (Fig. 5.6f). Furthermore, in both scans the side peak with higher Q_h and lower $|Q_k|$ values have a higher intensity than the respective twin. This indicates that for both TPs a preferred occupation of one twin domain over the other is present. Based on a Lorentzian peak modeling, the ratio is $\approx$ 1:1.3 for the 40 u.c. film and $\approx$ 1:1.5 for the 20 u.c. film. This observation agrees with the preferred alignment, where the DyBCO *a*-axis favors the alignment with the NGO b_{sur}-axis and the DyBCO *b*-axis with the NGO a_{sur}-axis.

The uneven domain distribution can also be seen in the (4 0 10) and (0 4 10) peak (shown for 40 u.c. DyBCO in Fig. 5.6c, d), where the individual peak intensities around the (4 0 10) peak are almost equal and differ from the intensity ratio of the (0 4 10) peak.

By using a substrate with a rectangular surface, an anisotropic domain distribution can be obtained. While on LSAT and STO the domains from one TP are populated equally and preferences of one TP over

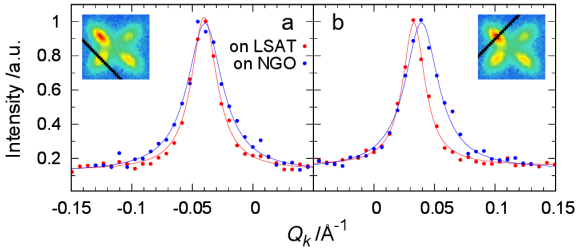

Figure 5.8: hk-scans extracted from the (4 0 10) RSM of 20 u.c. on LSAT (red) and on NGO (blue), normalized to 1 and projected on Q_k. The cut of the extracted scan with respect to the twin domains is shown in the inset as a black line (RSM of the 20 u.c. film on LSAT).

the other arise from the substrate miscut and edge orientation, the rectangular surface of NGO (110) induces an anisotropic domain distribution, where the domains with the longer DyBCO axis prefer to align with the longer substrate in-plane axis.

5.4 Mosaicity

After studying the domain distribution, we now discuss the angular spread of the crystalline domains (mosaicity). The mosaicity is important for the transport, since the domain boundary itself is a lattice potential change that causes scattering. Typically the mosaicity is obtained from rocking curves at the peak position. Since the commensurate film peak position consists of multiple twin domains, rocking scans need to be centered on the individual twin domains to obtain useful information. However, similar information can be obtained from the RSM at the (4 0 10) peak by extracting hk-scans transversal to the individual domains. The angular spread is then extracted from the θ and χ angles corresponding to the reciprocal-space coordinates. Using the RSMs of the 20 u.c. thick films, the full width half maximum

(FWHM) of the rocking curves are ≈ 0.35 ° and 0.3 ° on LSAT, ≈ 0.5 ° and 0.48 ° on NGO, and ≈ 1.1 ° on STO (Fig. 5.8, 5.7c). The angular spread suggests larger overall domain sizes for LSAT, which also correlates with the high $T_c \approx 86$ K. For NGO and STO the smaller domain sizes, as well as the different lattice parameters and for STO even the different twinning direction correlate with the lower T_c (≈ 84 K (NGO) and ≈ 82 K (STO), Tab. 4.1).

5.5 Doping dependence

So far, the discussion about twinning focused on fully oxidized thin films. By reducing the oxygen content, a transition from the orthorhombic towards a tetragonal structure akin to single crystals is observed. In order to investigate the structure evolution, fully oxidized, as grown films were cut into four pieces and each one was subsequently annealed to obtain a different oxygen content, deduced from the measurement of T_c. Thereby, the obtained results can be linked directly to the oxygen content without the need to consider variations arising from the film growth, such as the defect density.

In the 20 u.c. film on LSAT, twin domains with a noticeable reduction of the orthorhombicity are visible at $T_c \approx 65$ K (Fig. 5.9a). Upon further reduction to $T_c \approx 50$ K, the orthorhombicity is completely suppressed and a single peak is present, suggesting a pseudo-tetragonal structure (Fig. 5.9b). It should be mentioned that the observed structural transition is observed for multiple sets of samples, but the T_c for the individual stages varied. The different stages can be assigned to the film thickness, resulting in a different initial degree of orthorhombicity, and also to the defect density of the film.

The structural changes upon oxygen loss are analogous for films on NGO. For a 20 u.c. film on NGO with $T_c \approx 45$ K, twinning and a

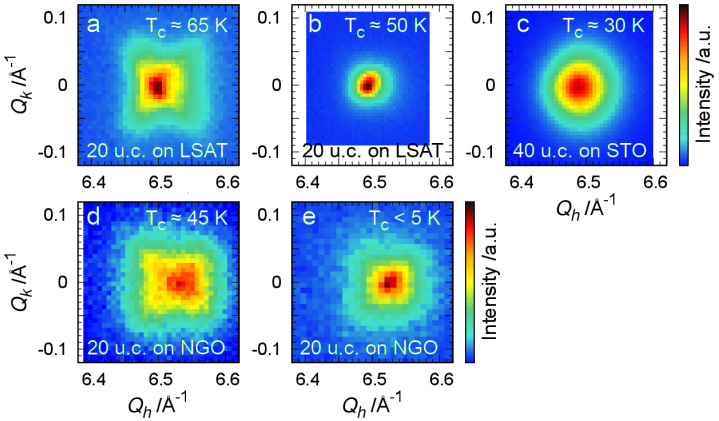

Figure 5.9: RSM around the (4 0 10) DyBCO peak for (a,b) a 20 u.c. film on LSAT with $T_c \approx 65$ K (a) and ≈ 50 K (b), (c) for a 40 u.c. film on STO with $T_c \approx 30$ K, and (d,e) for a 20 u.c. film on NGO with $T_c \approx 45$ K (d) and < 5 K (e).

reduced orthorhombicity is observed (Fig. 5.9d). By reducing the film further, a tetragonal structure is obtained as demonstrated for a film with a T_c below 5 K (Fig. 5.9e).

On STO 40 u.c. thick films were investigated, since the fully oxidized 20 u.c. films already show a reduced orthorhombicity. Similar to the films on NGO and LSAT, the reduced film on STO shows a transition to a pseudo-tetragonal phase with tetragonal bulk-like lattice parameters (Fig. 5.9c). In contrast to the 10 u.c. fully oxidized film (Fig. 5.7g), where the pseudo-tetragonal structure is strained to the substrate, the reduced 40 u.c. film is relaxed. This supports that the large substrate strain can only be accommodated in very thin films.

The in-plane lattice match can also be seen in the RSM around the (4 0 l) plane (Fig. 5.10). While reduced films on NGO and LSAT are strained and have an in-plane lattice matching to the substrate, the

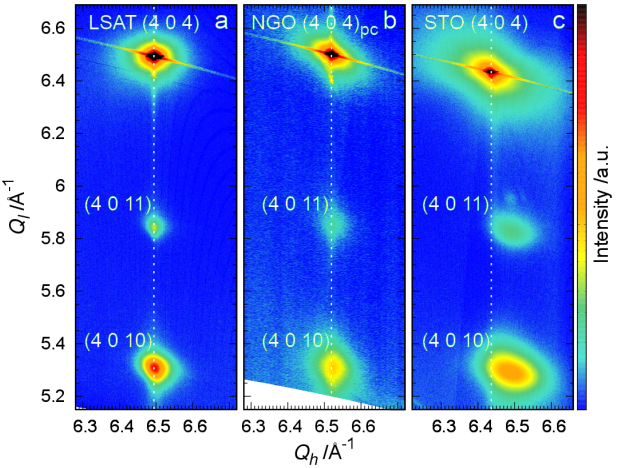

Figure 5.10: RSM along (4 0 l) of (a) 20 u.c. films on LSAT with T_c $\approx$ 50 K, (b) 20 u.c. on NGO with $T_c < 5$ K and (c) 40 u.c. on STO with $T_c \approx 30$ K in logarithmic intensity scale. The white lines mark the Q_h position of the substrate.

reduced film on STO is relaxed and has a bulk-like tetragonal lattice. This is in accordance with the observations from the fully oxidized films. Films grown on a substrate with a small lattice mismatch (LSAT and NGO) can adjust their structure to the substrate lattice, while films on substrates with large lattice mismatch (STO) are relaxing more quickly to the bulk-like lattice.

5.6 Summary

In this chapter we presented the investigation of the effects of the substrate surface lattice onto the microstructure of DyBCO films.
We showed how orthorhombic twin domains are formed as a function

of the film thickness. In very thin films (10 u.c.), the orthorhombicity is strongly suppressed and a pseudo-tetragonal DyBCO phase forms, where alternating short-range CuO chain segments are present, but the overall structure appears tetragonal. In 20 u.c. thick films, the orthorhombicity is slightly reduced, but the formation of orthorhombic domains was observed. Films thicker than 20 u.c. have an orthorhombic twinned structure. The films grown on LSAT and NGO form the orthorhombic domains by twinning along [110]/[1$\bar{1}$0] akin to single crystals, while in thin films on STO twins along [100]/[010] are formed that change to twinning along [110]/[1$\bar{1}$0] in thick films.

Furthermore, we showed that the DyBCO films on LSAT and NGO adjusted their lattice to the one of the substrate, despite forming twin domains. In contrast, the films on STO relaxed quickly and already 20 u.c. thick films exhibited bulk-like lattice parameters. This behavior suggests that the formation of orthorhombic domains and the substrate strain relaxation are two separate processes that are not easily linked.

Another intriguing result in this regard are the films grown on the (110) facet of NGO. This cut provides an anisotropic lattice mismatch and induces an anisotropic twinning, where the DyBCO *b*-axis preferentially aligns with the longer in-plane axis of the substrate.

Finally, the effect of oxygen reduction on the microstructure was presented. Similar to single crystals, the DyBCO thin films undergo an orthorhombic-to-tetragonal phase transition upon reduction of the oxygen content.

In summary, our study revealed a complex interplay of lattice mismatch, film thickness and oxygen content. We show possibilities, how heteroepitaxy can be used to systematically tune the structure of DyBCO and thus manipulate its lattice degree of freedom.

Chapter 6

Resonant scattering study of DyBCO thin films

With a detailed analysis of the structure and the twinning of DyBCO films at hand, we now turn to possible modifications of the collective charge ordered state probed by resonant x-ray scattering (RXS). By tuning the x-ray energy to particular absorption edges, the scattering signal becomes very sensitive to electronic and magnetic interactions of a specific ion. Within the scope of this thesis we performed scattering experiments at the Cu L_3 absorption edge and the Dy M_5 absorption edge. The measurements were done at the UE56 PGM-1 beamline of the Helholtz-Zentrum Berlin at the BESSY-II synchrotron, where magnetic fields up to 6 T can be applied to the film. The results are under review for publication [109].

In cuprates, many competing phases can be accessed by changing temperature, by applying pressure, by introducing doped carriers, and by applying a magnetic field. In addition to superconductivity, a long range charge order stabilizes in underdoped cuprates at low temperatures (sec. 1.4). Using x-ray diffraction on YBCO single crystals, the

formation of a charge density wave (CDW) in the CuO_2 planes was detected [38, 39, 110]. This CDW competes with superconductivity and by applying a magnetic field, which suppresses superconductivity, the signal grows below T_c [39–42]. This CDW does not have long-range correlations along the c-direction and rather has a 2D nature. This can be anticipated since mainly the Cu ions in the CuO_2 planes are involved. Nevertheless, by applying very high magnetic fields, a correlation along the c-direction is observed, forming a 3D CDW [2, 43, 111]. Recently, a 3D CDW was also observed in YBCO thin films in zero magnetic field and was attributed to the pseudo-tetragonal structure of the film[4]. Therefore, thin films allow for the investigation of this novel ordered states without the technical challenges arising from the application of high magnetic fields. In thin films the probed signals are weak and frequently beyond detection to non-resonant x-ray scattering. By tuning the x-ray energy to an absorption edges, the signal can be enhanced and becomes particularly sensitive to the electronic interactions of the resonant ion.

6.1 Cu L_3 edge resonance

YBCO served as a model system for the high T_c cuprates and has been investigated extensively [38, 42, 110, 112]. In order to establish similarities to the less studied DyBCO and to investigate the influence of the large, paramagnetic Dy magnetic moments, resonant x-ray scattering tuned to the Cu L_3 edge was used.

123 cuprates contain two different Cu sites per unit cell: the Cu(1) ions in the CuO chain layer and Cu(2) ions in the CuO_2 planes (Fig. 1.1). RXS at the Cu L_3 edge promotes electrons from the $2p$ orbital to unoccupied d states (sketch of RXS in Fig. 3.1). For simplicity the filled inner shells are omitted in the following electron configurations. The Cu(1) electron configuration depends on the oxygen doping and

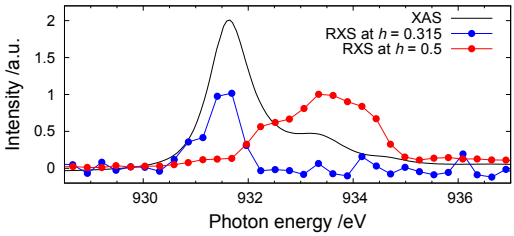

Figure 6.1: Energy profile of the reflection at (0.315 0 1.45) and (0.5 0 0.88) at the Cu L_3 edge, shown together with the x-ray absorption spectra (XAS). The data were taken at 5 K with no applied field and σ polarization of the x-rays.

evolves from a $3d^{10}$ for empty chains to a $3d^9 + 3d^9\underline{L}$ configuration for filled chains, where $\underline{L}$ indicates a hole in the oxygen $2p$ orbital (sec. 1.3)[112, 113]. The doping of the chain layers also generates a mild doping of the Cu(2) ions in the CuO_2 planes, which results in a configuration between the undoped $3d^9$ and the doped $3d^9 + 3d^9\underline{L}$ configuration. The different configurations give rise to an x-ray absorption fine structure with peaks at 931.7 eV ($3d^9$), 932.7 eV ($3d^9\underline{L}$) and 934.3 eV ($3d^{10}$) [112]. Therefore, energy profiles allow connecting the observed ordered states with the Cu(1) or Cu(2) ion and consequently link them to the CuO chain or CuO_2 plane layer.

In order to investigate charge ordering, reduced 20 u.c. DyBCO films on NGO (110) with $T_c \approx 55$ K were investigated by synchrotron x-ray scattering. After the experiments, the T_c of the probed films was reduced by up to 20 K compared to the initial value. The possible origin of this degrading is related to the required high vacuum conditions for low x-ray energy experiments as well as the substrate-induced

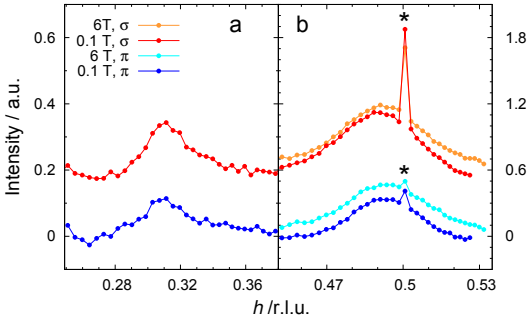

Figure 6.2: Rocking curves projected onto the reciprocal h direction at (a) (0.315 0 1.45) (CDW) and (b) (0.5 0 0.88) (ortho-II order) for DyBCO at the Cu L_3 edge (931.7 eV) at 5 K. The scans are vertically shifted for clarity. The sharp spike (marked with *) arises from the substrate.

strain, which favors of the non-superconducting tetragonal phase (see sec. 4.3.1). Despite the degrading of T_c, the observations were reproduced for two samples, confirming the validity of the results.

6.1.1 Charge order at the Cu L_3 edge

In the investigated DyBCO films, a CDW peak is detected at a wave vector of ≈ (0.315 0 1.45) (Fig. 6.2a). The corresponding energy profile has a maximum intensity at ≈ 931.7 eV, clearly linking it to the CuO_2 planes with primarily $3d^9$ configuration (Fig. 6.1).
The temperature dependence reveals an onset of the CDW between 150 and 100 K and a maximum at ≈ 60 K, which approximately matches with T_c (Fig. 6.3a). The temperature difference between T_c (55 K) and the CDW maximum intensity is assigned to the uncertainty in the determination of the maxmimum CDW intensity and the determination of T_c by MI, where T_c corresponds to the zero resistance value and not

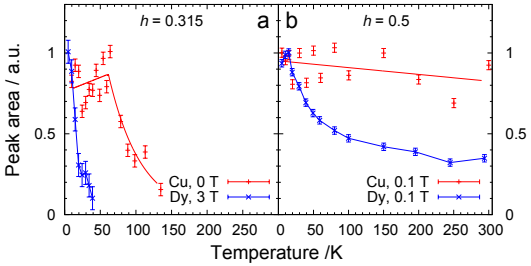

Figure 6.3: Temperature dependence of (a) the CDW peak ($h = 0.315$) and (b) the ortho-II peak ($h = 0.5$) at the Cu L_3 edge (931.7 eV) and at the Dy M_5 edge ((a) 1293.1 eV, (b) 1293.8 eV) with an applied magnetic field as indicated. The lines are guides to the eye. The results at the Dy M_5 edge are discussed in section 6.2.

the onset temperature (sec. 4.3.1). By cooling below the superconducting transition, the intensity of the CDW peak decreases, indicative of the competition between charge order and superconductivity.
Interestingly, the application of magnetic fields up to 6 T has almost no effect on the CDW peak intensity (Fig. 6.4). This behavior seems to disagree with the scenario of a competition between the CDW and superconductivity, where the magnetic field weakens the superconducting state and thereby could give rise to an enhanced CDW intensity. The origin of the field-insensitivity may be related to pinning of CDW domains to defects, where superconductivity is suppressed.
YBCO single crystals with a T_c in the same range as the DyBCO films also show almost no field effect [42]. The similarity between theses single crystals and the DyBCO films indicates that in the investigated temperature and magnetic field range, the substitution of Y by Dy, the element with the highest magnetic moment [16], does not effect the superconductivity in the neighboring CuO_2 planes.
After confirming that the CDW observed in DyBCO thin films is com-

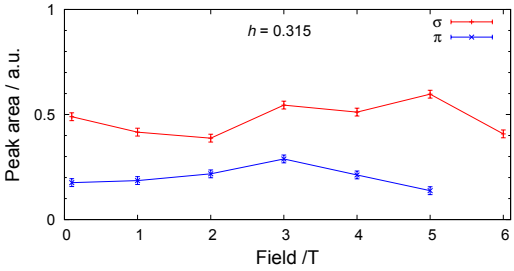

Figure 6.4: Magnetic field dependence of the CDW peak ($h = 0.315$) at the Cu L_3 edge (931.7 eV) at 5 K with with different polarization (σ and π) of the incident x-ray beam.

parable to the CDW in similarly doped YBCO single crystals, the attention is drawn to the dimensionality of the CDW.

In a 2D CDW, the order is confined in the CuO_2 plane and therefore a broad peak along l is observed. For YBCO single crystals a maximum at half values, for example $l = 0.5$, was reported, indicating an anti-phase modulation of the CDW between neighboring CuO_2 planes [39, 40]. The additional correlation along the c-axis, which forms a 3D CDW, is indicated by the formation of strong peaks at integer l values in addition to the broad 2D CDW signal [2, 4, 43, 111].

RXS with the photon energy tuned to the Cu ions in the CuO_2 planes (931.7 eV) was used to perform multiple rocking curves at different l values in order to obtain a RSM (Fig. 6.5a). An extended intensity along l with a maximum near $l = 1.5$ was obtained indicating a 2D and no 3D order. Also, the other investigated film on NGO contained no peak at $l = 1$.

The 3D CDW in YBCO films on STO is connected to a pseudo-tetragonal structure, where oxygen dopants in the chain layers do not order coherently [4]. While the 3D CDW in single crystals involves only the Cu(2) ions from the CuO_2 planes, the 3D CDW in YBCO

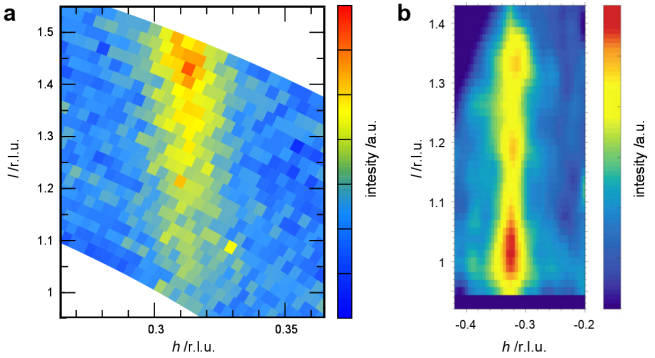

Figure 6.5: (a) The RSM around the CDW signal for DyBCO on NGO (110) at the Cu L_3 edge (931.7 eV) at 52 K reveals a 2D CDW with no enhancement at $l = 1$. (b) RSM around the CDW signal of a YBCO film on STO with 2D and 3D CDW at the Cu L_3 edge, taken from [4].

films also reveals contributions from the Cu(1) ions of the CuO chain layers. The correlation through the CuO chains suggests a competition between the formation of orthorhombic domains with long range CuO chains and the coupling of the Cu(1) ions to the Cu(2) ions.
The absence of a 3D CDW can be related to the different crystal structure of the DyBCO and YBCO films. In the DyBCO films on NGO, the orthorhombicity is less pronounced but still present as evident from the non-resonant RSM around the (4 0 10) DyBCO peak (section 5.5, Fig. 5.9d). Furthermore, the presence of orthorhombic domains is confirmed in the next section by the detection of an oxygen order in the CuO chains. The substrate also has a crucial influence on the film structure. The in-plane lattice parameters of the DyBCO films are strained to the NGO structure, while films on STO relax towards the bulk-like lattice parameters.
Therefore, DyBCO films on STO were also investigated, but no strong diffraction peak at l=1 was observed either (Fig. 6.6). This can be

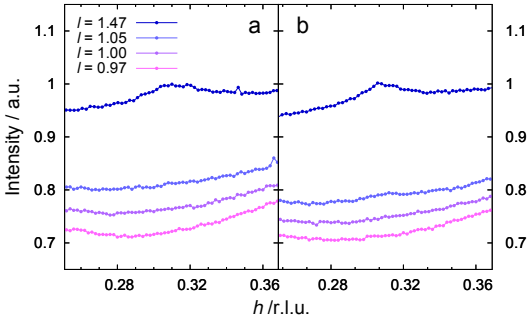

Figure 6.6: Comparison of h-scans at (0.315 0 l) at the Cu L_3 edge (931.3 eV) of DyBCO grown on STO with (a) $T_c \approx 60$ K and (b) $T_c \approx 65$ K.

related to the narrow doping range ($T_c \approx$ 50-55 K) of the 3D CDW [4]. Although DyBCO films with T_c slightly above the 3D CDW range were used to anticipate the degradation over time (T_c(before) $\rightarrow$ T_c(after): 65 K $\rightarrow$ 59 K, 60 K $\rightarrow$ 54 K), a similar doping as the YBCO films with a 3D CDW was not achieved.

Future studies should further investigate the interplay of the film structure and the formation of 3D CDW. The results from the previous chapter should be used as a guideline to systematically tune the film structure and consequently manipulate the CuO chains. Since the intensity of the 3D CDW was stronger in 50 nm YBCO films compared to 20 nm films [4], thicker films should be considered for future experiments. These do not only promise a stronger signal but also a more stable T_c.

6.1.2 Ortho-II order at the Cu L_3 edge

In addition to the charge order peak in DyBCO films on NGO, a strong signal was observed at (0.5 0 0.88), consisting of a broad and a narrow peak (Fig. 6.2b). The very sharp peak is most likely related to a substrate truncation rod and should be neglected. The l-dependence of the signal was not further explored due to limitations in the accessible reciprocal space.

The energy profile of the broad peak reveals a maximum at 933.2 eV, which relates the signal to the Cu(1) ions of the the CuO chains (Fig. 6.1). For the doping level associated with $T_c \approx 55$ K, an ortho-II oxygen order is expected in YBCO single crystals [19]. Therefore, an oxygen order in DyBCO thin films is also expected, however it had not previously been reported for any 123 thin film to our knowledge.

The broad peak at (0.5 0 l) is already observed at room temperature (Fig. 6.3b) supporting the presence of ortho-II order, which has been detected beyond 250 °C before [110]. The temperature dependence of the integrated peak intensity reveals no feature near T_c and increases slightly with decreasing temperatures. This agrees with the temperature dependence of ortho order observed in YBCO single crystals [110]. Furthermore, the application of a magnetic field up to 6 T resulted in no change of the peak intensity (Fig. 6.2b), ruling out a magnetic origin.

In conclusion, RXS at the Cu L_3 edge revealed a 2D charge order in the CuO_2 plane and an ortho-II order in the CuO chain layer, akin to YBCO single crystals.

6.2 Dy M_5 edge resonance

Next, we discuss the results of x-ray scattering experiments with photon energy tuned to the Dy M_5 edge.

X-ray absorption at the Dy M_5 edge corresponds to excitations of $3d$ electrons to the unfilled $4f$ states. The absorption spectrum fine structure exhibits three characteristic peaks. In addition to the dipole selection rule $\Delta J = 0,\pm1$, a local magnetic field splits the J multiplets into M_J sublevels, for which the selection rule $\Delta M_J = 0,\pm1$ applies. The observed three peaks in the absorption spectrum are associated to $\Delta J = 0,\pm1$ transitions. At low temperatures, the Boltzman distribution results in the uneven occupation of the different levels. In a magnetically ordered compound, one ΔM_J dominates in one ΔJ peak [114]. The transitions with $\Delta M_J = 0$ are of linear dichroic character, of orbital origin, while transitions with $\Delta M_J = \pm1$ are of circular dichroic character, of magnetic origin [114, 115]. Therefore, energy scans in resonant scattering give a hint to the origin of the observed ordered state.

Neutron diffraction on DyBCO single crystals revealed an antiferromagnetic ordering of the Dy moments below 1 K [116]. However, this temperature cannot be reached in the RXS setup at UE46 at BESSY. Using RXS, induced ordered states of the Dy ions were observed for example in $DyMnO_3$, where a Dy order was induced by the Mn spin [115], or in $DyScO_3$-$LaNiO_3$ heterostructures, where a Dy magnetic order was induced by adjacent Ni layers [117]. Therefore, we used RXS tuned to the Dy M_5 edge to investigate potentially induced Dy orders related to the charge and oxygen ordering in the copper-oxide sublattice.

6.2.1 Charge order at the Dy M_5 edge

Similar to the charge ordering at the Cu L_3 edge, a peak with the wave vector (0.315 0 l) is observed at the Dy M_5 edge (Fig. 6.7a). Increasing the temperature, the peak intensity decreased until 40 K, where the peak vanished into the background noise level (Fig. 6.3a).

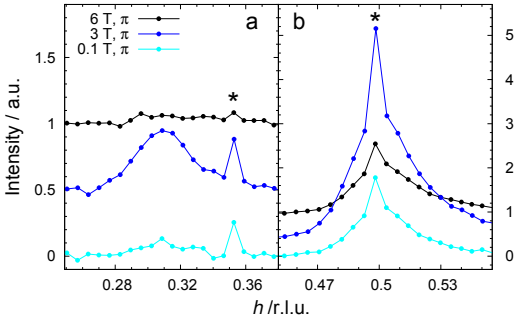

Figure 6.7: Rocking curves projected onto the reciprocal h direction at (a) (0.315 0 2.24) (CDW) and (b) (0.5 0 1.88) (ortho-II) for DyBCO at the Dy M_5 edge (1293.8 eV) at 5 K. The scans are vertically shifted for clarity. The spikes (marked with *) arise from the substrate.

In comparison to the temperature dependence of the CDW at the Cu L_3 edge, where the order is observed above 100 K and has a maximum at T_c, the Dy temperature dependence suggests an induced nature of the order at the Dy sites. At low temperatures the presence of the CDW in the proximity of the Dy ions generates a modulation of the Dy moments akin to the Cu sites, while at higher temperatures the thermal occupation of higher energy levels obscures the modulation and lets the Dy states appear effectively degenerate.

In contrast to the CDW at the Cu edge, the induced order at the Dy edge exhibits a non-monotonic field dependence (Fig. 6.8). The field was applied at $\alpha = 45$ ° from the in-plane direction (Fig. 3.6). By increasing the magnetic field to 3 T, the peak intensity increases. However, by further increasing the field above 3 T, the intensity decreases. Energy scans at the absorption edge at different magnetic field were also performed (Fig. 6.9), but due to the low scattering intensity, the interpretation of the data is difficult. At low fields only the central

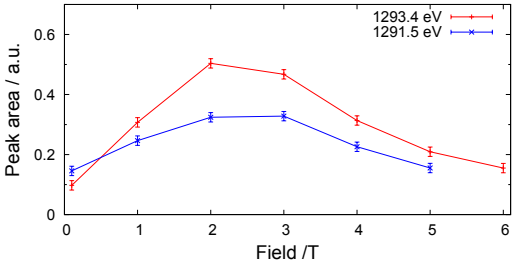

Figure 6.8: Field dependence of the CDW peak at the Dy M_5 edge at 5 K and π polarization for DyBCO on NGO. The photon energy was tuned to 1291.5 eV and 1293.4 eV corresponding to the strong peaks in the absorption spectra fine structure as shown in Fig. 6.9.

peak of the absorption spectrum has substantial scattering intensity, indicating a primary orbital origin. By increasing the magnetic field the side peaks, which have magnetic origin, also contribute to the scattering peak [115]. By increasing the magnetic field above 3 T, the side peaks decrease.

By changing the direction of the applied 3 T field from $\alpha = 45$ ° to 90 ° from the in-plane direction (Fig. 6.9), the magnetic contribution (peak A and C) in the RXS signal is strongly reduced, possibly indicating magnetic anisotropy. However, other origins can not be ruled out, since a complete angular dependence of the magnetisation was not performed. For all following discussions the orientation is kept at 45 °.

The observed order of the Dy ions reveals that the CDW in the CuO_2 planes surrounding the Dy layers also induces a modulation with the same periodicity in the Dy sublattice.

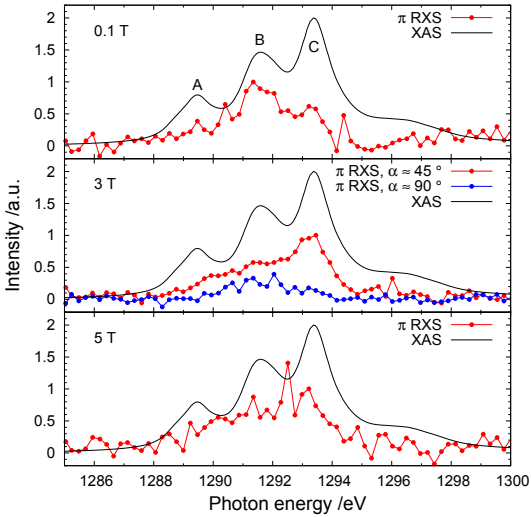

Figure 6.9: Energy profiles of the induced peak at (0.315 0 2.24) at Dy M_5 edge, 5 K and $\alpha = 45$ ° field orientation relative to the surface (Fig. 3.6). At 3 T also the field orientation of 90 ° is shown. The energy profiles are shown together with the XAS.

6.2.2 Ortho-II order at the Dy M_5 edge

Although the CuO chain layers are located rather far away from the Dy ions, the oxygen order distorts the entire crystal structure and creates orthorhombic domains, which consequently also affect the Dy arrangements. Therefore, it is not surprising that a strong peak at (0.5 0 l) is observed at the Dy M_5 edge (Fig. 6.7b). In contrast to the CDW induced order, the ortho-II induced order peak possesses a relatively high intensity already at 0.1 T applied field, suggesting a strong influence of the CuO chain arrangement on the Dy ions. Similar to the induced CDW order, the order at (0.5 0 l) decays quickly when

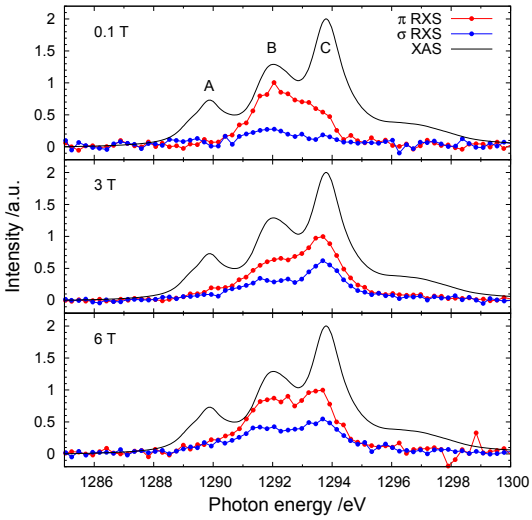

Figure 6.10: Energy profiles at Dy M_5 edge for various magnetic fields at (0.5 0 1.88) and 5 K, shown together with the XAS.

the temperature is increased (Fig. 6.3b). However, a detectable signal is still present up to room temperature.

The field dependence of the ortho-II induced peak shows the same non-monotonic behavior as in the CDW induced order, where the peak intensity increases up to 3 T and then decreases again. The field was applied at 30 ° from the in-plane direction (Fig. 3.6). The energy scans at different magnetic fields match the behavior observed in the induced CDW peak (Fig. 6.10). Due to the higher intensity of the ortho-II scattering peak, the different contributions to the photon energy dependence can be analyzed better. For example, the absence of a magnetic contribution at 0.1 T can be confirmed. While the magnetic contribution is strongest at 3 T, the corresponding side peak at 1293.4 eV is still detected at 6 T.

The similar field dependence, with a maximum in intensity at the same magnetic field for the CDW and ortho-II induced order states, opens the possibility of using the Dy ions to sense ordered states originating from other ions. By applying a moderate magnetic field, weak induced orders of the Dy ions can be enhanced.

To further understand these results, a modeling of the Dy ions was performed by Davide Betto [109]. In a simplified model, Dy ions with and without crystal field (CF) splitting were considered. The M_J states of the Dy ions without CF are degenerate, while the CF on the others stabilizes the $M_J = \pm\frac{11}{2}$ states. Upon the application of a magnetic field, the Zeeman splitting stabilizes the $M_J = +\frac{15}{2}$ state in the ions without CF, while the $M_J = +\frac{11}{2}$ state remains the ground state of the ions with CF.

In a more realistic model, a CF of different strengths acts on different Dy ions, however, this simplified model already explains the experimental data well. For low applied fields, the intensity of the induced order peak follows the paramagnetic magnetization of the Dy sublattice, which increases with an increasing magnetic field up to 3 T. This is further supported by the energy scans, which exhibit an increasing magnetic contribution until ≈ 3 T (peak A and C in Fig. 6.9 and 6.10). By increasing the field above 3 T, the magnetic moment starts to saturate. Strikingly, the intensity of the order peaks decreases above 3 T. The high field energetically lowers the states stabilized by the Zeeman splitting. This effect possibly dominates the contribution of the crystal field. Then the different Dy electronic levels become more degenerate, resulting in a lower RXS signal.

The magnetization of the Dy moments is further supported by XMCD measurements. The difference between the XAS measures with right-hand and left-hand circular polarized x-rays reveals the dichroism, as shown for the measurement at 2 T in Fig. 6.11. The integrated area of the dichroism is proportional to the magnetization. Thus, the XMCD

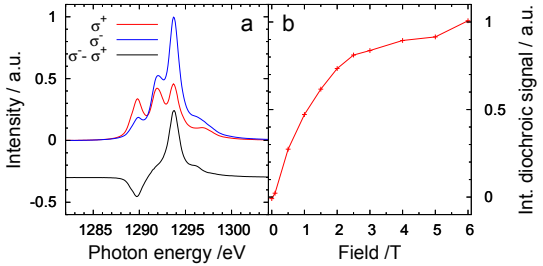

Figure 6.11: (a) XAS spectra at 2 T for σ^+ and σ^- circular polarized light, as well as the difference spectrum (XMCD). (b) Field dependence of the integrated dichroic signal.

supports that the Dy ions show a paramagnetic response up to 3 T and that the moments are saturated above 3 T.

6.3 Summary

In this chapter we focused on the results from the RXS investigation of charge and oxygen ordered states at the Cu L_3 and Dy M_5 edge. Similar to underdoped YBCO single crystals, 20 u.c. DyBCO films on NGO (110) with $T_c \approx$ 55 K showed charge ordering in the CuO_2 planes, as probed with energies resonant to the Cu L_3 edge. Remarkably, also an oxygen order in the CuO chains was detected. In contrast to YBCO films on STO, only a 2D CDW was observed in the DyBCO films. We conclude that the absence of the 3D correlation is connected to the presence of orthorhombic domains, which preclude the coupling through the CuO chains to form the 3D CDW. However, since the mechanism for the formation of the 3D CDW in thin films is not fully understood, future studies should focus in more detail on the interplay with the film structure.

Both, the charge and oxygen order, were also observed with x-ray ener-

gies resonant to the Dy M_5 edge and assigned to an induced order in the Dy layers. The magnetic field dependence revealed a non-monotonic behavior, where the intensity of the order peaks decreased above fields of 3 T. The nature of the induced order in the RE sublattices should be investigated further for other RE elements. Interesting candidates are NdBCO and GdBCO, where the RE ions have the highest and lowest orbital momentum, and the non-superconducting PrBCO, where a antiferromagnetic ordering of the Pr sublattice is observed below 19 K and which interacts with the Cu sublattice [118, 119].

Chapter 7

Conclusion

Within the scope of the present thesis three main topics have been addressed: the growth of DyBCO thin films using MBE, the investigation of their microstructure by non-resonant XRD, and the formation of ordered states studied by resonant x-ray scattering (RXS).
In the first part we described the advantages of MBE thin film growth for the 123 cuprate DyBCO. An atomic-layer-by-layer shutter sequence with *in-situ* feedback was developed to control the stoichiometry during the growth, and to suppress defect formation. The high quality of the films was confirmed by comprehensive *ex-situ* characterization, including the confirmation of single-phase *c*-axis oriented DyBCO by XRD, the observation of few surface defects by AFM, and the reduction of structural defects by STEM. Furthermore, the optimized growth was successfully extended to the growth of phase-pure *RE*BCO thin films (RE = Ho, Gd, Nd) with high T_c.
The superconducting transition of the DyBCO films was probed by mutual inductance measurements and revealed a reduced T_c in ultrathin films ($\leq$ 7 u.c.), while all films above 10 u.c. have a T_c above 80 K. Moreover, the influence of the lattice mismatch with the underlying

substrates on the resistivity was determined by transport measurements: films on LSAT exhibit the lowest resistivity, while the large tensile strain from STO and the orthorhombic crystal structure of NGO cause a higher resistivity.

The high quality of our DyBCO films allowed us to systematically investigate the orthorhombic-to-tetragonal phase transition as a function of different parameters, such as film thickness, substrate lattice mismatch, and oxygen content of the films. For substrates with low lattice mismatch (LSAT (100) and NGO (110)), the film lattice parameters adjust to the substrate lattice. While films below 20 u.c. show a pseudo-tetragonal structure, thicker films form orthorhombic domains by twinning along [110] and [1$\bar{1}$0]. Despite forming orthorhombic domains, the film lattice is still adjusted to that of the substrate. For films grown on STO (100), which provides a large tensile strain, the film lattice relaxes towards bulk-like parameters already in 20 u.c. thick films. Despite the observed relaxation, the substrate strain stabilizes a twinning along [100] and [010] for films between 20 and 40 u.c. thickness. Only in very thick films ($\geq$ 60 u.c.) a twinning along [110] and [1$\bar{1}$0] is observed.

The structure of the DyBCO films also affects their superconducting properties. DyBCO films with strong orthorhombic domains have a $T_c > 85\ K$, while films with reduced orthorhombicity and a pseudo-tetragonal structure have a broader transition and lower T_c. The reduced orthorhombicity can be obtained either by reducing the oxygen content akin to single crystals, or by reducing the film thickness and thus enhancing the strain effect from the substrate.

The stability of T_c remains challenging for both reduced films and ultra-thin films. The reduced orthorhombicity favors the transition towards the tetragonal non-superconducting phase, which is stabilized by the (pseudo-) cubic substrate lattice. The degradation of T_c could be compensated either by using a buffer layer to reduce the epitaxial

strain, by capping the films, or by increasing the film thickness, thereby increasing the time scale of the degradation as well as reducing the strain effect from the substrate.

More generally, the developed growth method for DyBCO thin films is a versatile technique, which exploits the specific advantages of MBE, such as the low deposition energy and the control of individual atomic layers. In a next step, this knowledge should be applied to the growth of multilayers. It has been shown that MBE-grown heterostructures contain sharp interfaces and a lower deviation from the intended stacking sequence compared to other growth techniques, such as PLD [50]. The possibility to substitute the *RE* ions in an atomic-layer fashion can be used to grow multilayers, for example with high-T_c and non-superconducting 123 cuprates, e.g. DyBCO-PrBCO multilayers. In such heterostructures the PrBCO layers can be used as a buffer to stabilize the orthorhombic structure of DyBCO, which promises to obtain a high T_c in heterostructures with only a few DyBCO layers [120, 121]. The stoichiometry control of MBE growth can be also applied to investigate homogeneously doped 123 cuprates, and to study the intermixing of the layers, e.g. by two-dimensional doping (delta doping) of a single high-T_c layer analogous to previous work on 214 cuprates [122]. Furthermore, the combination of insulating and superconducting layers allows the fabrication of Josephson junctions.

The heteroepitaxy is not limited to the 123 cuprate structure. For example, the combination of YBCO with the ferromagnet $La_{2/3}Ca_{1/3}MnO_3$ has revealed long range proximity effects stabilizing the CDW [123]. The investigation of this interplay in MBE-grown heterostructures promises fewer stacking faults in the 123 cuprate layer and less cation intermixing at the interface.

An important contribution of DyBCO thin films to the understanding of cuprates was described in chapter 6, where RXS was used to investigate the charge and oxygen ordered states. Similar to YBCO thin

films and single crystals, charge ordering was observed in underdoped DyBCO films. While recently YBCO films on STO revealed a 3D CDW in zero magnetic field [4], the investigated DyBCO films with similar doping level show a 2D CDW. We ascribe this difference to the choice of substrate and the significant distortion due to orthorhombic domains in the DyBCO films. The rather strong orthorhombicity was further confirmed by the presence of an ortho-II order of the CuO chain layers, which has only been observed in single crystals so far. Remarkably, both ordered states (charge and oxygen) alter the Dy ion electronic and magnetic configuration. By applying a moderate magnetic field ($\approx$ 3 T) the peak intensity of the induced order at the Dy ion is enhanced. The unique temperature- and field-dependence of these induced orders could be used to sense ordered states originating from other ions.

The observed induced orders of the Dy sublattice could be further investigated in 123 cuprates with other *RE* ions. In particular, the interplay with the orbital degree of freedom could be investigated with Nd and Gd, which have the highest and lowest orbital momentum of the rare-earth elements, respectively.

A still open question of this study is the stabilization of the 3D CDW in thin films. So far, only underdoped YBCO thin films on STO showed the 3D CDW in a fairly narrow doping range [4]. Moreover, the origin of the 3D CDW remains unclear. In YBCO single crystals the 3D CDW only evolves in high magnetic fields or under uniaxial strain [2, 3, 43]. Furthermore, it only involves the CuO_2 planes with an onset temperature similar to the 2D CDW, while the 3D CDW in thin films has a contribution from both Cu sites and is stable up to room temperature. In thin films, the involvement of the Cu ions from the CuO chain layers in the CDW formation points to the importance of the structure and a possible competition with long-range order, such as the oxygen order of the CuO chains resulting in orthorhombic do-

mains. Future experiments should continue to investigate the effects of the microstructure on the formation of the 3D CDW. The developed growth procedure and the investigation of the microstructure of DyBCO films in this thesis can be expanded to study the 3D CDW formation as a function of orthorhombicity and lattice deformation in related heterostructures. In addition, the optimized process forms the basis for the growth of more complex multilayers with atomically sharp interfaces. In such multilayers the interplay with a second material whose properties either enhance or suppress superconductivity can be studied. As such, they are novel, well-defined model systems, and their investigation could make important contributions to the understanding of high-temperature superconductivity.

List of Figures

Bibliography

1. B. Keimer *et al.*, *Nature* **518**, 179–186 (cit. on pp. 7, 13, 26). DOI 10.1038/nature14165 (Feb. 2015).
2. S. Gerber *et al.*, *Science* **350**, 949–952 (cit. on pp. 9, 15, 28, 120, 124, 140). DOI 10.1126/science.aac6257 (Nov. 2015).
3. H.-H. Kim *et al.*, *Science* **362**, 1040–1044 (cit. on pp. 9, 15, 28, 140). DOI 10.1126/science.aat4708 (Nov. 2018).
4. M. Bluschke *et al.*, *Nature Communications* **9**, 2978 (cit. on pp. 9, 15, 28, 120, 124–126, 140). DOI 10.1038/s41467-018-05434-8 (Dec. 2018).
5. H. Y. Hwang *et al.*, *Nature Materials* **11**, 103–113 (cit. on p. 17). DOI 10.1038/nmat3223 (Feb. 2012).
6. D. G. Schlom *et al.*, *Annual Review of Materials Research* **37**, 589–626 (cit. on p. 17). DOI 10.1146/annurev.matsci.37.061206.113016 (Aug. 2007).

7. P. Zubko *et al.*, *Annual Review of Condensed Matter Physics* **2**, 141–165 (cit. on p. 17).
DOI 10.1146/annurev-conmatphys-062910-140445 (Mar. 2011).

8. R. Ramesh, D. G. Schlom, *Nature Reviews Materials* **4**, 257–268 (cit. on p. 17).
DOI 10.1038/s41578-019-0095-2 (Apr. 2019).

9. J. G. Bednorz, K. A. Müller, *Zeitschrift für Physik B Condensed Matter* **64**, 189–193 (cit. on p. 19).
DOI 10.1007/BF01303701 (June 1986).

10. M. K. Wu *et al.*, *Physical Review Letters* **58**, 908–910 (cit. on p. 19).
DOI 10.1103/PhysRevLett.58.908 (Mar. 1987).

11. A. Schilling *et al.*, *Nature* **363**, 56–58 (cit. on p. 19).
DOI 10.1038/363056a0 (May 1993).

12. C. W. Chu *et al.*, *Nature* **365**, 323–325 (cit. on p. 19).
DOI 10.1038/365323a0 (Sept. 1993).

13. J. M. Tarascon *et al.*, *Physical Review B* **36**, 226–234 (cit. on pp. 20, 90, 91).
DOI 10.1103/PhysRevB.36.226 (July 1987).

14. J. G. Lin *et al.*, *Physical Review B* **51**, 12900–12903 (cit. on pp. 20, 90, 91).
DOI 10.1103/PhysRevB.51.12900 (May 1995).

15. K. Yang *et al.*, *Solid State Communications* **63**, 515–519 (cit. on pp. 20, 90, 91).
DOI 10.1016/0038-1098(87)90282-1 (Aug. 1987).

16. A. F. Holleman *et al.*, *Lehrbuch Der Anorganischen Chemie* (Walter de Gruyter, Berlin • New York, 2007) (cit. on pp. 20, 24, 123).
DOI 10.1515/9783110177701.

17. J. D. Jorgensen *et al.*, *Physical Review B* **41**, 1863–1877 (cit. on pp. 20–22, 83, 96, 101, 104).
DOI 10.1103/PhysRevB.41.1863 (Feb. 1990).

18. R. Cava *et al.*, *Physica C: Superconductivity* **165**, 419–433 (cit. on pp. 20, 21).
DOI 10.1016/0921-4534(90)90376-P (Feb. 1990).

19. M. v. Zimmermann *et al.*, *Physical Review B* **68**, 104515 (cit. on pp. 20, 22, 127).
DOI 10.1103/PhysRevB.68.104515 (Sept. 2003).

20. G. Chryssikos *et al.*, *Physica C: Superconductivity* **254**, 44–62 (cit. on p. 21).
DOI 10.1016/0921-4534(95)00553-6 (Nov. 1995).

21. K. Momma, F. Izumi, *Journal of Applied Crystallography* **44**, 1272–1276 (cit. on p. 21).
DOI 10.1107/S0021889811038970 (Dec. 2011).

22. M. Onoda *et al.*, *Japanese Journal of Applied Physics* **26**, 1049 (cit. on pp. 22, 96).
DOI 10.7567/JJAPS.26S3.1049 (Jan. 1987).

23. D. Currie, M. Weller, *Physica C: Superconductivity* **214**, 204–213 (cit. on pp. 22, 96).
DOI 10.1016/0921-4534(93)90130-I (Sept. 1993).

24. R. Liang, D. A. Bonn, W. N. Hardy, *Physical Review B* **73**, 180505 (cit. on p. 22).
DOI 10.1103/PhysRevB.73.180505 (May 2006).

25. N. Andersen *et al.*, *Physica C: Superconductivity* **317-318**, 259–269 (cit. on p. 22).
DOI 10.1016/S0921-4534(99)00066-0 (May 1999).

26. V. K. Wadhawan, *Physical Review B* **38**, 8936–8939 (cit. on p. 23).
DOI 10.1103/PhysRevB.38.8936 (Nov. 1988).

27. U. Welp *et al.*, *Physica C: Superconductivity* **161**, 1–5 (cit. on p. 23).
DOI 10.1016/0921-4534(89)90033-6 (Oct. 1989).

28. H. Schmid *et al.*, *Physica C: Superconductivity* **157**, 555–560 (cit. on p. 23).
DOI 10.1016/0921-4534(89)90285-2 (Mar. 1989).

29. J. Brötz, H. Fuess, *Physica C: Superconductivity* **339**, 75–78 (cit. on pp. 23, 101, 111).
DOI 10.1016/S0921-4534(00)00351-8 (Oct. 2000).

30. D. Schweitzer *et al.*, *Thin Solid Films* **280**, 147–151 (cit. on pp. 23, 101).
DOI 10.1016/0040-6090(95)08210-7 (July 1996).

31. A. Bianconi *et al.*, *Solid State Communications* **63**, 1009–1013 (cit. on p. 24).
DOI 10.1016/0038-1098(87)90650-8 (Sept. 1987).

32. M. Imada, A. Fujimori, Y. Tokura, *Reviews of Modern Physics* **70**, 1039–1263 (cit. on p. 25).
DOI 10.1103/RevModPhys.70.1039 (Oct. 1998).

33. J. Zaanen, G. A. Sawatzky, J. W. Allen, *Physical Review Letters* **55**, 418–421 (cit. on p. 25).
DOI 10.1103/PhysRevLett.55.418 (July 1985).

34. G. Uimin, J. Rossat-Mignod, *Physica C: Superconductivity* **199**, 251–261 (cit. on p. 25).
DOI 10.1016/0921-4534(92)90408-5 (Sept. 1992).

35. H. Ding *et al.*, *Nature* **382**, 51–54 (cit. on p. 27).
DOI 10.1038/382051a0 (July 1996).

36. A. G. Loeser *et al.*, *Science* **273**, 325–329 (cit. on p. 27).
DOI 10.1126/science.273.5273.325 (July 1996).

37. M. Hashimoto *et al.*, *Nature Physics* **10**, 483–495 (cit. on p. 27).
DOI 10.1038/nphys3009 (July 2014).

38. G. Ghiringhelli *et al.*, *Science* **337**, 821–825 (cit. on pp. 27, 120).
DOI 10.1126/science.1223532 (Aug. 2012).

39. J. Chang *et al.*, *Nature Physics* **8**, 871–876 (cit. on pp. 28, 120, 124).
DOI 10.1038/nphys2456 (Dec. 2012).

40. E. Blackburn *et al.*, *Physical Review Letters* **110** (cit. on pp. 28, 120, 124).
DOI 10.1103/PhysRevLett.110.137004 (Mar. 2013).

41. S. Blanco-Canosa *et al.*, *Physical Review Letters* **110** (cit. on pp. 28, 120).
DOI 10.1103/PhysRevLett.110.187001 (May 2013).

42. S. Blanco-Canosa *et al.*, *Physical Review B* **90** (cit. on pp. 28, 120, 123).
DOI 10.1103/PhysRevB.90.054513 (Aug. 2014).

43. J. Chang *et al.*, *Nature Communications* **7** (cit. on pp. 28, 120, 124, 140).
DOI 10.1038/ncomms11494 (Sept. 2016).

44. A. Ohtomo, H. Y. Hwang, *Nature* **427**, 423–426 (cit. on p. 32).
DOI 10.1038/nature02308 (Jan. 2004).

45. N. Reyren *et al.*, *Science* **317**, 1196–1199 (cit. on p. 32).
DOI 10.1126/science.1146006 (Aug. 2007).

46. J. L. García-Muñoz *et al.*, *Physical Review B* **46**, 4414–4425 (cit. on p. 32).
DOI 10.1103/PhysRevB.46.4414 (Aug. 1992).

47. A. Venimadhav, I. Chaitanya Lekshmi, M. Hegde, *Materials Research Bulletin* **37**, 201–208 (cit. on p. 32).
DOI 10.1016/S0025-5408(01)00777-2 (Feb. 2002).

48. M. Hepting *et al.*, *Physical Review Letters* **113**, 227206 (cit. on p. 32).
DOI 10.1103/PhysRevLett.113.227206 (Nov. 2014).

49. J.-P. Locquet *et al.*, *Nature* **394**, 453–456 (cit. on p. 32).
DOI 10.1038/28810 (July 1998).

50. F. Wrobel *et al.*, *Applied Physics Letters* **110**, 041606 (cit. on pp. 34, 139).
DOI 10.1063/1.4975005 (Jan. 2017).

51. K. Oura *et al.*, *Surface Science* (Springer Berlin Heidelberg, Berlin, Heidelberg, 2003) (cit. on pp. 34, 35).
DOI 10.1007/978-3-662-05179-5.

52. R. Hammond, R. Bormann, *Physica C: Superconductivity and its Applications* **162-164**, 703–704 (cit. on p. 36).
DOI 10.1016/0921-4534(89)91218-5 (Dec. 1989).

53. D. G. Schlom *et al.*, *Applied Physics Letters* **53**, 1660–1662 (cit. on p. 36).
DOI 10.1063/1.100443 (Oct. 1988).

54. D. Schlom *et al.*, *Journal of Crystal Growth* **102**, 361–375 (cit. on p. 36).
DOI 10.1016/0022-0248(90)90393-Y (May 1990).

55. J. Eckstein *et al.*, *MRS Bulletin* **17**, 27–33 (cit. on p. 36).
DOI 10.1557/S0883769400041828 (Aug. 1992).

56. F. Baiutti, G. Christiani, G. Logvenov, *Beilstein Journal of Nanotechnology* **5**, 596–602 (cit. on p. 37).
DOI 10.3762/bjnano.5.70 (May 2014).

57. J. N. Miller, *Journal of Vacuum Science & Technology B: Microelectronics and Nanometer Structures* **10**, 803 (cit. on p. 39).
DOI 10.1116/1.586120 (Mar. 1992).

58. F. G. Celii, *Journal of Vacuum Science & Technology B: Microelectronics and Nanometer Structures* **11**, 1018 (cit. on pp. 39, 40).
DOI 10.1116/1.586860 (June 1993).

59. C. Heyn, S. Cunis, *Journal of Vacuum Science & Technology B: Microelectronics and Nanometer Structures* **23**, 2014 (cit. on p. 39).
DOI 10.1116/1.2041648 (Sept. 2005).

60. S.-i. Gozu *et al.*, *Nanoscale Research Letters* **7**, 620 (cit. on p. 39).
DOI 10.1186/1556-276X-7-620 (Dec. 2012).

61. G. Sauerbrey, *Zeitschrift für Physik* **155**, 206–222 (cit. on p. 41).
DOI 10.1007/BF01337937 (Apr. 1959).

62. M. C. Sullivan *et al.*, *Applied Physics Letters* **106**, 031604 (cit. on p. 45).
DOI 10.1063/1.4906419 (Jan. 2015).

63. J. Als-Nielsen, D. McMorrow, *Elements of Modern X-ray Physics* (Wiley, First, Mar. 2011) (cit. on pp. 47, 52, 57).
DOI 10.1002/9781119998365.

64. H. You, *Journal of Applied Crystallography* **32**, 614–623 (cit. on p. 55).
DOI 10.1107/S0021889899001223 (Aug. 1999).

65. J. B. Nelson, D. P. Riley, *Proceedings of the Physical Society* **57**, 160–177 (cit. on p. 55).
DOI 10.1088/0959-5309/57/3/302 (May 1945).

66. H. Lüth, *Solid Surfaces, Interfaces and Thin Films* (Springer International Publishing, Cham, 2015) (cit. on p. 57).
DOI 10.1007/978-3-319-10756-1.

67. D. Putzky *et al.*, *Applied Physics Letters* **117**, 072601 (cit. on pp. 61, 95).
DOI 10.1063/5.0019673 (Aug. 2020).

68. J.-P. Locquet *et al.*, *Applied Physics Letters* **64**, 372–374 (cit. on p. 66).
DOI 10.1063/1.111151 (Jan. 1994).

69. Z.-B. Wu *et al.*, *Physical Review Materials* **4**, 124801 (cit. on pp. 70, 82).
DOI 10.1103/PhysRevMaterials.4.124801 (Dec. 2020).

70. M. Chandrasekhar *et al.*, *Materials Research Bulletin* **55**, 237–245 (cit. on p. 72).
DOI 10.1016/j.materresbull.2014.04.013 (July 2014).

71. D. Taylor, *Transactions and Journal of the British Ceramic Society* **83**, 5–9 (cit. on p. 72) (1984).

72. C. L. Teske, H. Müller-Buschbaum, *Zeitschrift für Naturforschung B* **27**, 296–301 (cit. on p. 73).
DOI 10.1515/znb-1972-0314 (Mar. 1972).

73. M. T. Weller, D. R. Lines, *Journal of the Chemical Society, Chemical Communications*, 484 (cit. on p. 73).
DOI 10.1039/c39890000484 (1989).

74. T. Lindemer, E. Specht, *Physica C: Superconductivity* **255**, 81–94 (cit. on p. 73).
DOI 10.1016/0921-4534(95)00460-2 (Dec. 1995).

75. A. Kan *et al.*, *Journal of the European Ceramic Society* **21**, 2593–2598 (cit. on p. 73).
DOI 10.1016/S0955-2219(01)00322-3 (Jan. 2001).

76. J. L. Luce, A. M. Stacy, *Chemistry of Materials* **9**, 1508–1515 (cit. on p. 73).
DOI 10.1021/cm960226u (July 1997).

77. G. Koster *et al.*, *Applied Physics Letters* **73**, 2920–2922 (cit. on p. 74).
DOI 10.1063/1.122630 (Nov. 1998).

78. D. G. Schlom *et al.*, *Zeitschrift für Physik B Condensed Matter* **86**, 163–175 (cit. on p. 76).
DOI 10.1007/BF01313822 (June 1992).

79. M. Hawley *et al.*, *Science* **251**, 1587–1589 (cit. on p. 76).
DOI 10.1126/science.251.5001.1587 (Mar. 1991).

80. S. Bals *et al.*, *Physica C: Superconductivity* **355**, 225–230 (cit. on p. 77).
DOI 10.1016/S0921-4534(01)00034-X (June 2001).

81. G. Rijnders *et al.*, *Applied Physics Letters* **84**, 1150–1152 (cit. on p. 77).
DOI 10.1063/1.1646463 (Feb. 2004).

82. H. W. Zandbergen *et al.*, *Nature* **331**, 596–599 (cit. on p. 78).
DOI 10.1038/331596a0 (Feb. 1988).

83. A. T. Fiory *et al.*, *Applied Physics Letters* **52**, 2165–2167 (cit. on p. 79).
DOI 10.1063/1.99757 (June 1988).

84. J. H. Claassen, M. E. Reeves, R. J. Soulen, *Review of Scientific Instruments* **62**, 996–1004 (cit. on pp. 79, 87).
DOI 10.1063/1.1141991 (Apr. 1991).

85. X. He *et al.*, *Review of Scientific Instruments* **87**, 113903 (cit. on p. 80).
DOI 10.1063/1.4967004 (Nov. 2016).

86. E. S. Hellman, *Journal of Vacuum Science & Technology B: Microelectronics and Nanometer Structures* **6**, 799 (cit. on p. 81).
DOI 10.1116/1.584334 (Mar. 1988).

87. M. Salluzzo *et al.*, *Physical Review B* **66**, 184518 (cit. on p. 81).
DOI 10.1103/PhysRevB.66.184518 (Nov. 2002).

88. R. Arpaia *et al.*, *Physical Review B* **96**, 064525 (cit. on pp. 81, 90).
DOI 10.1103/PhysRevB.96.064525 (Aug. 2017).

89. J. M. Dekkers *et al.*, *Applied Physics Letters* **83**, 5199–5201 (cit. on pp. 81, 111).
DOI 10.1063/1.1633010 (Dec. 2003).

90. R. D. Dawson *et al.*, *Physical Review Letters* **125**, 237001 (cit. on p. 82).
DOI 10.1103/PhysRevLett.125.237001 (Dec. 2020).

91. R. Arpaia *et al.*, *Physical Review Materials* **2**, 024804 (cit. on p. 83).
DOI 10.1103/PhysRevMaterials.2.024804 (Feb. 2018).

92. M. Salluzzo *et al.*, *Physical Review B* **72**, 134521 (cit. on pp. 83, 84, 90, 108).
DOI 10.1103/PhysRevB.72.134521 (Oct. 2005).

93. B. Dunlap *et al.*, *Journal of Magnetism and Magnetic Materials* **68**, L139–L144 (cit. on p. 85).
DOI 10.1016/0304-8853(87)90266-6 (Aug. 1987).

94. L. J. van der Pauw, *Philips Technical Review* **13**, 1–9 (cit. on p. 86) (1958).

95. A. Ramadan, R. Gould, A. Ashour, *Thin Solid Films* **239**, 272–275 (cit. on p. 86).
DOI 10.1016/0040-6090(94)90863-X (Mar. 1994).

96. N. W. Ashcroft, N. D. Mermin, *Solid State Physics* (Brooks/Cole, Belmont, 1976) (cit. on p. 88).

97. N. Barisic *et al.*, *Proceedings of the National Academy of Sciences* **110**, 12235–12240 (cit. on p. 88).
DOI 10.1073/pnas.1301989110 (July 2013).

98. S. Khanof, J. Mannhart, H. Boschker, *Applied Physics Letters* **113**, 022605 (cit. on p. 90).
DOI 10.1063/1.5037540 (July 2018).

99. C. B. Eom *et al.*, *Applied Physics Letters* **55**, 595–597 (cit. on p. 90).
DOI 10.1063/1.102436 (Aug. 1989).

100. J. Kurian, M. Naito, *Japanese Journal of Applied Physics* **43**, L1502–L1505 (cit. on p. 90).
DOI 10.1143/JJAP.43.L1502 (Oct. 2004).

101. C. K. Kim *et al.*, *Journal of Electron Spectroscopy and Related Phenomena*, S0368204818300884 (cit. on p. 92).
DOI 10.1016/j.elspec.2018.07.003 (Sept. 2018).

102. L Vasylechko *et al.*, *Journal of Alloys and Compounds* **297**, 46–52 (cit. on p. 97).
DOI 10.1016/S0925-8388(99)00603-9 (Feb. 2000).

103. R. J. Nelmes, G. M. Meyer, J. Hutton, *Ferroelectrics* **21**, 461–462 (cit. on p. 97).
DOI 10.1080/00150197808237297 (Jan. 1978).

104. J. D. Budai, R. Feenstra, L. A. Boatner, *Physical Review B* **39**, 12355–12358 (cit. on p. 101).
DOI 10.1103/PhysRevB.39.12355 (June 1989).

105. T. Steinborn *et al.*, *Physica C: Superconductivity* **220**, 219–226 (cit. on p. 101).
DOI 10.1016/0921-4534(94)90906-7 (Feb. 1994).

106. M. Déchamps, D. Favrot-Colson, A. Rosová, *Key Engineering Materials* **101-102**, 217–236 (cit. on p. 101).
DOI 10.4028/www.scientific.net/KEM.101-102.217 (Mar. 1995).

107. X. Jiang *et al.*, *Physical Review Letters* **67**, 2167–2170 (cit. on p. 104).
DOI 10.1103/PhysRevLett.67.2167 (Oct. 1991).

108. J. Brötz *et al.*, *Physical Review B* **57**, 3679–3682 (cit. on p. 111).
DOI 10.1103/PhysRevB.57.3679 (Feb. 1998).

109. D. Betto *et al.*, *Physical Review B* **102**, 195149 (cit. on pp. 119, 133).
DOI 10.1103/PhysRevB.102.195149 (Nov. 2020).

110. A. J. Achkar *et al.*, *Physical Review Letters* **109**, 167001 (cit. on pp. 120, 127).
DOI 10.1103/PhysRevLett.109.167001 (Oct. 2012).

111. H. Jang *et al.*, *Proceedings of the National Academy of Sciences* **113**, 14645–14650 (cit. on pp. 120, 124).
DOI 10.1073/pnas.1612849113 (Dec. 2016).

112. D. G. Hawthorn *et al.*, *Physical Review B* **84**, 075125 (cit. on pp. 120, 121).
DOI 10.1103/PhysRevB.84.075125 (Aug. 2011).

113. J. Fink *et al.*, *Journal of Electron Spectroscopy and Related Phenomena* **66**, 395–452 (cit. on p. 121).
DOI 10.1016/0368-2048(93)01857-B (Jan. 1994).

114. J. B. Goedkoop *et al.*, *Physical Review B* **37**, 2086–2093 (cit. on p. 128).
DOI 10.1103/PhysRevB.37.2086 (Feb. 1988).

115. E. Schierle *et al.*, *Physical Review Letters* **105**, 167207 (cit. on pp. 128, 130).
DOI 10.1103/PhysRevLett.105.167207 (Oct. 2010).

116. A. I. Goldman *et al.*, *Physical Review B* **36**, 7234–7236 (cit. on p. 128).
DOI 10.1103/PhysRevB.36.7234 (Nov. 1987).

117. M. Bluschke *et al.*, *Physical Review Letters* **118**, 207203 (cit. on p. 128).
DOI 10.1103/PhysRevLett.118.207203 (May 2017).

118. J. P. Hill *et al.*, *Physical Review B* **58**, 11211–11214 (cit. on p. 135).
DOI 10.1103/PhysRevB.58.11211 (Nov. 1998).

119. J. P. Hill *et al.*, *Physical Review B* **61**, 1251–1255 (cit. on p. 135).
DOI 10.1103/PhysRevB.61.1251 (Jan. 2000).

120. T. Terashima *et al.*, *Physical Review Letters* **67**, 1362–1365 (cit. on p. 139).
DOI 10.1103/PhysRevLett.67.1362 (Sept. 1991).

121. M. Varela *et al.*, *Physical Review B* **62**, 12509–12515 (cit. on p. 139).
DOI 10.1103/PhysRevB.62.12509 (Nov. 2000).

122. F. Baiutti *et al.*, *Nature Communications* **6**, 8586 (cit. on p. 139).
DOI 10.1038/ncomms9586 (Dec. 2015).

123. A. Frano *et al.*, *Nature Materials* **15**, 831–834 (cit. on p. 139). DOI 10.1038/nmat4682 (Aug. 2016).

Acknowledgements

During my PhD years, I had the privilege and pleasure to encounter and work with many fantastic people. In the following, I would like to use this opportunity to thank everybody who has helped me along the way.

First of all, I would like to thank Prof. Keimer for giving me the great opportunity to join his department and benefit from the excellent technical and intellectual resources. His dedication to science was truly inspiring to me. I deeply appreciate his guidance, support and trust during my PhD. Furthermore, I am grateful to him for giving me the opportunity to expand my chemical background while gaining insights into the exciting world of condensed matter physics, as well as the possibility to broaden my horizon in workshops, research schools and conferences.

I am also very thankful to Prof. Schmitz and Prof. Niewa for agreeing to be on my thesis committee and for evaluating my thesis.

I am grateful to my day-to-day supervisor Dr. Eva Benckiser for providing guidance throughout my PhD years. I benefited from her extensive knowledge on the careful analysis of x-ray data which permanently shaped my view on reciprocal space maps. I would like to thank Dr. Gennady Logvenov for his supervision regarding thin film growth and for sharing his in-depth knowledge about MBE with me.

Special thanks to Dr. Matteo Minola, who introduced me to resonant x-ray scattering and further provided much appreciated supervision, support and advice during my projects. Eva, Gennady and Matteo were always there for any kind of question.

Thin film growth would not have been possible without Georg Christiani and Peter Specht, who I am deeply grateful to. Georg is a never-ending source of knowledge on film growth and always provided a fresh perspective on the interpretation of RHEED patterns. Peter knows the MBE inside out, readily fixes arising problems, implements upgrades and will eventually become one with the setup.

Beamtimes are always exciting, but at the same time quite exhausting. I would therefore like to thank the beamline scientists and my great colleagues for their tireless commitment and help. At KARA, I could always count on the on-site support of Peter Wochner and Shyjumon Ibrahimkutty, regardless whether it was day or night. Thank you to Padma Radhakrishnan for being my reliable partner on many beamtimes, even if only for a few hours of beam. I want to particularly thank Christopher Dietl, who not only taught me how to operate x-ray diffractometers and how to write macros, but also how to fix them. At BESSY, Enrico Schierle and Martin Bluschke were indispensable in preparing the experiments and made important contributions to discussions about the data. Thank you to Davide Betto for enriching the project with his profound experience in x-ray scattering and contributing calculations.

I am thankful for my wonderful and inspiring office mates: Friederike Wrobel, who shared the secrets of film growth with me, Maximilian Krautloher, Hun-ho Kim and Xiaotong Chi. Thanks for all the great discussions we had.

I thank all members of Prof. Keimer's department, it was a pleasure working with you: Joel Bertinshaw, Alexander Boris, Robert Dawson, Hlynur Gretarsson, Laura Guasco, Matthias Hepting, Marc Höppner,

Timofei Larkin, Humei Liu, Toshinao Loew, Yi Lu, Simon Mayer, Suguru Nakata, Roberto Ortiz, Juan Porras, Rebecca Pons, Daniel Pröpper, Ksenia Rabinovic, Cissy Suen, Hakuto Suzuki, Heiko Trepka, Kentaro Ueda, Lichen Wang, Zichen Yang, Peter Yordanov, Junbang Zeng and Valentin Zimmermann. Special thanks to Katrin Fürsich and Gideok Kim for the adventures we had while attending conferences. Furthermore, I appreciate the support from Sonja Balkema, Benjamin Bruha, Kirsten Eppard, Hans-Georg Libuda, Manfred Ohl and Michael Schulz in administrative and technical matters.

I would like to express my gratitude for the help I received from colleagues outside of the department: Dr. Rotraut Merkle for being part of my PhD comitee; Benjamin Stuhlhofer for discussing and explaining the equipment; Birgit Lemke, Stephan Schmid and Yvonne Stuhlhofer for sputtering the contacts on the films; Hans Boschker for discussions on YBCO growth; Ilya Drozdov and Ze-Bin Wu at BNL for sharing their knowledge about MBE growth.

I feel blessed for the friends I have made at the institute. Alessandro, who started with me; the fellow PhD representatives of 2016: Anna, Jachym, Luzia, Pinar, Rafael and Werner; as well as Alexander, Basti, Erin, Filip, Johannes, Julia, Lukas, Marie, Parmida, Robin and many more. Thank you for making the institute more than just a workplace.

Finally, I am very grateful to my family. You have sparked my interest in science and given me unconditional support and love throughout the years. Last but not least, I would like to thank my girlfriend Maria for her constant encouragement and her never-ending support.

List of Publications

9) D. Betto, M. Bluschke, **D. Putzky**, E. Schierle, A. Amorese, K. Fürsich, S. Blanco-Canosa, G. Christiani, G. Logvenov, B. Keimer, and M. Minola:
Imprint of charge and oxygen orders on Dy ions in $DyBa_2Cu_3O_{6+x}$ thin films probed by resonant x-ray scattering,
Physical Review B **102**, 195149 (2020).

8) Z. Wu, **D. Putzky**, A. K. Kundu, H. Li, S. Yang, Z. Du, S. H. Joo, J. Lee, Y. Zhu, G. Logvenov, B. Keimer, K. Fujita, T. Valla, I. Bozovic, and I. K. Drozdov:
Homogeneous superconducting gap in $DyBa_2Cu_3O_{7-\delta}$ synthesized by oxide molecular beam epitaxy,
Physical Review Materials **4**, 124801 (2020).

7) R. D. Dawson, K. S. Rabinovich, **D. Putzky**, G. Christiani, G. Logvenov, B. Keimer, and A. V. Boris:
Approaching Two-Dimensional Superconductivity in Ultrathin $DyBa_2Cu_3O_{7-\delta}$,
Physical Review Letters **125**, 237001 (2020).

6) G. Kim, K. Son, Y. E. Suyolcu, L. Miao, N. J. Schreiber, H. P. Nair, **D. Putzky**, M. Minola, G. Christiani, P. A. van Aken, K. M. Shen, D. G. Schlom, G. Logvenov, and B. Keimer:
Inhomogeneous ferromagnetism mimics signatures of the topological Hall effect in $SrRuO_3$ films,
Physical Review Materials **4**, 104410 (2020).

5) **D. Putzky**, P. Radhakrishnan, Y. Wang, P. Wochner, G. Christiani, M. Minola, P. A. van Aken, G. Logvenov, E. Benckiser, and B. Keimer:
Strain-induced structural transition in $DyBa_2Cu_3O_{7-x}$ films grown by atomic layer-by-layer molecular beam epitaxy,
Applied Physics Letters **117**, 072601 (2020).

4) C. Hao, M.-J. Kim, K. Katsumi, S. Kovalev, R. D. Dawson, L. Schwarz, N. Yoshikawa, G. Kim, **D. Putzky**, Z. Z. Li, H. Raffy, S. Germanskiy, J.-C. Deinert, N. Awari, I. Ilyakov, B. Green, M. Chen, M. Bawatna, G. Christiani, G. Logvenov, Y. Gallais, A. V. Boris, B. Keimer, A. Schnyder, D. Manske, M. Gensch, Z. Wang, R. Shimano, and S. Kaiser:
Phase-resolved Higgs response in superconducting cuprates,
Nature Communications **11**, 1793 (2020).

3) G. Kim, Y. E. Suyolcu, J. Herrero-Martin, **D. Putzky**, H. P. Nair, J. P. Ruf, N. J. Schreiber, C. Dietl, G. Christiani, G. Logvenov, M. Minola, P. A. van Aken, K. M. Shen, D. G. Schlom, and B. Keimer:
Electronic and vibrational signatures of ruthenium vacancies in Sr_2RuO_4 thin films,
Physical Review Materials **3**, 094802 (2019).

2) M. Bluschke, A. Frano, E. Schierle, **D. Putzky**, F. Ghorbani, R. Ortiz, H. Suzuki, G. Christiani, G. Logvenov, E. Weschke, R. J. Birgeneau, E. H. da Silva Neto, M. Minola, S. Blanco-Canosa, and B. Keimer:
Stabilization of three-dimensional charge order in $YBa_2Cu_3O_{6+x}$ via epitaxial growth
Nature Communications **9**, 2978 (2018).

1) C. Dietl, S. K. Sinha, G. Christiani, Y. Khaydukov, T. Keller, **D. Putzky**, S. Ibrahimkutty, P. Wochner, G. Logvenov, P. A. van Aken, B. J. Kim, and B. Keimer:
Tailoring the electronic properties of Ca_2RuO_4 via epitaxial strain,
Applied Physical Letters **112**, 031902 (2018)

Erklärung über die Eigenständigkeit der Dissertation

Ich versichere, dass ich die vorliegende Arbeit mit dem Titel
„Thin film growth and structural investigation of $DyBa_2Cu_3O_{7-\delta}$“
selbständig verfasst und keine anderen als die angegebenen Quellen und Hilfsmittel benutzt habe; aus fremden Quellen entnommene Passagen und Gedanken sind als solche kenntlich gemacht.

Declaration of Authorship

I hereby certify that the dissertation entitled
„Thin film growth and structural investigation of $DyBa_2Cu_3O_{7-\delta}$“
is entirely my own work except where otherwise indicated. Passages and ideas from other sources have been clearly indicated.

Name/Name: Daniel Putzky

Unterschrift/Signed:

Datum/Date: